Integrated-Circuit Structures on Anisotropic Substrates

NICÓLAOS G. ALEXÓPOULOS, SENIOR MEMBER, IEEE

(Invited Paper)

Abstract—**This paper addresses the problem of anisotropy in substrate materials for microwave integrated-circuit applications. It is shown that in modeling the circuit characteristics, a serious error is incurred which becomes larger with increasing frequency when the substrate anisotropy is neglected. Quasi-static, dynamic, and empirical methods employed to obtain the propagation characteristics of microstrip, coplanar waveguides, and slotlines on anisotropic substrates are presented. Numerical solutions such as the method of moments and the transmission-line matrix technique are outlined. The modified Wiener–Hopf, the Fourier series techniques, and the method of lines are also discussed. A critique of the aforementioned methods and suggestions for future research directions are presented. The paper includes new results as well as a review of established methods.**

I. Introduction

MANY MATERIALS used as substrates for integrated microwave circuits or printed-circuit antennas exhibit dielectric anisotropy which either occurs naturally in the material or is introduced during the manufacturing process. The development of accurate methods and optimization techniques for the design of integrated microwave circuits requires a precise knowledge of the substrate material dielectric constant. It is well recognized that variations in the value of the substrate material relative dielectric constant, as well as possible variations in the value of ϵ for different material batches, introduce errors in integrated-circuit design and reduce integrated-circuit repeatability. For these reasons and because in certain applications anisotropy serves to improve circuit performance, it must be fully and accurately accounted for.

The plurality of substrate materials used for microwave integrated circuits belong to the alumina family. Permittivity variations occurring from batch to batch necessitate repeated measurements for the accurate determination of the dielectric constant [1]; in addition, these materials are slightly anisotropic [2]. Teflon-type substrates are usually ceramic-impregnated, which introduces anisotropic behavior. It is known, e.g., that the E-10 ceramic-impregnated teflon (commonly known as Epsilam 10) is anisotropic with a relative dielectric constant $\epsilon_{yy} = 10.3$ perpendicular and $\epsilon_{xx} = \epsilon_{zz} = 13.0$ parallel to the substrate plane. Similar anisotropies are exhibited by a variety of other teflon substrates such as the TFE/glass cloth and loaded TFE/glass cloth [3].

Among the crystalline substrates, single-crystal sapphire ($\epsilon_{xx} = \epsilon_{zz} = 9.4$, $\epsilon_{yy} = 11.6$) has attracted considerable attention [4], [5]. Sapphire exhibits several very desirable properties in that it is optically transparent, it is compatible with high-resistivity silicon, its electrical properties are reproducible from batch to batch, and it exhibits a 30 percent higher thermal conductivity than alumina [2]. On the other hand, it is produced in rather small area samples (about 22 mm square) and it is quite expensive. Pyrolitic boron nitride is another anisotropic material suggested for potential use as a substrate for microwave applications [6], [7]. Boron nitride exhibits anisotropy with $\epsilon_{xx} = \epsilon_{zz} = 5.12$ and $\epsilon_{yy} = 3.4$.

There are applications where magnetic anisotropy is employed (as in nonreciprocal devices). For such applications, magnetized ferrite materials are used whose magnetic properties are depicted by a second-rank tensor permeability $\bar{\bar{\mu}}$. The elements of $\bar{\bar{\mu}}$ are related to the externally applied dc magnetic field, microwave frequency, as well as the inherent physical properties of the ferrite material [8]. Recently, microstrip [9], [10] and finline [11] have been analyzed on ferrite substrate layers.

The basic interaction of electromagnetic waves with anisotropic materials is well understood. Extensive results exist in the literature for plane-wave propagation through anisotropic materials as well as for guided waves in waveguides loaded with gyrotropic slabs [15]–[26]. As far as the determination of the characteristics of integrated microwave circuits on anisotropic substrates is concerned, however, the existing publications relate mostly to microstrip structures, with a few publications on the analysis of coupled slots and slotlines.

The intent of this paper is to present existing empirical, quasi-static, and dynamic solution methods for the derivation of the propagation characteristics for a variety of structures such as microstrip, coplanar waveguides, and slotlines. Among the quasistatic approaches, the finite differences method [4], [5], the method of moments [27]–[33], and the variational principle [34]–[43] are emphasized. The transmission-line matrix method [44]–[49], the Fourier spectrum approach [51]–[56], and the method of lines [10] constitute the dynamic solution techniques presented in

Manuscript received May 21, 1985; revised June 3, 1985. This work was supported in part by the National Science Foundation, under Research Grant ESC 82-15408 and in part by the U.S. Army, under Research Contract DAAG 29-83-K-0067.

The author is with the Electrical Engineering Department, University of California, Los Angeles, CA 90024.

0018-9480/85/1000-0847$01.00 ©1985 IEEE

this paper. Empirical methods are discussed, a critique of the accuracy and applicability of each approach is given, and finally, future research directions are suggested.

II. General Background on Anisotropic Substrates

Dielectric substrate materials are either naturally (e.g., crystalline materials) or artificially anisotropic (as a result of the manner under which they are manufactured). In either case, the permittivity of these materials is a second-rank tensor or dyadic, and it is expressed as

$$\bar{\bar{\epsilon}} = [\epsilon_{ij}] = \begin{pmatrix} \epsilon_{11} & \epsilon_{12} & \epsilon_{13} \\ \epsilon_{21} & \epsilon_{22} & \epsilon_{23} \\ \epsilon_{31} & \epsilon_{32} & \epsilon_{33} \end{pmatrix}. \tag{1}$$

For lossless crystals, $\bar{\bar{\epsilon}}$ is symmetric (i.e., $\epsilon_{ij} = \epsilon_{ji}$). For this case, $\bar{\bar{\epsilon}}$ can always be transformed into a diagonalized form

$$\bar{\bar{\epsilon}} = \begin{pmatrix} \epsilon_1 & 0 & 0 \\ 0 & \epsilon_2 & 0 \\ 0 & 0 & \epsilon_3 \end{pmatrix} \tag{2}$$

where the diagonal elements $\epsilon_1, \epsilon_2, \epsilon_3$ are the eigenvalues of $\bar{\bar{\epsilon}}$ and their directions constitute the principal dielectric axes of the crystal. Furthermore, $\bar{\bar{\epsilon}}$ is positive definite, and guarantees that the inverse $\bar{\bar{\epsilon}}^{-1}$ exists. In general, the values of $\epsilon_1, \epsilon_2, \epsilon_3$ are distinct, in which case the crystal is called biaxial [57]. Most of the crystalline substrates considered in this paper are characterized by a single axis of symmetry (optic axis) or equivalently by a diagonal tensor with two equal elements. These crystals are defined as uniaxial. With reference to the geometries shown in Fig. 1, the most general dyadic form of $\bar{\bar{\epsilon}}$ considered in this paper will be

$$\bar{\bar{\epsilon}} = \begin{pmatrix} \epsilon_{xx} & \epsilon_{xy} & 0 \\ \epsilon_{yx} & \epsilon_{yy} & 0 \\ 0 & 0 & \epsilon_{zz} \end{pmatrix}. \tag{3}$$

The dyadic elements ϵ_{xy} and ϵ_{yx} may represent misalignment of the substrate coordinate system with respect to that of the integrated circuit.

As far as magnetic substrates are concerned, the permeability tensor may take the form

$$\bar{\bar{\mu}} = \begin{pmatrix} \mu_{xx} & \mu_{xy} & 0 \\ \mu_{yx} & \mu_{yy} & 0 \\ 0 & 0 & \mu_{zz} \end{pmatrix} \tag{4}$$

when an external dc magnetic field is applied in the $\hat{x}$-direction, or the form

$$\bar{\bar{\mu}} = \begin{pmatrix} \mu_{xx} & 0 & \mu_{xz} \\ 0 & \mu_{yy} & 0 \\ \mu_{zx} & 0 & \mu_{zz} \end{pmatrix} \tag{5}$$

when the external dc magnetic field is applied in the $\hat{y}$-direction. It is the latter case which will be referred to in this paper. In the analytical development which follows, a

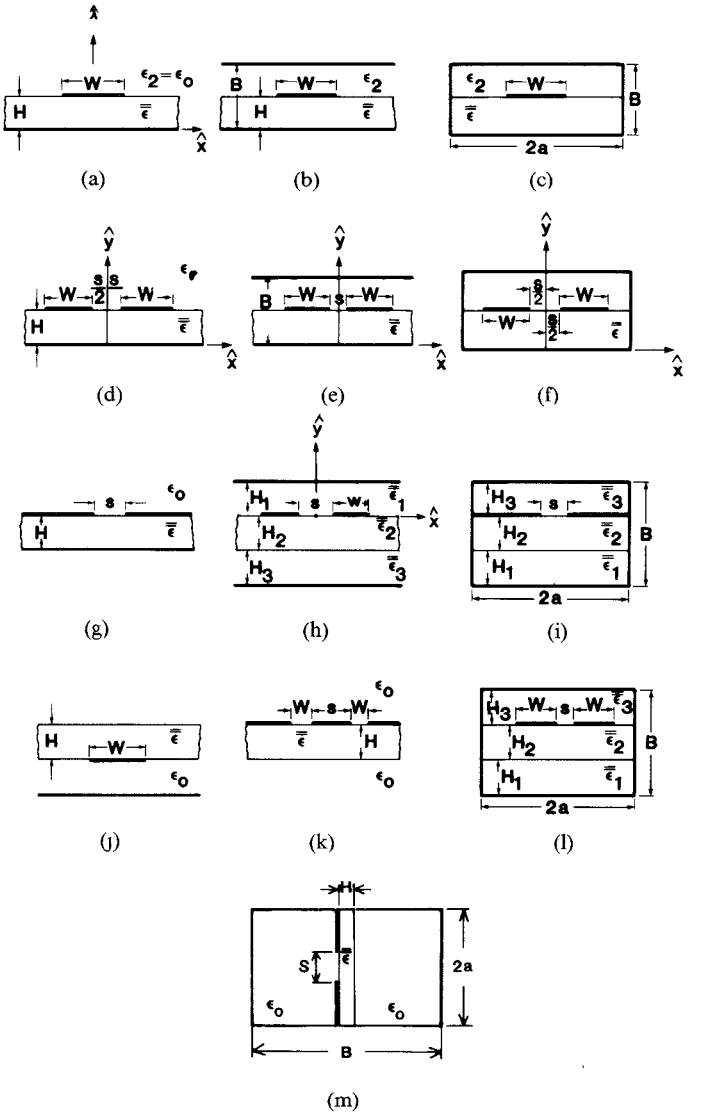

Fig. 1. A variety of integrated-circuit structures on anisotropic substrates.

tensor conductivity will also be allowed, that is,

$$\bar{\bar{\sigma}} = \begin{pmatrix} \sigma_{xx} & 0 & 0 \\ 0 & \sigma_{yy} & 0 \\ 0 & 0 & \sigma_{zz} \end{pmatrix}. \tag{6}$$

Maxwell's equations will be considered in their generalized form; thus, the system of equations to be solved is

$$\nabla \times \boldsymbol{E}(\boldsymbol{r}, t) = -\frac{\partial \boldsymbol{B}}{\partial t}(\boldsymbol{r}, t) \tag{7}$$

$$\nabla \times \boldsymbol{H}(\boldsymbol{r}, t) = \boldsymbol{J} + \frac{\partial \boldsymbol{D}}{\partial t}(\boldsymbol{r}, t) \tag{8}$$

$$\nabla \cdot \boldsymbol{B} = 0 \tag{9}$$

$$\nabla \cdot \boldsymbol{D} = \rho \tag{10}$$

with the constitutive equations

$$\boldsymbol{D}(\boldsymbol{r}, t) = \epsilon_0 \bar{\bar{\epsilon}} \cdot \boldsymbol{E}(\boldsymbol{r}, t) \tag{11}$$

$$\boldsymbol{B}(\boldsymbol{r}, t) = \mu_0 \bar{\bar{\mu}} \cdot \boldsymbol{H}(\boldsymbol{r}, t) \tag{12}$$

and

$$\boldsymbol{J}(\boldsymbol{r},t)=\bar{\bar{\sigma}}\cdot\boldsymbol{E}(\boldsymbol{r},t). \tag{13}$$

With the aid of these relations, Maxwell's equations can be written in the rectangular coordinate system as

$$\frac{\partial E_z}{\partial y}-\frac{\partial E_y}{\partial z}=-\mu_0\left(\mu_{xx}\frac{\partial H_x}{\partial t}+\mu_{xz}\frac{\partial H_z}{\partial t}\right) \tag{14}$$

$$\frac{\partial E_x}{\partial z}-\frac{\partial E_z}{\partial x}=-\mu_0\mu_{yy}\frac{\partial H_y}{\partial t} \tag{15}$$

$$\frac{\partial E_y}{\partial x}-\frac{\partial E_x}{\partial y}=-\mu_0\left(\mu_{zx}\frac{\partial H_x}{\partial t}+\mu_{zz}\frac{\partial H_z}{\partial t}\right) \tag{16}$$

and

$$\frac{\partial H_z}{\partial y}-\frac{\partial H_y}{\partial z}=\sigma_{xx}E_x+\epsilon_0\left(\epsilon_{xx}\frac{\partial E_x}{\partial t}+\epsilon_{xy}\frac{\partial E_y}{\partial t}\right) \tag{17}$$

$$\frac{\partial H_x}{\partial z}-\frac{\partial H_z}{\partial x}=\sigma_{yy}E_y+\epsilon_0\left(\epsilon_{yx}\frac{\partial E_x}{\partial t}+\epsilon_{yy}\frac{\partial E_y}{\partial t}\right) \tag{18}$$

$$\frac{\partial H_y}{\partial x}-\frac{\partial H_x}{\partial y}=\sigma_{zz}E_z+\epsilon_0\epsilon_{zz}\frac{\partial E_z}{\partial t}. \tag{19}$$

This system of equations encompasses all the cases to be treated in this paper, and solutions to this system will be provided for particular quasi-static as well as time- and frequency-domain cases. Propagation will be assumed in the z-direction. In the frequency domain, a harmonic time dependence will be considered of the form $e^{+j\omega t}$. This implies that $\partial/\partial z\rightarrow-\gamma$, where γ is the propagation constant ($\gamma=j\beta$ for lossless materials) and $\partial/\partial t\rightarrow j\omega$. For the time-harmonic solutions, the field vectors will be denoted by capital letters as, e.g., $\boldsymbol{A}(\boldsymbol{r},t)=\boldsymbol{A}(\boldsymbol{r})e^{j\omega t}$.

III. Anisotropic Materials in Integrated-Circuit Applications

The development of sophisticated analytical methods for the design of microwave integrated circuits on substrates with anisotropy is meaningful only to the extent that the physical parameters describing the anisotropy ($\bar{\bar{\epsilon}}$, $\bar{\bar{\mu}}$, or $\bar{\bar{\sigma}}$) can be accurately determined. For uniaxial crystals, $\epsilon_{\parallel}=\epsilon_{yy}$ is defined as the relative permittivity parallel and $\epsilon_{\perp}=\epsilon_{xx}=\epsilon_{zz}$ as the component perpendicular to the crystal optic axis.

Among the crystalline substrate materials, sapphire has been measured at low [58], microwave [59], [60], infrared [61], and optical frequencies [62]. At 1 KHz, the relative permittivity values were determined as $\epsilon_{\perp}=9.395\pm0.005$ and $\epsilon_{\parallel}=11.589\pm0.005$, while at 3 GHz as $\epsilon_{\perp}=9.39$ and $\epsilon_{\parallel}=11.584$ [59]. More recent results on sapphire in the microwave frequency range of 2–12 GHz indicate $\epsilon_{\perp}=9.34$ and $\epsilon_{\parallel}=11.49$ with ±0.5-percent error [60]. In this case, the measurements were performed on completely and partially metallized sapphire substrates cut with the optic axis either parallel or perpendicular to the substrate surface. The formula

$$\epsilon_{yy}=\left(\frac{c}{2lf_{n,m}}\right)^2(n^2+m^2) \tag{20}$$

is used for the computation of ϵ normal to the broad walls of the cavity, where l is the length of each side of a square substrate sample, and $f_{n,m}$ the measured resonant frequency of the n,mth node. It is estimated that, with this type of procedure, the measured resonant frequency is lower than the actual one by the fraction $\Delta f/f=1/2Q$, where Q is the loaded quality factor of the resonator [12]. This indicates that due to radiation loss at the open ends of the cavity, the method predicts a permittivity ϵ_{yy} higher than the actual value by the factor $\Delta\epsilon/\epsilon_{yy}=2(\Delta f/f)=1/Q$. The Q measurements for the $(n,0)$ mode yield $Q>200$, and therefore the correction to the measured permittivity, due to radiation losses from the cavity, is much smaller than 1 percent. When a completely metallized cavity is used, the measurements produce (due to coupling errors) higher $\bar{\bar{\epsilon}}$ than the actual value. Correct estimates of these types of error are not available, but it is suggested that $\epsilon_{\parallel}=9.40\pm0.01$ and $\epsilon_{\parallel}=11.6\pm0.01$ should be considered as the typical sapphire substrate relative permittivity values for this frequency range [2]. The ±0.01 error range is recommended by both the low-frequency measurements [58] as well as those in the infrared [61] (the latter have shown less than 0.1-percent bulk material dispersion below 300 GHz).

Single-crystal α-quartz is also a useful substrate for both microwave and millimeter-wave applications, with the permittivity tensor elements having been measured as $\epsilon_{\parallel}=4.6368\pm0.001$ and $\epsilon_{\perp}=4.5208\pm0.001$ at 1 KHz [58]. Data extrapolated to zero frequency from measurements in the far-infrared yield $\epsilon_{\parallel}=4.635\pm0.004$ [61], $\epsilon_{\parallel}=4.693\pm0.004$ [62], and $\epsilon_{\parallel}=4.635\pm0.01$ [63]. On the other hand, $\epsilon_{\perp}$ has been measured as $\epsilon_{\perp}=4.436\pm0.004$ [61], $\epsilon_{\perp}=4.46\pm0.004$ [62], and $\epsilon_{\perp}=4.418\pm0.01$ [63], indicating a discrepancy of the latter two measurements from the data obtained in [61] and [63]. Typically, quoted values for $\epsilon_{\parallel}$ and $\epsilon_{\perp}$ are 4.6 and 4.5, respectively [58].

With the exception of crystalline substrates such as sapphire and quartz, the bulk of materials used as substrates for microwave integrated-circuit applications and which exhibit varying degrees of anisotropy are the soft, high-permittivity substrates such as 3M's Epsilam 10® (E-10), Roger's RT/Duroid® 6010, and Keene Corporation's Dieclad® 810. As an example, consideration is given to Epsilam-10, which is a ceramic-impregnated teflon material (low-loss PTFE- (Polytetrafluoroethylene) based substrate). As in all cases where impregnant (fill) materials are introduced so as to obtain substrate dimensional stability, a varying degree of dielectric anisotropy is generated. The permittivity tensor elements of E-10 have the values $\epsilon_{yy}=10.2$ and $\epsilon_{xx}=\epsilon_{zz}=13.0$. The larger permittivity occurs in the xz-plane due to the shear introduced in that plane during processing. The anisotropy of impregnated PTFE materials can be measured by the plated disk test [64] to determine ϵ_{yy} and by the TE_{111} cavity test [3] (estimated accuracy of this method is 0.1–0.2 percent) for the ϵ_{xx} and ϵ_{zz} elements. A list of data from such measurements is shown in Table I for PTFE materials.

Substrate materials such as woven glass PTFE laminates consist of glass fibers oriented along planes parallel to the

TABLE I
DIELECTRIC ANISOTROPY FOR PTFE SUBSTRATES [3]

Material	Description	Sample Thickness (cm)	ϵ_{yy}	$\epsilon_{xx}, \epsilon_{zz}$
Unfilled PTFE	2 Discs	0.522	2.08	2.09
PTFE Glass	CuClad 217	0.051	2.15	2.34
PTFE Cloth	Old CuClad 2.45	0.153	2.45	2.89/2.95
PTFE Cloth	New CuClad 2.45	0.153	2.43	2.88
Filled PTFE (Glass Cloth)	GL 606	0.153	6.24	6.64/5.56

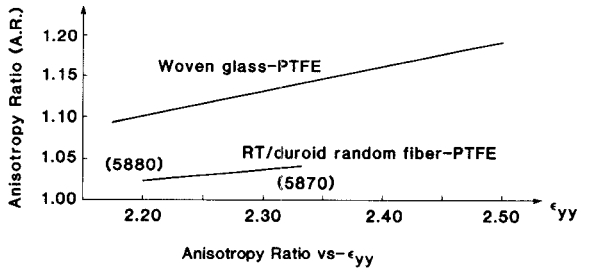

Fig. 2. Anisotropy Ratio versus ϵ_{yy}. Reprinted by permission from Rogers Co., TR 2692, July 1981.

xz-plane. These glass fiber planes are interspersed in the y-direction with the polymer matrix. From an equivalent network point of view, the substrate appears as a three-dimensional capacitance network with series connections in the $\hat{y}$-direction and parallel connections in the x, y-direction. This equivalent representation indicates that $\epsilon_{yy} < \epsilon_{xx}$, $\epsilon_{yy} < \epsilon_{zz}$. If it is desired to minimize anisotropy in composite substrate materials, the obvious solution is to (again considering the woven glass PTFE as an example) orient the glass fibers randomly. The effectiveness of this approach is shown in Fig. 2 where the measured anisotropy ratio $AR = \epsilon_{xx}/\epsilon_{yy} = \epsilon_{zz}/\epsilon_{yy}$ is graphed as a function of ϵ_{yy} for the woven glass PTFE and RT/Duroid random fiber PTFE substrates [65]. Clearly there is considerable reduction in anisotropy when a random rather than an ordered orientation of the impregnant glass fiber is enforced in the PTFE base material. Where anisotropy is not accounted for analytically, low ϵ composite substrates with randomly oriented filling to reduce anisotropy should result in more successful designs for microwave printed-circuit antennas. On the other hand, high ϵ soft substrate materials which are useful for microwave integrated circuits may exhibit considerable anisotropy even for random orientation of the filling substance. This is readily observed if a linear, albeit arbitrary, extrapolation of the random fiber-filled PTFE substrate curve is constructed. Such an extrapolation indicates, with $\epsilon_{xx} = \epsilon_{zz} \simeq 16$ and $\epsilon_{yy} = 10$, an anisotropy ratio of 1.6, which is perhaps high. The example shows, however, that for high ϵ soft substrates which are impregnated with another material matrix, anisotropy is not negligible and should be accounted for in the development of high-accuracy design procedures.

IV. Quasi-Static Methods

A full-wave analysis of integrated-circuit structures (such as microstrip) on anisotropic substrates involves the development of guided waves in terms of hybrid modes. A much simpler approach is to consider that the structure supports a dominant TEM mode, an argument especially valid at low frequencies. Under the assumption of a dominant TEM mode, a simplified design procedure evolves in a rather straightforward manner, since the guided-wave field components can be derived from the solution to Laplace's equation.

The design parameters of the microstrip structures of Fig. 1 are the characteristic impedance Z_0 and effective dielectric constant ϵ_{eff}. These parameters are defined for nonmagnetic substrates by

$$Z_0 = \frac{1}{c\sqrt{C_a C_s}} \text{ and } \epsilon_{\text{eff}} = C_s/C_a \tag{21}$$

where c is the speed of light in vacuum, C_a and C_s denote the capacitance of the strip conductor in the absence and presence of the substrate, respectively, and ϵ_{eff} is the effective dielectric constant of the structure. The computation of C_a or C_s is obtained from the definition $C_r = Q_r/V_0$ ($r = a$ or $r = s$), where V_0 is the potential of the strip with respect to ground. The total charge Q is given as

$$Q_r = \int_{-w/2}^{w/2} \rho_r(x')\, dx' \tag{22}$$

where $\rho_r(x')$ is the unknown charge density on the strip. It is clear now that the central problem of a quasi-static method is the determination of $\rho_r(x)$. If $\rho_r(x)$ is known, then the potential at any point (x, y) is given by

$$\phi_r(x, y) = \int_{-w/2}^{w/2} \rho_r(x') G_r(x - x', y - H)\, dx' \tag{23}$$

where $G_r(x - x', y - y')$ is the Green's function pertinent to the boundary-value problem. On the conductor strip ($y = H$, $|x| \leq w/2$, $|x'| \leq w/2$), $\phi(x, H) = V_0$ and therefore

$$V_{0_r} = \int_{-w/2}^{w/2} \rho_r(x') G_r(x - x')\, dx' \qquad (|x| \leq w/2,\ |x'| \leq w/2). \tag{24}$$

This is a Fredholm integral equation of the first kind to be solved for $\rho_r(x')$. The Green's function $G_r(x - x', y - y')$ is obtained by considering Laplace's equation for the given boundary-value problem. In the anisotropic medium, Laplace's equation is obtained from $\nabla \cdot \boldsymbol{D} = 0$, $\boldsymbol{D} = \bar{\bar{\epsilon}} \cdot \boldsymbol{E}$, and $\boldsymbol{E} = -\nabla\phi$, in the form

$$\nabla \cdot [\bar{\bar{\epsilon}} \cdot \nabla\phi(x, y)] = 0. \tag{25}$$

Equation (25) can be solved by the finite differences technique [4], variable substitution [66]–[71], or by Fourier transform methods [27], [72], [73]. The method is easily extendable to the characterization of coupled microstrip lines, as those shown in Fig. 1. This is readily achieved by composing the solution in terms of even- $(+V_0, V_0)$ and odd- $(+V_0, -V_0)$ mode excitation of the coupled lines (see Fig. 1(f)). Under this scheme, the even- and odd-mode impedances, and the effective dielectric constants are de-

fined as

$$Z_0^{\{e\atop o\}} = \frac{1}{c\sqrt{C_a^{\{e\atop o\}} C_s^{\{e\atop o\}}}} \quad \epsilon_{\text{eff}} = \frac{C_s^{\{e\atop o\}}}{C_a^{\{e\atop o\}}} \tag{26}$$

where

$$C_r^{\{e\atop o\}} = Q_r^{\{e\atop o\}}/V_0 \quad Q_r^{\{e\atop o\}} = \int_{s/2}^{s/2+w} \rho_r^{\{e\atop o\}}(x')\,dx'. \tag{27}$$

In addition, $\rho_r^{\{e\atop o\}}(x')$ is obtained by solving the integral equations

$$1 = \int_{s/2}^{s/2+w} \rho_r^{\{e\atop o\}}(x') G_r^{\{e\atop o\}}(x-x')\,dx' \tag{28}$$

where

$$G_r^{(c)}(x-x') = G_r(x-x') + G_r(x+x'+s) \tag{29}$$

and

$$G_r^{(0)}(x-x') = G_r(x-x') - G_r(x+x'+s). \tag{30}$$

The even- and odd-mode excitations are equivalent to erecting magnetic and electric walls, respectively, on the $x = 0$ plane. The single-strip case can be obtained from the even-mode excitation as $s/H \to 0$.

Various quasi-static design procedures have evolved for the determination of Z_0 and ϵ_{eff}. These procedures are 1) finite differences, 2) empirical, 3) method of moments, 4) coordinate transformation (variable substitution), and 5) variational methods. Each of these procedures will now be presented and their advantages as well as limitations discussed.

A. Finite Differences

The finite differences technique has been employed to obtain design parameters for microstrip without cover on a sapphire substrate [4], [5]. The $\bar{\bar{\epsilon}}$ is assumed diagonal, and therefore Laplace's equation becomes

$$\epsilon_{ixx}\frac{\partial^2\phi_i(x,y)}{\partial x^2} + \epsilon_{iyy}\frac{\partial^2\phi_i(x,y)}{\partial y^2} = 0 \tag{31}$$

where $i = 1,2$ denotes the region of validity. At the interface between the two layers, the tangential electric field and its gradient must be continuous and

$$\frac{\partial^2\phi_1(x,H)}{\partial x^2} = \frac{\partial^2\phi_2(x,H)}{\partial x^2} \tag{32}$$

is obtained. In addition, the normal $\boldsymbol{D}$ component is continuous, i.e.,

$$\epsilon_{1yy}\frac{\partial\phi_1(x,H)}{\partial y} = \epsilon_{2yy}\frac{\partial\phi_2(x,H)}{\partial y}. \tag{33}$$

If the grid shown in Fig. 3 is considered, then by the relaxation method, the potential at A, ϕ_{iA} can be obtained in terms of the potentials ϕ_{iB}, ϕ_{iC}, ϕ_{iD}, and ϕ_{iE}. Now the finite difference equation can be derived in its general form

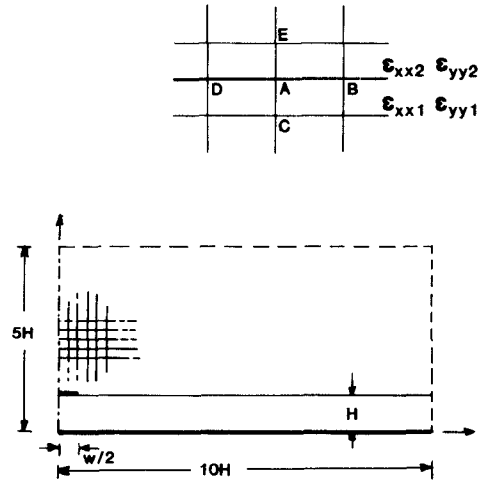

Fig. 3. Rectangular grid for application of the method of finite differences.

by eliminating derivatives in the previous equations, i.e.,

$$\frac{1}{2}(\epsilon_{2xx}+\epsilon_{1xx})(\phi_{iB}+\phi_{iD}) + \epsilon_{2yy}\phi_{iE} + \epsilon_{1yy}\phi_{iC} - (\epsilon_{2xx}+\epsilon_{1xx}+\epsilon_{2yy}+\epsilon_{1yy})\phi_{iA} = 0. \tag{34}$$

There are three regions where this generalized finite difference equation applies and where it takes distinct forms.

1) Anisotropic Region 1 ($0 < y < H$): In this region, $\epsilon_{2yy} = \epsilon_{1yy}$, $\epsilon_{2xx} = \epsilon_{1xx}$, and (34) becomes

$$\epsilon_{xx}(\phi_{1B}+\phi_{1D}) + \epsilon_{yy}(\phi_{1E}+\phi_{1C}) - 2(\epsilon_{xx}+\epsilon_{yy})\phi_{1A} = 0. \tag{35}$$

2) Interface ($y = H$): Here the top points of the grid are in air, and therefore $\epsilon_{2xx} = \epsilon_{2yy} = 1$. In addition, by writing $\epsilon_{1xx} = \epsilon_{xx}$, $\epsilon_{1yy} = \epsilon_{yy}$, $\phi_{1A} = \phi_{2A} = \phi_A$, $\phi_{1B} = \phi_{2B} = \phi_B$, $\phi_{1D} = \phi_{2D} = \phi_D$, the equation reduces to

$$\frac{1}{2}(1+\epsilon_{xx})(\phi_B+\phi_D) + \phi_{2E} + \epsilon_{yy}\phi_{1C} - (2+\epsilon_{xx}+\epsilon_{yy})\phi_A = 0. \tag{36}$$

3) $y > H$: The entire grid is in the second region, which is assumed to be a vacuum, and therefore $\epsilon_{1xx} = \epsilon_{1yy} = \epsilon_{2xx} = \epsilon_{2yy} = 1$. The difference equation is simplified now into

$$\phi_{2B} + \phi_{2C} + \phi_{2D} + \phi_{2E} - 4\phi_{2A} = 0. \tag{37}$$

The microstrip capacitance may be computed using the definition

$$C_s = \epsilon_0 \int\int_S \epsilon_n E_n\,ds \tag{38}$$

where the subscript n denotes the direction normal to the strip. Thus, under the strip $\epsilon_n = \epsilon_{yy}$, and in the air region $\epsilon_n = 1$. The choice of ϵ_n at the strip edges (substrate–air interface) is dictated by the coefficient of the term $\phi_B + \phi_D$ in (36), i.e., $\epsilon_n = (1+\epsilon_{xx})/2$. In applying the relaxation method, an overrelaxation factor of $\alpha \simeq 1.8$ has been assumed [4]. The grid is established by choosing the substrate thickness $H = 4N$, where N is the number of grid points. A zero potential boundary is assumed at $x = \pm 10H(\pm 40N)$ and at $y = 0$ and $y = 5H(20N)$. Using this scheme, the

capacitance is computed iteratively until the value changes by less than 0.1 percent. The final asymptotic value of $C_{s\infty}$ is subsequently obtained by extrapolation [2], [4].

For $w/H \geq 1$, the asymptotic capacitance value $C_{s\infty}$ is reached quickly, i.e., the finite differences method converges rapidly. When $w/H < 1$, however, the method converges very slowly and it becomes increasingly costly to determine $C_{s\infty}$. The evaluation of $C_{a\infty}$ proves more difficult, even over the range of $w/H > 1$. An accuracy of 0.5 percent is estimated [4] in computing $C_{s\infty}$ when $w/H = 0.125$ with $N = 12$. With $w/H = 9$, the method converges rapidly but the result is sensitive to box size (the estimated error for the range is stated to be of the order of 0.5 percent [4]).

This method suffers from sensitive convergence problems depending on the w/H range and box size. Even though the method is theoretically extendable to treat coupled lines, the computer cost to obtain desirable accuracy would be prohibitive. In fact, the method was not found accurate enough to obtain Z_0 and ϵ_{eff} [4] by direct computation of C_a and C_s. Consequently, an important equivalent permittivity ϵ_{req} was defined as that for isotropic substrate permittivity, which yields the same Z_0 and ϵ_{eff} [4] as the anisotropic layer. The parameter ϵ_{req} is computed by using the method of finite differences from the definition

$$\epsilon_{req} = \epsilon_b + (\epsilon_c - \epsilon_b)\left(\frac{C_{s\infty} - C_{b\infty}}{C_{c\infty} - C_{b\infty}}\right) \tag{39}$$

where ϵ_b and ϵ_c are the isotropic permittivities above and below the anticipated ϵ_{req} ($C_{b\infty}, C_{c\infty}$ are the asymptotic capacitance values for the cases corresponding to ϵ_b, ϵ_c). The behavior of ϵ_{req} with respect to the linewidth ratio w/H as obtained by the method of finite differences through the use of (39) is shown in Fig. 4(a) for a sapphire substrate [4].

B. Empirical Methods

In order to obtain a design method for microstrip on a sapphire substrate, it is possible to utilize the results obtained for ϵ_{req} with the method of finite differences and develop an empirical design approach. To this end, the empirical formula

$$\epsilon_{req} = 12.0 - \frac{1.21}{1 + 0.39\left[\log\left(\frac{10w}{H}\right)\right]^2} \tag{40}$$

has been developed [4]. The accuracy of this formula has been estimated to be ± 0.5 percent in the range $0.1 \leq w/H \leq 10.0$, and it may be used with existing methods [74], [75] for microstrip on isotropic substrates to yield design graphs for ϵ_{req} and Z_0 as shown in Fig. 4(b) [4]. The accuracy of Z_0 obtained in this manner is reported to be 4 percent for $w/H = 0.1$, and it is claimed that it improves to 0.5 percent when $w/H = 1.0$ [4]. These accuracy estimates have been found actually to be on the conservative side. A quasi-static method of moments solution indicates that (40) yields a

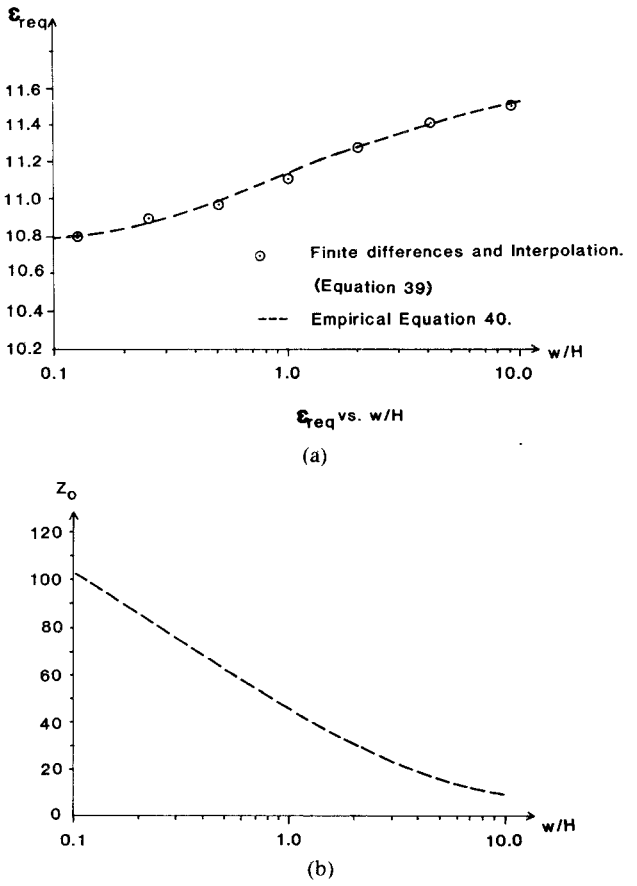

Fig. 4. (a) ϵ_{req} versus w/H. (b) Characteristic impedance Z_o versus w/H.

better than 0.4-percent accuracy for $0.1 \leq w/H \leq 10.0$, while the error in Z_0 is less than 1 percent for the same range in w/H. The empirical formula given for ϵ_{req} is simple and useful but it suffers from lack of generality, as it applies only to sapphire substrates.

C. The Method of Moments

The method of moments [76] has proven to be a very useful numerical technique in solving a variety of engineering problems in electromagnetics. It will be adopted here to obtain the total charge per unit length for a single line, and the even- and odd-mode total charges for coupled microstrip lines. The unknown charge density $\rho_n^{\{e\atop o\}}(x)$ is expanded into a series of the form

$$\rho^{\{e\atop o\}}(x) = \sum_{n=1}^{N} \alpha_n^{\{e\atop o\}} f_n(x) \tag{41}$$

where $\{f_n(x)\}$, $n = 1, 2, 3, \cdots, N$, is a set of known basis (expansion) functions, and the α_n are unknown coefficients. Substitution of this expansion into (28) yields the following pair of integral equations for the even- and odd-mode unknown coefficients $\alpha_n^{\{e\atop o\}}$:

$$1 = \sum_{n=1}^{N} \alpha_n^{\{e\atop o\}} \int_{s/2}^{s/2+w} G^{\{e\atop o\}}(x - x') f_n(x')\, dx'. \tag{42}$$

At this point, another set of known functions $\{w_m(x)\}$,

$m=1,2,3,\cdots,N$, (the testing functions) is selected and the inner product is formed with both sides of (42), i.e.,

$$\langle 1, w_m(x)\rangle = \sum_{n=1}^{N} \alpha_n^{\left\{\begin{smallmatrix} e \\ o \end{smallmatrix}\right\}} \cdot \left\langle w_m(x), \int_{s/2}^{s/2+w} G^{\left\{\begin{smallmatrix} e \\ o \end{smallmatrix}\right\}}(x-x') f_n(x')\,dx' \right\rangle \tag{43}$$

where the inner product is defined by

$$\langle f(x), w(x)\rangle = \int_{s/2}^{s/2+w} f(x)w(x)\,dx. \tag{44}$$

Equation (43) can now be written as

$$\beta_m^{\left\{\begin{smallmatrix} e \\ o \end{smallmatrix}\right\}} = \sum_{n=1}^{N} \alpha_n^{\left\{\begin{smallmatrix} e \\ o \end{smallmatrix}\right\}} g_{mn}^{\left\{\begin{smallmatrix} e \\ o \end{smallmatrix}\right\}} \tag{45}$$

where

$$\beta_m^{\left\{\begin{smallmatrix} e \\ o \end{smallmatrix}\right\}} = \langle 1, w_m(x)\rangle \tag{46}$$

and

$$g_{mn}^{\left\{\begin{smallmatrix} e \\ o \end{smallmatrix}\right\}} = \left\langle w_m(x), \int_{s/2}^{s/2+w} G^{\left\{\begin{smallmatrix} e \\ o \end{smallmatrix}\right\}}(x-x') f_n(x')\,dx' \right\rangle \tag{47}$$

or in matrix form

$$[\beta_m] = [g_{mn}][\alpha_n]. \tag{48}$$

Upon inversion, the coefficients α_n are

$$[\alpha_n] = [g_{mn}]^{-1}[\beta_m]. \tag{49}$$

The total line charge per unit length finally takes the form

$$Q^{\left\{\begin{smallmatrix} e \\ o \end{smallmatrix}\right\}} = \sum_{N=1}^{N} \alpha^{\left\{\begin{smallmatrix} e \\ o \end{smallmatrix}\right\}} \int_{s/2}^{s/2+w} f_n(x)\,dx \tag{50}$$

and therefore the even- and odd-mode capacitance is $C^{\left\{\begin{smallmatrix} e \\ o \end{smallmatrix}\right\}} = Q^{\left\{\begin{smallmatrix} e \\ o \end{smallmatrix}\right\}}$, since $V^{\left\{\begin{smallmatrix} e \\ o \end{smallmatrix}\right\}} = 1$. These capacitance values are subsequently employed to determine $Z^{\left\{\begin{smallmatrix} e \\ o \end{smallmatrix}\right\}}{}_0$, $\epsilon_{\text{eff}}^{\left\{\begin{smallmatrix} e \\ o \end{smallmatrix}\right\}}$, and $v_p^{\left\{\begin{smallmatrix} e \\ o \end{smallmatrix}\right\}}$. The single-line results can be readily obtained by allowing $s/2 \to 0$ in the formulation for the even mode. Recognize that C_r for a single strip $= 2C_r$ for coupled lines, Z_0 for a single strip $= \frac{1}{2}Z_0^e$ for coupled lines, and w/H of a single strip $= \frac{1}{2}w/H$ for coupled lines. A significant feature of the method is the choice of expansion and testing functions. These functions are critical both in the complexity of analysis as well as rate of convergence. Often the choice $\{w_n(x)\} = \{f_n(x)\}$ is made; this selection of testing and expansion functions is known as the Galerkin method [76]. For the problem at hand, $\{f_n(x)\} = \{p_n(x)\}$ is chosen where $\{p_n(x)\}$ is a set of pulse functions defined by

$$p_n(x) = P_n(x-x_n) = \begin{cases} 1, & x_n - \Delta/2 \leqslant x \leqslant x_n + \Delta/2 \\ 0, & x < x_n - \Delta/2,\ x > x_n + \Delta/2 \end{cases} \tag{51}$$

and $\Delta = (w/H)/N$. Furthermore, the testing functions $\{w_m(x)\}$ are chosen as $w_m(x) = \delta(x - x_m)$ · the point-matching method, with $x_m = \Delta(m - 1/2)$. N denotes here the number of subsections the metallic strip is divided into. Finally, the $g_{mn}^{\left\{\begin{smallmatrix} e \\ o \end{smallmatrix}\right\}}$ matrix elements reduce to

$$g_{mn}^{\left\{\begin{smallmatrix} e \\ o \end{smallmatrix}\right\}} = \int_{x_n - \Delta/2}^{x_n + \Delta/2} G^{\left\{\begin{smallmatrix} e \\ o \end{smallmatrix}\right\}}(x_m - x')\,dx'. \tag{52}$$

This approach applies to a variety of cases.

1) Microstrip on Anisotropic Substrate with Optic Axis Misalignment: It is assumed that the principal axes (ξ, η) of the anisotropic substrate form an angle θ with respect to the microstrip coordinate system (x, y) [77] (see Fig. 7). The elements of the relative permittivity tensor are given in the microstrip coordinate system by

$$\begin{aligned} \epsilon_{xx} &= \epsilon_{\xi\xi}\cos^2\theta + \epsilon_{\eta\eta}\sin^2\theta \\ \epsilon_{yy} &= \epsilon_{\xi\xi}\sin^2\theta + \epsilon_{\eta\eta}\sin^2\theta \\ \epsilon_{xy} &= \epsilon_{yx} = (\epsilon_{\xi\xi} - \epsilon_{\eta\eta})\sin\theta\cos\theta \end{aligned} \tag{53}$$

and

$$\epsilon_{zz} = \epsilon_{zz}.$$

To proceed with the method of moments, the Green's function is obtained [27] by solving the boundary-value problem for the potential functions $\phi_1(x, y)$ and $\phi_2(x, y)$. The potentials must satisfy Laplace's equation and the pertinent boundary conditions.

In Region 1:

$$\epsilon_{xx}\frac{\partial^2\phi_1}{\partial x^2} + 2\epsilon_{xy}\frac{\partial^2\phi_1}{\partial x\,\partial y} + \epsilon_{yy}\frac{\partial^2\phi_1}{\partial y^2} = 0. \tag{54}$$

In Region 2:

$$\frac{\partial^2\phi_2}{\partial x^2} + \frac{\partial^2\phi_2}{\partial y^2} = 0. \tag{55}$$

The boundary conditions are

$$\phi_1(x,0) = 0 \tag{56}$$

$$\phi_2(x, B) = 0 \tag{57}$$

$$\phi_1(x, H) = \phi_2(x, H) \tag{58}$$

and

$$\left[\epsilon_{yx}\frac{\partial\phi_1(x,y)}{\partial x} + \epsilon_{yy}\frac{\partial\phi_1(x,y)}{\partial y} - \frac{\partial\phi_2(x,y)}{\partial y}\right]_{y=H} = \frac{\rho_l}{\epsilon_0}\delta(x-x') \tag{59}$$

where ρ_l is the line of charge at $x = x'$, $y = H$, generating the potentials $\phi_1(x, y)$ and $\phi_2(x, y)$. This problem can be solved by using a Fourier transform in x and integrating the resulting ordinary differential equation in y. The transform potential in region 1 is found to be

$$\tilde{\phi}_1(\zeta, y) = \frac{\rho_l}{2\pi\epsilon_0}\frac{\exp[-j\zeta(y-H)]}{\zeta[\alpha\delta\coth(\zeta\delta H) + \coth(\zeta H\nu)]} \cdot \frac{\sinh(\zeta\delta y)}{\sinh(\zeta\delta H)} \tag{60}$$

with

$$\delta = \left[\frac{\epsilon_{xx}}{\epsilon_{yy}} - \left(\frac{\epsilon_{xy}}{\epsilon_{yy}}\right)^2\right]^{1/2} \quad \alpha = \epsilon_{yy} \text{ and } \nu = \frac{B}{H} - 1. \tag{61}$$

After deriving the inverse transforms of $\tilde{\phi}_1$ and $\tilde{\phi}_2$, the Green's function pertinent to the characterization of single and coupled microstrip is obtained from either $\phi_1(x, y)$ or $\phi_2(x, y)$ by letting $\rho_l = 1$ and $y = H$. The Green's function is

$$G(x-x') = \frac{1}{2\pi\epsilon_0}\int_{-\infty}^{\infty} d\zeta \frac{\cos[\zeta|x-x'|]}{\zeta[\alpha\delta\coth(\zeta\delta H)+\coth(\zeta H\nu)]} \tag{62}$$

from which $G\left\{\begin{matrix} e \\ o \end{matrix}\right\}(x-x')$ is obtained by considering (29) and (30). The elements of the $[g_{mn}^{\left\{\begin{matrix} e \\ o \end{matrix}\right\}}]$ matrix are derived in the form

$$g_{mn}^{\left\{\begin{matrix} e \\ o \end{matrix}\right\}} = \frac{4}{\pi\epsilon_0}\int_0^{\infty} \frac{\sin\left(\frac{\alpha\zeta}{2}\right)\left[\begin{matrix}\cos \\ \sin\end{matrix}\left(\zeta\left[x_m+\frac{s}{2}\right]\right)\right]}{\zeta^2[\alpha\delta\coth(\delta H\zeta)+\coth(\nu H\zeta)]} \cdot\left[\begin{matrix}\cos \\ \sin\end{matrix}\left(\zeta\left[x_n+\frac{s}{2}\right]\right)\right] d\zeta. \tag{63}$$

The upper limit of integration in (63) is chosen as $\zeta_m = \max(A/\delta, A/\nu)$, where A is determined from $\tanh(A) \simeq 1.0$ (for $\tanh(A) \simeq 0.999$, $A = 5$). This value of A results in the negligible error of 0.009 percent. The Green's function can also be written in the following series form by considering analytic continuation and the Cauchy residue theorem [28]:

$$G(x-x') = \frac{1}{\epsilon_0 H}\sum_{l=1}^{\infty} \frac{\exp[-v_l|x-x'|]}{v_l[\alpha\delta^2\csc^2(v_l\delta H)+\nu\csc^2(v_l H\nu)]} \tag{64}$$

where v_l is the lth root of the transcendental equation

$$\sin[v_l(\delta+\nu)H] + M\sin[v_l(\nu-\delta)H] = 0 \tag{65}$$

with

$$M = \frac{\alpha\delta-1}{\alpha\delta+1}.$$

For this representation, the matrix elements are given by

$$g_{mn}^{\left\{\begin{matrix} e \\ o \end{matrix}\right\}} = \frac{2}{\epsilon_0 H}\sum_{l=1}^{\infty} \frac{1}{v_l^2[\alpha\delta^2\csc^2(v_l\delta H)+\nu\csc^2(v_l H\nu)]} \times \begin{cases} 1-\exp\left[-v_l\frac{\Delta}{2}\right] \pm \sinh\left(\frac{v_l\Delta}{2}\right)\exp[-v_l|x_m+x_n+s|] \\ \sinh\left(\frac{v_l\Delta}{2}\right)\exp[-v_l|x_m-x_n|] \pm \exp[-v_l|x_m+x_n+s|] \end{cases} \tag{66}$$

where the upper form is valid for $x_m = x_n$, while the lower is for $x_m \neq x_n$.

Computations have been carried out for single and coupled microstrip lines with a convergence accuracy better than 0.5 percent (any desired convergence accuracy is obtainable by increasing the number of subsections N). The method of moments has been compared with other techniques for microstrip on isotropic substrates. The Bryant and Weiss approach [74] agrees well with the method of moments (to within 1 percent) except for very small linewidths where for coupled lines a discrepancy on the order of 3.5 percent is observed for the odd-mode impedance ($w/H = 0.1$, $s/H = 0.1$). It appears that when $w/H < 0.2$, the accuracy of the Bryant and Weiss results for coupled lines is somewhat questionable due to a coarse subdivision of the lines [74]. In addition, the increase in error for small linewidths may be due to the sensitivity of the finite differences method to mesh size.

The Finite Differences–Capacitance Interpolation (FD–CI) procedure (which includes the incorporation of the Bryant and Weiss algorithm) has been compared against the method of moments for a single microstrip line on a sapphire substrate. The method of moments is used in two computations whereby in one case the tensor permittivity $\bar{\bar{\epsilon}}$ is involved (MMA), while in the subsequent case ϵ_{req} is employed (MMEI). Table II summarizes the results for this comparison. For the method of moments, the geometry of Fig. 1(b) is considered with $B/H = 5.0$ and $B/H = 20.0$. The case of $B/H = 5.0$ is chosen since the empirical formula for ϵ_{req} is derived in [4] for the equivalent box size of $B/H = 5.0$. Table II indicates that when $B/H = 5.0$, the percent error is considerable when the FD–CI procedure is compared with the method of moments. On the other hand, when $B/H = 20.0$ (essentially an open structure), the agreement is very good. This may be due to the possible use in [4] of the Bryant and Weiss algorithm for an open structure. The method of moments quasi-static results shown in Table II have also been verified with excellent agreement by considering the low-frequency limit of a dynamic solution [56] for the geometry of Fig. 1(c) with the proper dimensions.

An investigation has also been carried out to determine the error introduced when the anisotropic nature of a given substrate is neglected and in addition to clarify the effect of the anisotropy ratio (AR) on line characteristics.

Table III provides a comparison of results for Z_0 and ϵ_{eff} versus w/H for an Epsilam-10 substrate with $\epsilon_{xx} = \epsilon_{zz} = 13$, and $\epsilon_{yy} = 10.3$. As Table III indicates, the error increases for narrow linewidths. This is due to the fact that the fringing field is not taken into account correctly when anisotropy is neglected, an ommission which leads to erroneous calculation of the guided wavelength, resonant length, and subsequently inaccurate equivalent-circuit representations. The method of moments yields a faster convergence in computing ϵ_{eff} than Z_0. For 0.5-percent convergence accuracy, the largest number of subsections needed for a single line was $N = 16$.

Table IV provides an understanding of the rate of convergence on the UCLA IBM 3033 computer. The results

TABLE II
COMPARISON OF FINITE DIFFERENCES (FD–CI) AND THE EMPIRICAL TECHNIQUE (MMET) WITH THE METHOD OF MOMENTS (MMA)

w/H	Z_0	Z_0	% Error	Z_0	% Error
0.125	97.095	97.76	0.68	96.982	0.80
	97.858		0.1	97.752	0.01
1.0	45.845	46.60	1.62	45.765	1.79
	46.569		0.07	46.439	0.35
9.0	9.651	10.17	5.11	9.634	5.27
	10.143		0.27	10.126	0.43
w/H	ϵ_{eff}	ϵ_{eff}	% Error	ϵ_{eff}	% Error
0.125	6.4048	6.522	1.80	6.4197	1.57
	6.4924		0.45	6.5065	0.24
1.0	7.1699	7.391	2.99	7.1949	2.65
	7.3633		0.37	7.3875	0.05
9.0	8.8135	9.718	9.31	8.8439	8.99
	9.5671		1.55	9.5977	1.24

Upper data: $B/H = 5.0$; lower data: $B/H = 20.0$.

TABLE III
ERROR IN NEGLECTING ANISOTROPY—SINGLE LINE

w/H	Z_0 $\epsilon = 10.3$ isotropic	Z_0 $\epsilon_{xx} = \epsilon_{zz} = 13$ $\epsilon_{yy} = 10.3$	%Error in Z_0	ϵ_{eff} $\epsilon = 10.3$ isotropic	ϵ_{eff} $\epsilon_{xx} = \epsilon_{zz} = 13$ $\epsilon_{yy} = 10.3$	% Error in ϵ_{eff}
0.1	105.3763	101.2740	3.89	6.1854	6.6967	8.27
1.0	48.0923	46.9167	2.44	6.8345	7.1813	5.07
2.0	32.7080	32.1597	1.68	7.2877	7.5384	3.44
3.0	25.0139	24.6982	1.26	7.6128	7.8086	2.57
4.0	20.3157	20.1101	1.01	7.8537	8.0151	2.06
5.0	17.1296	16.9846	0.85	8.0379	8.1758	1.72
7.0	13.0643	12.9792	0.65	8.2980	8.4073	1.32
9.0	10.5852	10.5243	0.58	8.4645	8.5628	1.16

All results within 0.5-percent convergence accuracy.

for a case of coupled lines ($s/H = 0.1$, $B/H = 10.0$) are also summarized in Table V. The subscripts i and a refer to Epsilam-10 with anisotropy omitted or taken into account, respectively. It is observed that the error is larger for the odd-mode characteristic impedance and ϵ_{eff} than for the even mode. The discrepancy in ϵ_{eff} is also shown in Fig. 5. Further computations demonstrate that the error increases as s/H decreases (computations for $s/H = 1.0$ yield a 6.77-percent error in ϵ_{eff}^{e}, which is lower than the corresponding cases when $s/H = 0.1$). This is due to higher intensity fringing fields between the lines for the anisotropic than for the isotropic substrate. The coupled-line algorithm required $N = 32$ for the desired convergence accuracy (5.39-s CPU) with the odd-mode converging more slowly than the even mode.

Equalization of even–odd-mode phase velocities is a goal for improving integrated-circuit performance such as the directivity D of directional couplers [77], [78]. In theory, anisotropic substrates can equalize the even- and odd-mode phase velocities for coupled microstrip without a cover, but the required AR is not realizable with known substrate materials. On the other hand, if a cover is used, the requirement $v_p^e = v_p^o$ is possible for practical isotropic as well as anisotropic substrates. Fig. 6 illustrates the behavior of ϵ_{eff} and Z_0 for coupled lines with AR > 1 (AR $= 1.26$ for Epsilam-10), AR $= 1$ (isotropic substrate with $\epsilon = 10.3$), and AR < 1 (AR $= 0.89$ for sapphire) versus B/H. Equalization of phase velocities is achieved in all three cases. Note, however, that the smaller B/H is, the more sensitive the coupler design is to tolerance errors. Substrates with AR > 1 should be utilized where phase velocity equalization and lower sensitivity to tolerance errors are desired. Table VI summarizes eight different directional coupler

TABLE IV
METHOD OF MOMENTS CPU REQUIREMENT

w/H	N	Z_0	ϵ_{eff}	IBM 3033 CPU (seconds)
0.1	8	101.6595	6.6951	0.390
1.0	12	47.1137	7.1778	0.585
5.0	16	17.0495	8.1724	0.885
7.0	16	13.0352	8.4043	0.880
9.0	16	10.5705	8.5604	0.885

$B/H = 10.0$, Fig. 1(b). For 0.5-percent convergence accuracy. $\epsilon_{xx} = \epsilon_{zz} = 13$, $\epsilon_{yy} = 10.3$.

TABLE V
COMPARISON OF COUPLED LINE CHARACTERISTICS OF EPSILAM-10 ISOTROPIC VERSUS EPSILAM-10 ANISOTROPIC

w/H	Z^e_{oi}	Z^e_{oa}	% Error	$\epsilon^e_{\text{eff}_i}$	$\epsilon^e_{\text{eff}_a}$	% Error
0.1	158.3048	152.8358	3.455	6.3705	6.8346	7.285
1.0	63.4321	62.3986	1.629	7.3236	7.5682	3.340
3.0	29.2129	29.0010	0.725	8.1945	8.3148	1.468
5.0	19.1763	19.0638	0.587	8.5260	8.6270	1.185
7.0	14.5671	14.4020	1.13	8.5867	8.7847	2.306
w/H	Z^o_{oi}	Z^o_{oa}	% Error	$\epsilon^o_{\text{eff}_i}$	$\epsilon^o_{\text{eff}_a}$	% Error
0.1	50.7637	48.1442	5.160	5.6566	6.2889	10.054
1.0	26.6548	25.4680	4.452	5.8253	6.3809	8.707
3.0	17.4429	16.9438	2.861	6.4355	6.8208	5.987
5.0	13.2197	12.9606	1.960	6.9656	7.2468	3.880
7.0	10.5131	10.4271	0.724	7.4683	7.5920	1.656

$s/H = 0.1$, $B/H = 0.5$-percent convergence accuracy.

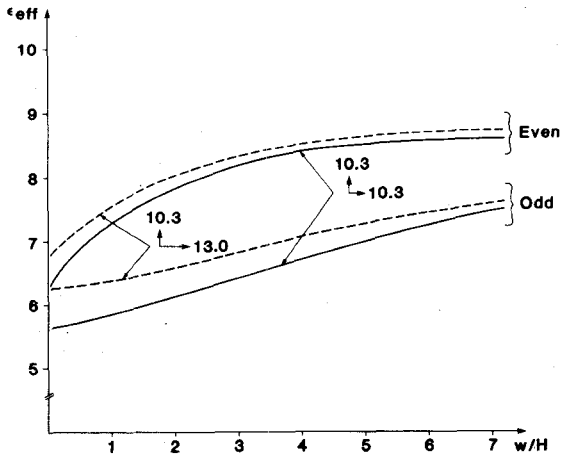

Fig. 5. Error in ϵ_{eff} versus w/H when anisotropy is ignored. Microstrip with cover: $s/H = 0.1$, $B/H = 10$.

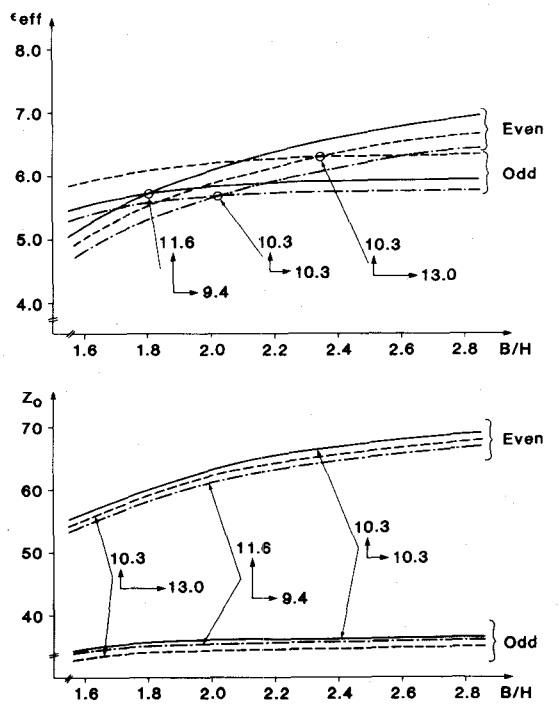

Fig. 6. Effect of AR on ϵ_{eff} and Z_o. Microstrip with cover: $w/H = 0.7$, $s/H = 0.26$.

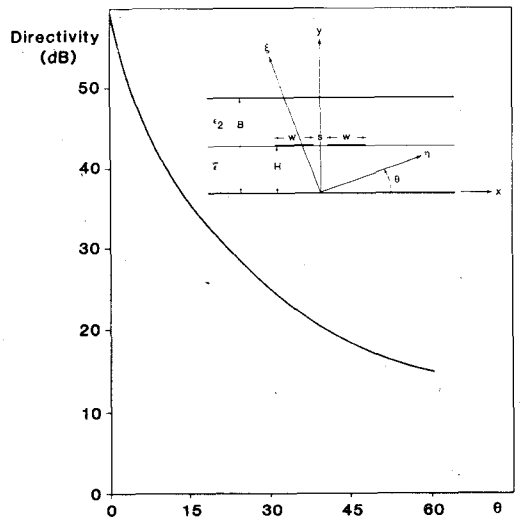

Fig. 7. 10-dB coupler boron-nitride substrate directivity versus rotation θ. $B/H = 2.8$, $s/H = 0.095$, $w/H = 1.6$.

configurations on Epsilam-10, PBN, and sapphire substrates. For each case shown, the parameters s/H and B/H were varied to obtain $Z_0^e \simeq 69.4$ and $Z_0^o = 36\ \Omega$ for a 10-dB coupler matched to a 50-Ω line. Whenever $v_p^e \simeq v_p^o$, the coupler directivity tends to infinity ($D \to \infty$); as shown in Table VI, $D \simeq 58$ dB when $B/H \simeq 2.80$ for a PBN substrate ($v_p^e = 1.876 \times 10^8$ m/s, $v_p^o = 1.875 \times 10^8$ m/s). An indication of the tight tolerances needed is clearly observed when the substrate optic axis is misaligned with respect to the microstrip coordinate system. Fig. 7 depicts the variation of D as a function of misalignment angle θ, where it is observed that even for small θ there is a significant reduction in coupler directivity [77].

2) Microstrip Couplers on an Anisotropic Substrate with an Isotropic Overlay: It has been established that coupler directivity improvement results on isotropic substrates when an isotropic overlay is used [79]–[84]. An overlay will also improve coupler directivity on anisotropic substrates by relaxing the tight tolerance requirements on B/H. This is particularly true for materials with AR < 1 (e.g., sapphire). For this design, phase velocities have been nearly equalized but, more importantly, both impedance and phase velocity curves vary quite slowly with increasing d/h (decreasing B/H) as shown in Fig. 8. Table VII indicates the usefulness of the overlay in realizing coupler designs with commercially available materials such as a 0.025-mil-thick sapphire substrate with a 0.050-mil alumina overlay. For this two-layer structure (isotropic overlay on an anisotropic substrate), the Green's function is given by [78]

$$G(x-x') = \frac{1}{2\pi\epsilon_0}\int_{-\infty}^{\infty} \frac{\cos[\zeta|x-x'|]}{\zeta}\,\frac{N(\zeta)}{D(\zeta)}\,d\zeta \quad (67)$$

where

$$N(\zeta) = \epsilon_2 + \epsilon_3 \coth(\zeta H v)\tan(\zeta t H) \quad (68)$$

TABLE VI
COUPLER DESIGNS—SUMMARY

Coupler	w/H	B/H	s/H	Z_o^e	Z_o^o	$(10^8$ m/s) v_p^e	$(10^8$ m/s) v_p^o	Directivity (dB)	VSWR	Center Freq. Coupling
Epsilam—Shielded	0.700	2.55	0.260	69.0	35.9	1.207	1.210	43	<1.01	10.02
Epsilam—Unshielded	0.800	> 6	0.280	69.4	36.0	1.138	1.204	18	1.03	10.00
Alumina Unshielded	0.875	> 6	0.260	69.2	35.9	1.150	1.286	12	1.06	10.04
Boron Nitride—Unshielded	1.850	> 6	0.120	70.0	35.9	1.772	1.860	19.5	1.03	9.83
Boron Nitride—Shielded	1.60	2.80	0.095	69.3	36.0	1.876	1.875	58	<1.01	10.00
Quartz—Unshielded	1.830	> 6	0.110	69.2	36.2	1.708	1.886	13	1.05	10.13
Sapphire—Shielded, 90° Offset ($\epsilon_{xx}=11.6$, $\epsilon_{yy}=9.4$)	0.690	2.20	0.225	69.2	35.9	1.256	1.257	49	1.01	9.98
Sapphire—Unshielded ($\epsilon_{xx}=9.4$, $\epsilon_{yy}=11.6$)	0.730	> 6	0.260	69.4	36.2	1.086	1.227	11	1.06	10.12

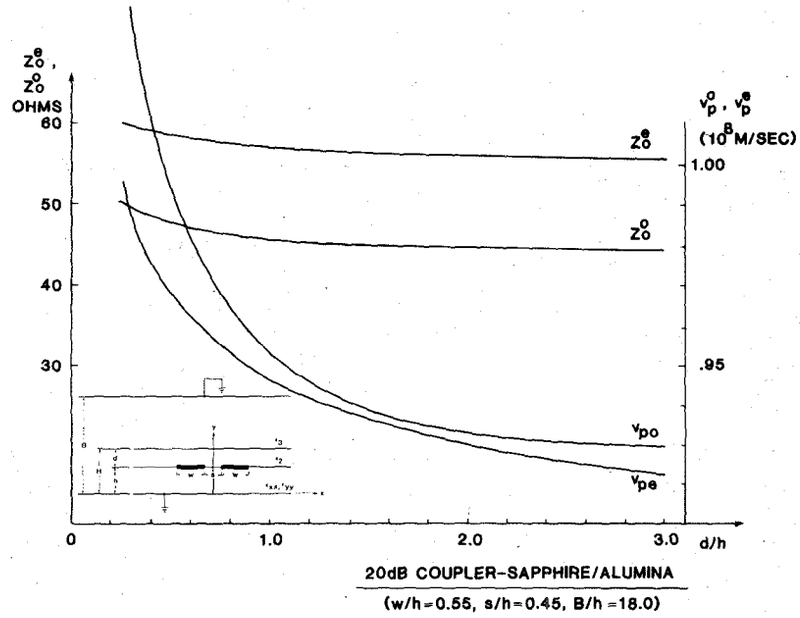

Fig. 8. 20-dB coupler-sapphire/alumina....

TABLE VII
COUPLER DESIGNS WITH AN OVERLAY

No.	Type	B/H	B/h	d/h	s/h	w/h	ϵ_2	Z_o^e	$\times 10^8$ v_p^e	Z_o^o	$\times 10^8$ v_p^e	C (dB)	Isol (dB)	Dir (dB)	VSWR
1.	10 dB (unshielded)	8.6	12.0	0.40	0.45	0.55	9.9	69.4	.9905	36.3	.9885	10.1	44.7	34.6	1.01
2.	20 dB (shielded)	3.4	6.2	0.80	1.60	0.58	9.9	55.5	.9629	45.1	.9646	19.7	57.3	37.6	1.002
3.	20 dB (shielded)	4.0	12.0	2.0	1.60	0.55	9.9	56.0	.9323	44.6	.9333	18.9	61.3	42.4	1.002
4.	20 dB (uncompensated)	12.0	12.0	0.0	1.20	0.86	—	55.5	1.068	45.3	1.180	20.0	22.4	2.4	1.02
5.	20 dB	6.0	18.0	2.0	1.60	0.55	9.9	56.1	.9306	44.6	.9333	18.9	53.0	34.1	1.00

Sapphire $\epsilon_{xx}=9.4$, $\epsilon_{yy}=11.6$. Alumina $\epsilon_2=9.9$, $\epsilon_3=1.0$.

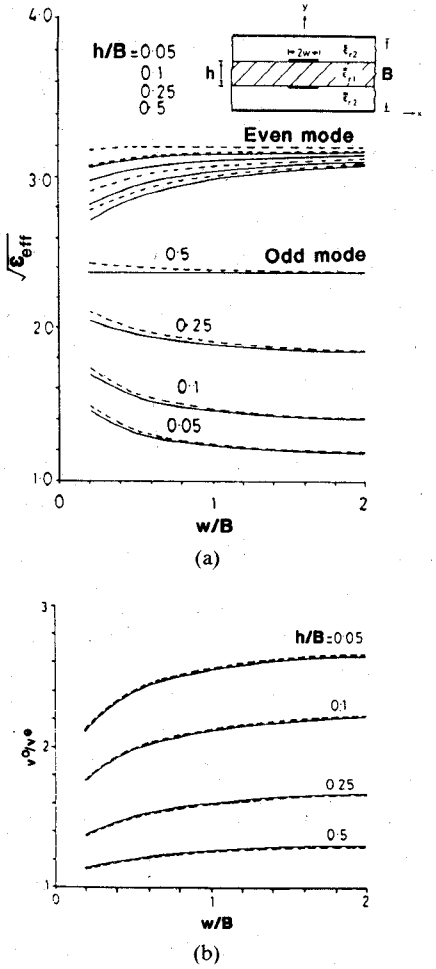

Fig. 9. (a) Even- and odd-mode factor $\sqrt{\epsilon_{\text{eff}}}$. (b) Phase-velocity ratio, v^o/v^e. Reprinted by permission from IEE *Electronics Letters* [29].

$$D(\zeta) = \tan(\zeta t H) \cdot \left[\epsilon_2^2 + \epsilon_3(\epsilon_{xx}\epsilon_{yy})^{1/2}\coth(\zeta H \nu) \cdot \coth\left(\left(\frac{\epsilon_{xx}}{\epsilon_{yy}}\right)^{1/2}\zeta h\right)\right] + \epsilon_2\left[\epsilon_3\coth(\zeta H\nu) + (\epsilon_{xx}\epsilon_{yy})^{1/2} \cdot \coth\left(\left(\frac{\epsilon_{xx}}{\epsilon_{yy}}\right)^{1/2}\zeta h\right)\right]. \quad (69)$$

The even and odd Green's function components $G^{\{e\atop o\}}(x-x')$ are obtained by using (29) and (30)

3) Broadside-Coupled Microstrip Lines: Broadside-coupled microstrip lines are considered as another application of the method of moments. The even–odd-mode Green's function for the structure shown in Fig. 9 is developed into the series form [29]

$$G^{\{e\atop o\}}(x-x') = \frac{1}{\epsilon_0}\sum_{l=1}^{\infty}\left\{\frac{2\exp(-\upsilon_l|x-x'|)}{\upsilon_l h} \cdot \left[\epsilon_{xx_1}\left\{\begin{matrix}\sec^2\left[\upsilon_l\frac{h}{2}\left(\frac{\epsilon_{xx_1}}{\epsilon_{yy_1}}\right)^{1/2}\right]\\ \cos^2\left[\upsilon_l\frac{h}{2}\left(\frac{\epsilon_{xx_1}}{\epsilon_{yy_1}}\right)^{1/2}\right]\end{matrix}\right\} + \left\{\epsilon_{xx_2}\nu\csc^2\left[\upsilon_l\frac{h}{2}\nu\left(\frac{\epsilon_{xx_2}}{\epsilon_{yy_2}}\right)^{1/2}\right]\right\}\right]\right\} \quad (70)$$

where $\nu = B/h - 1$, υ_l is the lth zero of the transcendental equation

$$\frac{\tan\left[\frac{\upsilon_l h}{2}\left(\frac{\epsilon_{xx_1}}{\epsilon_{yy_1}}\right)^{1/2}\right]^{-p}}{\cot\left[\upsilon_l\frac{h}{2}\nu\left(\frac{\epsilon_{xx_2}}{\epsilon_{yy_2}}\right)^{1/2}\right]} = (-p)\left(\frac{\epsilon_{xx_2}\epsilon_{yy_2}}{\epsilon_{xx_1}\epsilon_{yy_1}}\right)^{1/2} \quad (71)$$

and $p = \pm 1$ for even and odd modes, respectively. Incorporation of the Green's function in the algorithm yields the results [29] shown in Fig. 9(a) and (b) for broadside-coupled lines on anisotropic Epsilam-10 substrate. The curves shown indicate very small differences in $Z^{\{e\atop o\}}{}_0, \upsilon^{\{e\atop o\}}{}_p$ values between Epsilam-10 ($\epsilon_{xx} = \epsilon_{zz} = 13$, $\epsilon_{yy} = 10.2$) and AlSiMag 838 ($\epsilon = 10.2$) substrates. For small linewidths, however, the error increases when anisotropy is neglected since the fringing fields between the broadside-coupled lines is not accounted for correctly.

The method of moments proves to be a powerful tool in the effort to obtain the quasi-static characteristics of single and coupled microstrip lines on anisotropic substrates. Multiple material layers, either anisotropic or combinations of isotropic and anisotropic layers, can be incorporated into the algorithm easily by considering the appropriate Green's function for the structure. For the assumed geometries in this section (no sidewalls), the Green's function can be obtained either in integral or series form. For each structure, the series form as obtained by the Cauchy residue theorem, although it requires approximately 1/3 the computer time, is not as accurate as the integral form. This is due to the error accumulation incurred during the location of the roots when (65) or (71) are solved numerically. The results obtained for the char-

acteristic impedance by incorporating the series form in the method of moments algorithm are consistently 1–2-percent low. The integral form should be used where very high accuracy is required.

C. Coordinate Transformation Method

A simple approach to analyze the properties of microstrip on anisotropic substrates (without cover) may be developed if the Green's function given by (62) is examined closely. The anisotropy and structural dimensions are involved explicitly in the denominator term given by

$$\zeta\left[\left(\epsilon_{xx}\epsilon_{yy}-\epsilon_{xy}^2\right)^{1/2}\cdot\coth\left\{\zeta\left(\frac{\epsilon_{xx}}{\epsilon_{yy}}-\left(\frac{\epsilon_{xy}}{\epsilon_{yy}}\right)^2\right)^{1/2}H\right\}+\epsilon_2\coth(\zeta H\nu)\right].$$

If there is no top cover, $H\nu\to\infty$ as $B\to\infty$, and therefore $\coth(\zeta H\nu)\to 1$. The denominator may then be rewritten as $\zeta[\epsilon_{eq}\coth(\zeta H_{eq})+\epsilon_2]$ where [68]–[71]

$$\epsilon_{eq}=\left(\epsilon_{xx}\epsilon_{yy}-\epsilon_{xy}^2\right)^{1/2} \tag{72}$$

and

$$H_{eq}=\left[\frac{\epsilon_{xx}}{\epsilon_{yy}}-\left(\frac{\epsilon_{xy}}{\epsilon_{yy}}\right)^2\right]^{1/2}H. \tag{73}$$

This procedure reveals that the anisotropic substrate may be replaced with an "equivalent isotropic" layer whose permittivity and thickness are defined by (72) and (73). This equivalent microstrip problem can then be solved with an appropriate algorithm for isotropic substrates [74], [75]. A more rigorous justification of the "equivalent isotropic" problem has been derived by considering the simple case of a diagonalized tensor $\bar{\bar{\epsilon}}$ ($\epsilon_{xy}=\epsilon_{yx}=0$) [67], [68]. The coordinate transformation

$$\tau=x\qquad \upsilon=y\left(\frac{\epsilon_{xx}}{\epsilon_{yy}}\right)^{1/2}$$

yields Laplace's or Poisson's equation in the τ,υ coordinate system for a substrate characterized by

$$\epsilon_{eq}=\left(\epsilon_{xx}\epsilon_{yy}\right)^{1/2}\text{ and }H_{eq}=\left(\frac{\epsilon_{xx}}{\epsilon_{yy}}\right)^{1/2}H.$$

Furthermore, the relationship between $\phi(x,y)$ and $\Phi(\tau,\upsilon)$ is readily established as $\phi_P(x,y)=\Phi_Q(\tau,\upsilon)$ and $\partial\phi_P(x,y)/\partial y=(\partial\phi_Q(\tau,\upsilon)/\partial\upsilon)\frac{\partial\upsilon}{\partial y}$ where $Q(\zeta,\upsilon)$ is the point $P(x,y)$ transformed into the (τ,υ) coordinate system. Under this transformation, the boundary conditions at $y=H$ are invariant [68], i.e.,

$$E_x=-\frac{\partial\Phi}{\partial\tau}=E_\tau\text{ and }D_y=-\epsilon_0\epsilon_{eq}\frac{\partial\Phi}{\partial\upsilon}=D_\upsilon. \tag{74}$$

This method has been used in conjunction with the Bryant and Weiss algorithm [74] but the results obtained [68] are in error ranging up to 20 percent, due possibly to erroneous adaptation of the algorithm.

This approach should be used with caution when microstrip with a cover is considered, since the term $\coth(\zeta H\nu)$ cannot be equated to unity. For this case, the denominator of the Green's function takes the form $\zeta[\epsilon_{eq}\coth(\zeta H_{eq})+\epsilon_2\coth(\zeta H\nu)]$, and, strictly speaking, the concept of an equivalent isotropic substrate is no longer valid. Nevertheless, an algorithm for isotropic substrates can still be used with the extra care of proper entry for ϵ_{eq}, H_{eq}, and H.

D. The Image-Coefficient Method

An alternate approach, which also leads to the conclusions of the previous section, is to obtain the Green's function by considering the method of images for anisotropic media [30]. As a first step, Poisson's equation is considered with a unit strength per unit length charged line source at x',y'. For the moment, the entire space is anisotropic and is characterized by a diagonalized tensor $\bar{\bar{\epsilon}}$. Poisson's equation takes the form [67]

$$\epsilon_{xx}\frac{\partial^2 G}{\partial x^2}+\epsilon_{yy}\frac{\partial^2 G}{\partial y^2}=-\frac{\delta(x-x',y-y')}{\epsilon_0}. \tag{75}$$

Transforming coordinates with $\tau=x/\sqrt{\epsilon_{xx}}$, $\upsilon=y/\sqrt{\epsilon_{yy}}$, and using the delta function property $\delta(ax)=\delta(x)/|a|$, the equation is written as

$$\frac{\partial^2 G}{\partial\tau^2}+\frac{\partial^2 G}{\partial\upsilon^2}=-\frac{1}{\epsilon_0\epsilon_{xx}\epsilon_{yy}}\delta(\tau-\tau',\upsilon-\upsilon'). \tag{76}$$

This transformed Poisson equation easily yields the solution

$$G(x-x',y-y')=\frac{1}{2\pi\epsilon_0\epsilon_{eq}}\cdot\ln\left[\frac{1}{\sqrt{(x-x')^2+(y-y')^2\left(\frac{\epsilon_{yy}}{\epsilon_{xx}}\right)}}\right] \tag{77}$$

where, as before, $\epsilon_{eq}=\sqrt{\epsilon_{xx}\epsilon_{yy}}$. If the line source is now placed at x',y' above an anisotropic half-space (see Fig. 10), then consideration of the boundary conditions at the interface ($y=0$) and the reciprocity theorem [30] yield for this configuration the solution

$$G(x-x',y-y')=\begin{cases}\dfrac{\rho_1}{2\pi\epsilon_0\epsilon_{eq}}\ln\left[\dfrac{1}{\sqrt{(x-x')^2+(y-y_0')^2\left(\frac{\epsilon_{yy}}{\epsilon_{xx}}\right)}}\right], & y\leqslant 0 \quad (78)\\[2ex] \dfrac{1}{2\pi\epsilon_0}\ln\left[\dfrac{1}{\sqrt{(x-x')^2+(y-y')^2}}\right]+\dfrac{\rho_2}{2\pi\epsilon_0}\cdot\ln\left[\dfrac{1}{\sqrt{(x-x')^2+(y-y')^2}}\right], & y\geqslant 0 \quad (79)\end{cases}$$

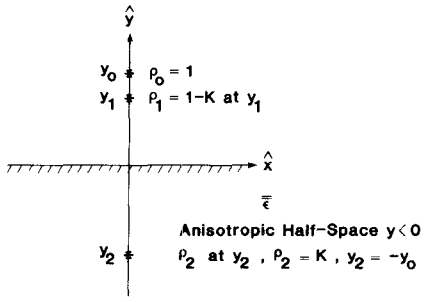

Fig. 10. Imaging a line charge source ($\rho_0 = 1$) over an anisotropic half-space.

where

$$y_0' = \sqrt{\frac{\epsilon_{xx}}{\epsilon_{yy}}}\, y' \tag{80}$$

$$y_1' = -y' \tag{81}$$

$$\rho_1 = 1 - K \tag{82}$$

$$\rho_2 = K \tag{83}$$

and

$$K = \frac{1-\epsilon_{eq}}{1+\epsilon_{eq}}. \tag{84}$$

For the microstrip geometry (without cover), multiple images result, just as for an isotropic substrate. Using image theory for this structure, the Green's function is written in the form

$$G(x-x') = \frac{1}{2\pi\epsilon_0(1+\epsilon_{eq})} \sum_{n=1}^{\infty} K^{n-1} \cdot \ln\left\{ \frac{\left[4n^2 + \left(\frac{x-x'}{H_{eq}}\right)^2\right]\left[\left(4n^2 + \frac{x+x'}{H_{eq}}\right)^2\right]}{\left[4(n-1)^2 + \left(\frac{x-x'}{H_{eq}}\right)^2\right]\left[4(n-1)^2 + \left(\frac{x+x'}{H_{eq}}\right)^2\right]} \right\} \tag{85}$$

where

$$H_{eq} = H\sqrt{\frac{\epsilon_{xx}}{\epsilon_{yy}}}.$$

This expression is identical to the Green's function by the method of images for microstrip on an isotropic substrate [86] provided the isotropic layer is characterized by the relative dielectric constant ϵ_{eq} and substrate thickness H_{eq}. This series representation of the Green's function converges rapidly and it yields results for the microstrip capacitance per unit length with excellent accuracy when adopted with an appropriate numerical method [30].

The theory of images is easily extended to obtain the Green's function for an electrooptic modulator structure, i.e., a metallic strip conductor on an anisotropic substrate of thickness H without a ground plane. This Green's function is given by [30]

$$G(x-x') = \frac{1}{2\pi\epsilon_0(1+\epsilon_{eq})} \cdot \sum_{n=1}^{\infty} K^{n-1} \ln\left\{ \frac{4(n-1)^2 + \left(\frac{x+x'}{H_{eq}}\right)^2}{4(n-1)^2 + \left(\frac{x-x'}{H_{eq}}\right)^2} \right\}. \tag{86}$$

These series representations, for both the microstrip line and electrooptic modulator structures, converge quite rapidly and they have been adopted in the discretized integral equation [30]

$$V = \sum_{j=1}^{M} \int_{y_j}^{y_{j+1}} \rho(x') G(x-x')\, dx' \tag{87}$$

where

$$\rho(x') = \rho_j + (\rho_{j+1} - \rho_j)\left(\frac{x'-x_j}{x_{j+1}-x_j}\right), \qquad 0 \leqslant x' \leqslant w/2 \tag{88}$$

with

$$x_j = \frac{w}{2}\left\{1 - \left(1 - \frac{j-1}{m}\right)^{\gamma}\right\}, \qquad j = 1,2,3,\cdots,m+1 \quad (\gamma = 1, 2, \text{or } 3). \tag{89}$$

The expression given for $\rho(x')$ gives an excellent piecewise approximation of the true charge density distribution for $0 \leqslant x' \leqslant w/2$. The total charge on the half-strip is

$$Q = \sum_{j=1}^{m} \int_{y_j}^{y_{j+1}} \rho(x')\, dx'. \tag{90}$$

When the conductor is charged to 1 V, the lineal capacitance is $C = 2Q$.

The accuracy of this approach is remarkable. The error (again comparing to the value obtained with conformal mapping) for microstrip on isotropic substrates is quoted as less than 0.0024 percent when $w/H = 0.01$ and less than 0.001 percent for $w/H > 0.01$ [30]. Similar accuracy is observed for the electrooptic modulator case [30].

E. Application of the Variational Principle

The variational principle is a powerful tool in that it yields results with very good accuracy for a variety of integrated-circuit structures. Furthermore, it provides upper- and lower-bound numerical results for the capacitance of single and coupled printed strip conductors with arbitrary substrate parameters and conductor geometry. In this section, the variational expression for capacitance is presented in the Fourier transform or space domain for a variety of microstrip geometries, as well as for unshielded suspended stripline, coupled slotlines, and coplanar waveguide structures on anisotropic substrates.

1) Fourier Transform Representation: The variational expression for the lower-bound computation of capacitance

can be derived in the form [87], [88]

$$\frac{1}{C}=\frac{1}{2\pi Q^2}\int_{-\infty}^{\infty}\tilde{\rho}(\zeta)\tilde{G}(\zeta,H)\,d\zeta \tag{91}$$

where $\tilde{\rho}(\zeta)$ and $\tilde{G}(\zeta)$ are the Fourier transforms of the line charge density and Green's function, respectively, while Q is the total charge per unit length. This variational expression can be rewritten as

$$\frac{1}{C}=\frac{1}{\pi Q^2}\int_{0}^{\infty}[\tilde{\rho}(\zeta)]^2\tilde{g}(\zeta,H)\,d\zeta \tag{92}$$

where $\tilde{g}(\zeta,H)$ is given by the following expressions depending on the structure under consideration.

Microstrip with cover:

$$\tilde{g}(\zeta,H)=\frac{1}{\epsilon_0\zeta\left[\epsilon_{eq}\coth(\zeta H_{eq})+\epsilon_2\coth(\zeta H\nu)\right]} \tag{93}$$

(usually $\epsilon_2=1$).

Microstrip without cover:

$$\tilde{g}(\zeta,H)=\frac{1}{\epsilon_0\zeta\left[\epsilon_{eq}\coth(\zeta H_{eq})+\epsilon_2\right]}. \tag{94}$$

Unshielded suspended stripline or coplanar striplines:

$$\tilde{g}(\zeta,H)=\frac{\epsilon_{eq}\coth(\zeta H_{eq})+1}{\epsilon_0\zeta\left[(1+\epsilon_{eq})+2\epsilon_{eq}\coth(\zeta H_{eq})\right]}. \tag{95}$$

The trial functions which are typically used to minimize the error in the computation of C are

$$\rho(x)=\begin{cases}|x|, & |x|\leqslant w/2\\ 0, & |x|>w/2\end{cases} \tag{96}$$

or

$$\rho(x)=\begin{cases}1+|2x/w|^3, & |x|\leqslant w/2\\ 0, & |x|>w/2\end{cases}. \tag{97}$$

The corresponding Fourier transforms are

$$\frac{\tilde{\rho}(\zeta)}{Q}=\frac{2\sin\left(\frac{\zeta w}{2}\right)}{\left(\frac{\zeta w}{2}\right)}-\left[\frac{\sin\left(\frac{\zeta w}{4}\right)}{\left(\frac{\zeta w}{4}\right)}\right]^2 \tag{98}$$

and

$$\frac{\tilde{\rho}(\zeta)}{Q}=\frac{8}{5}\left\{\frac{\sin(\zeta w/2)}{(\zeta w/2)}\right\}+\frac{12}{5\left(\frac{\zeta w}{2}\right)^2}\cdot\left[\cos\left(\frac{\zeta w}{2}\right)-\frac{2\sin(\zeta w/2)}{\zeta w/2}+\frac{\sin^2(\zeta w/4)}{(\zeta w/4)^2}\right]. \tag{99}$$

The method is easily extended to include the even- and odd-mode capacitance computation by considering the following representation for the Fourier transform of the charge density:

$$\tilde{\rho}^{\{e\atop o\}}(\zeta)=2\int_{s/2}^{s/2+w}\rho^{\{e\atop o\}}(x)\begin{matrix}\cos\\ \sin\end{matrix}\{\zeta x\}\,dx. \tag{100}$$

The Rayleigh–Ritz procedure has been employed with this method to determine the unknown constants, the a_i, in the expansions [36]–[38]

$$\rho^{(e)}(x)=\sum_{i=1}^{M+1}a_i x^{i-1} \tag{101}$$

and

$$\rho^{(0)}(x)=\sum_{i=1}^{M+1}a_i(w-x)^{i-1}. \tag{102}$$

For microstrip on an isotropic substrate without a cover layer, with $w/H>0.5$ and $s/H>0.5$, the reported error is less than 1 percent for the upper-bound even-mode characteristic impedance and 2 percent for the odd mode. However, for small s/H (less than 0.1), with $w/H>1.0$ or $w/H<0.1$, the error exceeds 6 percent [37]. Large errors result with this method for the case of microstrip with a cover [38]

The trial functions given by (98) and (99) have been considered to analyze the unshielded stripline on a Lithium–Niobate substrate (Li-Nb-O_3, $\epsilon_{xx}=28$, $\epsilon_{yy}=43$) [88]. The results obtained using the variational principle have been found to be in error by 4–10 percent when compared to the approach which uses image theory with the numerical technique discussed previously [30]. The corresponding formulation for even- and odd-mode upper-bound capacitance computation is given by [36]–[38]

$$C^{\{e\atop o\}}=\frac{\epsilon_0}{2\pi}\int_0^{\infty}\tilde{\phi}^{\{e\atop o\}}(\zeta)\tilde{g}(\zeta)\,d\zeta \tag{103}$$

where the trial functions for the potential may be chosen as

$$\phi^{\{e\atop o\}}(x)=\begin{cases}\sum_{i=L}^{L}a_i(d-x)^{-i}, & 0\leqslant x\leqslant s/2\\ 1, & s/2\leqslant x\leqslant s/2+w\\ \sum_{j=1}^{N+1}b_j(x-d)^{-j}, & x\geqslant s/2+w\end{cases} \tag{104}$$

with $L=M+1$ for even modes, $L=M+2$ for odd modes, and $d=(1/2)(s+w)$. The unknown constants a_i and b_j may be determined with the procedure used for the lower-bound computations. For isotropic substrates, the incurred error is found to be 2 percent for the even-mode impedance and 4 percent for the odd mode (by comparison with the results reported in [74] for $s/H\geqslant 0.5$ and $w/H\geqslant 0.5$). For smaller s/H and/or w/H, the error is substantially larger.

2) Space-Domain Formulation: A variational representation for the capacitance per unit length can also be given directly in terms of spatial coordinates, i.e., [12]

$$C=\frac{\int_{-w/2}^{w/2}\rho(x)\,dx}{\int_{-w/2}^{w/2}\int_{-w/2}^{w/2}G(x-x',y-y')\rho(x)\rho(x')\,dx\,dx'}. \tag{105}$$

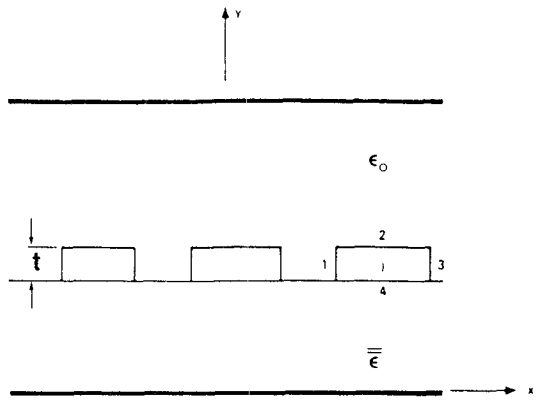

Fig. 11. Multiple conductor microstrip system.

It converges to the true value from the lower side. This variational representation has been implemented to analyze the properties of microstrip, inverted microstrip, and coplanar lines with multiple anisotropic layers in a rectangularly shaped shield [39]–[42].

The variational method can readily be extended to consider the characteristics of the system of N microstrip lines shown in Fig. 11. The conductor thickness may also be taken into account [34], [35]. The potential of the ith conductor is given for this configuration by

$$V_i = \sum_{j=1}^{N} \sum_{p=1}^{M} \int_{\mathscr{L}_{jp}} ds'_p G(s_r, s'_p) q_{jp}(s'_p) \tag{106}$$

with $i = 1, 2, 3, \cdots, N$. $\mathscr{L}_{jp}$ denotes integration on the pth side of the jth conductor, M the number of conductor sides ($M = 4$ for the rectangularly shaped strips considered here), and s'_p the integration variable along the pth side of the jth conductor. $s_r(s'_p)$ denotes $x(x')$ or $y(y')$ depending on whether the pth side is parallel to the x- or y-axis. Lastly, $q_{jp}(s'_p)$ is the unknown charge distribution of the pth side of the jth conductor and $G(s_r, s'_p)$ is the Green's function satisfying the Poisson equation. The total charge on the jth conductor is

$$Q_j = \sum_{p=1}^{4} \int_{\mathscr{L}_{jp}} q_{jp}(s'_p)\, ds'_p \tag{107}$$

which may be rewritten as

$$Q_j = \sum_{j} \sum_{p} \langle 1, q_{jp}(s_p) \rangle_{j,p}. \tag{108}$$

The inner product is defined here by

$$\langle V(s_p), W(s_p) \rangle_{j,p} = \int_{\mathscr{L}_{jp}} ds_p V(s_p) W(s_p). \tag{109}$$

The unknown charge density on the pth side may be written in terms of the following expansion:

$$q_{jp}(s_p) = \sum_{k=-M(j,p)}^{M(j,p)} c_k(j,p) \exp\{M_k(j,p) s_p\} \tag{110}$$

where $c_k(j,p)$ are unknown coefficients and $M_k(j,p)$ are known parameters on the pth side of the jth conductor. Utilizing the inner product definition and substituting (110) into (106), the V_i can be expressed as

$$V_i = \sum_{j=1}^{N} \sum_{p=1}^{4} \cdot \sum_{k=-M}^{M} c_k(j,p) \langle G(s_r, s'_p), \exp\{M_k(j,p) s'_p\} \rangle_{jp}. \tag{111}$$

Subsequently, the inner product of V_i with $\exp\{M_m(i,r) s_r\}$ yields

$$\langle \exp\{M_m(i,r) s_r\}, V_i \rangle_{ir} = \sum_{j=1}^{N} \sum_{p=1}^{4} \sum_{k=-M}^{M} c_k(j,p) \cdot \langle \exp\{M_m(i,r) s_r\}, \langle G(s_r, s'_p), \exp\{M_k(j,p) s'_p\} \rangle \rangle_{ir,jp} \tag{112}$$

where

$$\langle \ \rangle_{ir,jp} = \int_{\mathscr{L}_{ir}} \int_{\mathscr{L}_{jp}} ds_r\, ds'_p \exp\{M_m(i,r) s_r\} \cdot G(s_r, s'_p) \exp\{M_k(j,p) s'_p\}. \tag{113}$$

In order to simplify notation, the following matrices are defined, namely the column vector

$$[Y(m,i,r)] = [\langle \exp\{M_m(i,r) s_r\}, V_i \rangle_{ir}] \tag{114}$$

and the square matrix

$$[T(m,i,r,k,j,p)] = [\langle \ \rangle ir, jp]. \tag{115}$$

These definitions enable (112) to be rewritten in the matrix form

$$[T(m,i,r;k,j,p)][c_k(j,p)] = [Y(m,i,r)] \tag{116}$$

which, upon inversion, yields the solution for the unknown coefficients

$$[c_k(j,p)] = [T(m,i,r;k,j,p)]^{-1} [Y(m,i,r)]. \tag{117}$$

The total charge on the jth conductor is finally obtained as

$$Q_j = \sum_{k=-M}^{M} \sum_{p=-1}^{4} c_k(j,p) \langle 1, \exp\{u_k(j,p) s_p\} \rangle_{jp}. \tag{118}$$

In view of the assumption that $V_j = 1$ and $V_1 = \cdots = V_{j-1} = \cdots = \cdots = V_N = 0$, the variational expression (105) is rewritten for $C_{ij} = Q_i$ as

$$Q = \frac{\left(\sum_{r=1,\, r \in \mathscr{L}_{ir}}^{4} \int_{\mathscr{L}_{ir}} ds_r q_r(s_r) \right)^2}{\sum_{\substack{r=1 \\ r \in \mathscr{L}_{ir}}}^{4} \int_{\mathscr{L}_{ir}} ds_r q_{ir}(s_r) \sum_{j=1}^{N} \sum_{\substack{p=1 \\ p \in \mathscr{L}_{jp}}}^{4} \int_{\mathscr{L}_{jp}} ds'_p G(s_r, s'_p) q_{jp}(s'_p)}. \tag{119}$$

TABLE VIII
CONVERGENCE PATTERN FOR CAPACITANCE PER METER FOR MICROSTRIP ON SAPPHIRE

$u_k(2)=u_k(4)$				$u_k(1)=u_k(3)$	q_1+q_3 (nC)	q_2+q_4 (nC)	C(nF/m)
0.0	0.6			± 0.83,	0.01847	0.1832	0.2017
0.0	0.6	1.2	1.8	± 0.55, ± 1.66	0.02109	0.1789	0.2000
0.0	1.0			± 0.083	0.02093	0.1790	0.1999
0.0	1.0			± 0.055, ± 0.17	0.10977	0.1812	0.2010

$t/H=0.3$, $w/H=1.0$, $B/H=6.0$.

This expression is useful in obtaining the effect of the conductor thickness on the propagation characteristics of microstrip conductors [34], [35]. The Green's function pertinent for this purpose is [34]

$$G(x-x',y-y')=\frac{1}{\pi\epsilon_0}\int_0^\infty \cos\left[\frac{\zeta|x-x'|}{n_x}\right]\sinh\left(\frac{\zeta(B-y_>)}{n_x}\right) \cdot\frac{n_xn_y\sinh\left(\frac{\zeta(y_>-H)}{n_x}\right)\cosh\left(\frac{\zeta H}{n_y}\right)+\sinh\left(\frac{\zeta H}{n_y}\right)\cosh\left(\frac{\zeta(y_<-H)}{n_x}\right)}{n_xn_y\sinh\left(\frac{\zeta(B-H)}{n_x}\right)\cosh\left(\frac{\zeta H}{n_y}\right)+\sinh\left(\frac{\zeta H}{n_y}\right)\cosh\left(\frac{\zeta(B-H)}{n_x}\right)}\frac{d\zeta}{\zeta} \quad (120)$$

where $y_<=\min(y,y')$, $y_>=\max(y,y')$, $n_x=\sqrt{\epsilon_{xx}}$, and $n_y=\sqrt{\epsilon_{yy}}$.

A single conductor of thickness t is considered presently as an application of the just-outlined approach. On the vertical sides ($p=1,3$), the charge distribution is expressed as

$$q_p(y)=\sum_{k=-M}^{M} c_k(p)\exp\{u_k(p)y\}, \qquad p=1,3$$

while on the horizontal sides ($p=2,4$), q is given by

$$q_p(x)=\sum_{k=-M}^{M} c_k(p)\exp\{u_k(p)x\}.$$

Table VIII demonstrates the capacitance convergence pattern of this technique. Even with the choice of $u_k=0.0$, the value of Z_0 is found to be within 5 percent of its convergence value. An example of the dependence of Z_0 and v_p on t/H is shown in Figs. 12 and 13, for $w/H=1.0$ and $B/H=6.0$. Clearly, for $w/H=1.0$, the variation of Z_0 and v_p with t/H is a second-order effect. Convergence is obtained, using this technique, with two or three u_k points. In addition, it has been determined that for increasing values of w/H, faster convergence is achieved if the parameters u_k are chosen as $u_k=H/w$ [34], [35].

3) Extension to Coplanar Waveguides: The variational principle can be extended to yield an expression for the capacitance of the coplanar waveguide (CP) in the form of [89]

$$C=\frac{\int_{s/2}^{s/2+w}\int_{s/2}^{s/2+w}\int_0^\infty e_x(x)G(\zeta;x-x')e_x(x')\,dx\,dx'}{\left\{\int_{s/2}^{s/2+w}e_x(x)\,dx\right\}^2} \quad (123)$$

where $e_x(x)$ is the unknown electric-field distribution across the slot aperture and

$$G(\zeta;x-x')=\frac{4\epsilon_0}{\pi}\left\{1+\frac{1+\epsilon_{eq}\tanh(\zeta H_{eq})}{1+\frac{1}{\epsilon_{eq}}\tanh(\zeta H_{eq})}\right\}\frac{\sin\zeta x\sin\zeta x'}{\zeta}. \quad (124)$$

The aperture electric field is written as the expansion

$$e_x(x)=e_0(x)+\sum_{k=1}^{N}a_ke_k(x) \quad (125)$$

where

$$e_k(x)=\frac{T_k\left\{\frac{2(x-s)}{w}\right\}}{\left[1-\left\{\frac{2(x-s)}{w}\right\}^2\right]^{1/2}}. \quad (126)$$

The Chebyshev polynomials $T_k\{x\}$ of the first kind are used, and the parameters are calculated using the Rayleigh–Ritz method. This technique yields results which are identical to those obtained by conformal mapping when $N\geq 2$ in the absence of the substrate, and it is considered to be highly accurate when the anisotropic substrate is included [89]. The variation of ϵ_{eff} and Z_0 versus θ, as obtained by this method, are shown in Fig. 14 for a sapphire substrate (θ is defined here as in (53)).

V. MODELING DISPERSION

The quasi-static methods described previously provide solutions of limited validity since they do not account for dispersive effects. Simple frequency-dependent formulas based on empirical observation and curve fitting have been derived, but they too are of limited value. They either apply exclusively to a sapphire substrate [2], [4] or they are not accurate enough for electrically thick substrates. Although they may lack general applicability, these methods and formulas offer the convenience of closed-form alge-

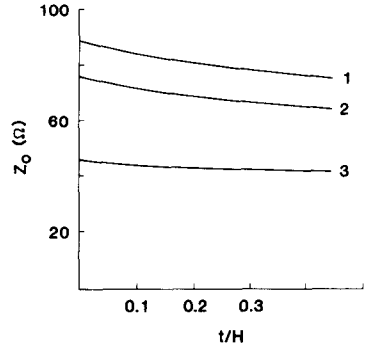

Fig. 12. Z_o versus (t/H) for 1: Polystyrene ($\epsilon_{xx} = \epsilon_{yy} = 2.54$); 2: quartz ($\epsilon_{xx} = \epsilon_{yy} = 3.78$); 3: sapphire ($\epsilon_{xx} = 9.4$, $\epsilon_{yy} = 11.6$). Reprinted by permission from the *Journal of the Franklin Institute* [34].

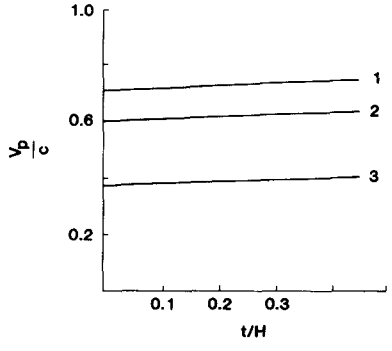

Fig. 13. $v_{p/c}$ versus (t/H) for the microstrip of Fig. 12. Reprinted by permission from the *Journal of the Franklin Institute* [34].

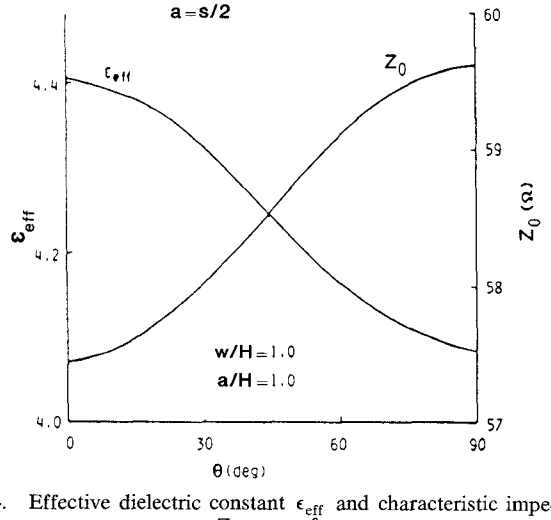

Fig. 14. Effective dielectric constant ϵ_{eff} and characteristic impedance Z_o versus θ.

braic expressions. For reference, then, some of these are presented.

An empirical formula for the frequency-dependent effective dielectric constant for a sapphire substrate is given as [5]

$$\epsilon_{eff} = \epsilon_{req} - \frac{\epsilon_{req} - \epsilon_{e0}}{1 + \left(\frac{H}{Z_0}\right)^{1.33}\left[0.43f^2 - 0.009f^3\right]} \tag{127}$$

where ϵ_{req} is defined by (40) and ϵ_{e0} is the static effective dielectric constant. H is in millimeters and f in gigahertz. This formula is reportedly valid with $a \pm 0.8$-percent error over the frequency range $2 \leqslant f \leqslant 18$ GHz and for a characteristic impedance value of $10 < Z_0 < 100\ \Omega$ [2], [5]. A dynamic solution obtained by the method of moments to within 0.5-percent accuracy [56] indicates that the error estimate in using (127) is within $\leqslant 3.3$ percent for $w/H = 0.5$, $\leqslant 1.5$ percent for $w/H = 1.0$, and $\leqslant 2.5$ percent for $w/H = 5.0$.

An approximate empirical formula which applies for arbitrary substrate anisotropy and thickness has been derived by combining two different dispersive models for isotropic substrates. The effective dielectric constant is defined as [90]

$$\epsilon_{\text{eff}} = \begin{cases} \dfrac{4}{[I_1 + I_2]^2}, & \text{if } I_1 > I_2 \\ \dfrac{1}{I_2^2}, & \text{if } I_1 < I_2 \end{cases} \tag{128}$$

where I_1 and I_2 are dispersive models for isotropic substrates [91], [92]. I_1 is expressed in the form

$$I_1 = \frac{\dfrac{1}{\sqrt{\epsilon_{yy}}}\left(\dfrac{f}{f_k}\right)^2 + \dfrac{1}{\sqrt{\epsilon_{e0}}}}{\left(\dfrac{f}{f_k}\right)^2 + 1} \tag{129}$$

with

$$f_k = \frac{v_0 \tan^{-1}\left[\epsilon_{req}\left(\dfrac{\epsilon_{e0} - 1}{\epsilon_{req} - \epsilon_{e0}}\right)^{1/2}\right]}{2\pi H\left(1 + \dfrac{w}{H}\right)\left[\epsilon_{req} - \epsilon_{e0}\right]^{1/2}}. \tag{130}$$

For I_2, the expression is

$$I_2 = \frac{\left(\dfrac{f}{f_y}\right)^{3/2} + 4}{\left(\dfrac{f}{f_y}\right)^{3/2}\sqrt{\epsilon_{yy}} + 4\sqrt{\epsilon_{e0}}} \tag{131}$$

with

$$f_y = \frac{v_0}{4H(\epsilon_{req} - 1)^{1/2}\left[\dfrac{1}{2} + \left(1 + 2\log\left(1 + \dfrac{w}{H}\right)\right)^2\right]}. \tag{132}$$

In these definitions, ϵ_{req} is the equivalent relative dielectric constant at zero frequency for an isotropic substrate on which the microstrip line (w, H being identical to the original line) has the same effective dielectric constant ϵ_{e0} as the latter line at zero frequency. Also, v_0 is the speed of light in vacuum.

The accuracy of the ϵ_{eff} formula given by (128) is very good for large w/H and arbitrary H/λ_0. When $H/\lambda_0 > 0.03$ and $w/H < 1.0$, however, the error for a sapphire is of the order of 4 percent. Clearly, for cases of arbitrary anisotropic substrates, a more precise accounting of dispersion is required. Rigorous solutions to Maxwell's equations addressing that need will now be presented.

A. The Transmission-Line Matrix (TLM) Technique

The TLM method, as it applies to anisotropic substrates [44] provides a solution to Maxwell's equations in the time domain by determining the impulse response of an equivalent distributed transmission-line network that models the given waveguiding structure [44]–[49]. The equivalence is obtained in terms of ideal two-wire transmission lines of length Δl connected in a three-dimensional lattice arrangement. At the transmission-line crossings, shunt or series nodes are formed which enable accurate characterization of the propagating medium with the incorporation of open- or short-circuited transmission-line stubs at each node. These transmission-line stubs are most instrumental in that they model the relative permittivity, conductivity, and relative permeability of the substrate. In the analysis, Kirchoff's voltage and current laws are applied to the equivalent three-dimensional network to yield a set of equations identifiable as an analog to Maxwell's equations (as they apply to the guiding structure).

The equivalent three-dimensional circuit is a periodic structure and it therefore exhibits the inherent passband and stopband frequency response characteristic of periodic networks. The upper frequency cutoff f_2 of the TLM model is the highest frequency of the lowest passband and it is determined by the mesh size Δl. It is possible to increase f_2 by choosing a smaller mesh size ($f_2 \to \infty$ as $\Delta l \to 0$). Moreover, for a given frequency having a finer mesh or smaller, Δl increases the model accuracy but at the expense associated with rapidly increasing computer run times and storage requirements. Distinct advantages, however, such as simplicity, versatility, and direct modeling of the physical waveguiding processes make this method a very useful engineering tool.

The TLM technique will be adopted herein to solve Maxwell's equations in the general form given by (7)–(19) for the microstrip structure shown in Fig. 1(c). A generalized node is shown in Fig. 15(a). It consists of three shunt and three series nodes $\Delta l/2$ apart from one another. Permeability is modeled by a short-circuited stub attached to each series node, while an open-circuited stub attached to each shunt node models permittivity. In addition, conductivity may be modeled with an infinite or matched line connected to each shunt node, and referred to as a loss stub. The coordinate orientation of the stubs denotes the particular component of the diagonalized tensor modeled by the stub, while the dashed lines in Fig. 15(a) are guide lines (and not equivalent transmission lines or stubs) [44]. The transmission-line representation of this generalized node is shown in Fig. 15(b). It illustrates the three-dimensional formation of shunt and series nodes (for clarity, stubs are not included in this figure). The voltages at the three shunt nodes represent the ***E***-field components, while the currents at the three series nodes are associated with the ***H***-field components in the three coordinate directions as shown in Fig. 15(b). Guide discontinuities and substrate material properties can be modeled with the appropriate choice of the stub electrical parameters (admittance or impedance). A better understanding of this may be attained by considering a series and a shunt node individually. The series node shown in Fig. 16(a) is analyzed by considering the equivalent lumped network schematic of Fig. 16(c). The short-circuited stub of length $\Delta l/2$ is in the $\hat{x}$-direction and its input impedance is $Z_{\text{in}} = jZ_{xx}(L/C)^{1/2}\tan(\omega\Delta l/2c)$, where Z_{xx} is the line characteristic impedance. If $\omega\Delta l/2c \ll 1$, then $Z_{\text{in}} = j\omega L'$, where $L' = (Z_{xx}\Delta l/2)L$. Kirchoff's voltage law then yields for this series node

$$\frac{\partial v_z}{\partial y} - \frac{\partial v_y}{\partial z} = -2L\left(1 + \frac{Z_{xx}}{4}\right)\frac{\partial i_x}{\partial t}. \tag{133}$$

This network equation is an analog to Maxwell's equations. Upon identification of v_z with $\mathscr{E}_z$, v_y with $\mathscr{E}_y$, and i_x with $\mathscr{H}_x$, it follows that (133) and (14) are equivalent, provided [44], [45]

$$\mu_0 = 2L \tag{134}$$

and

$$\mu_{xx} = \frac{4 + Z_{xx}}{4}. \tag{135}$$

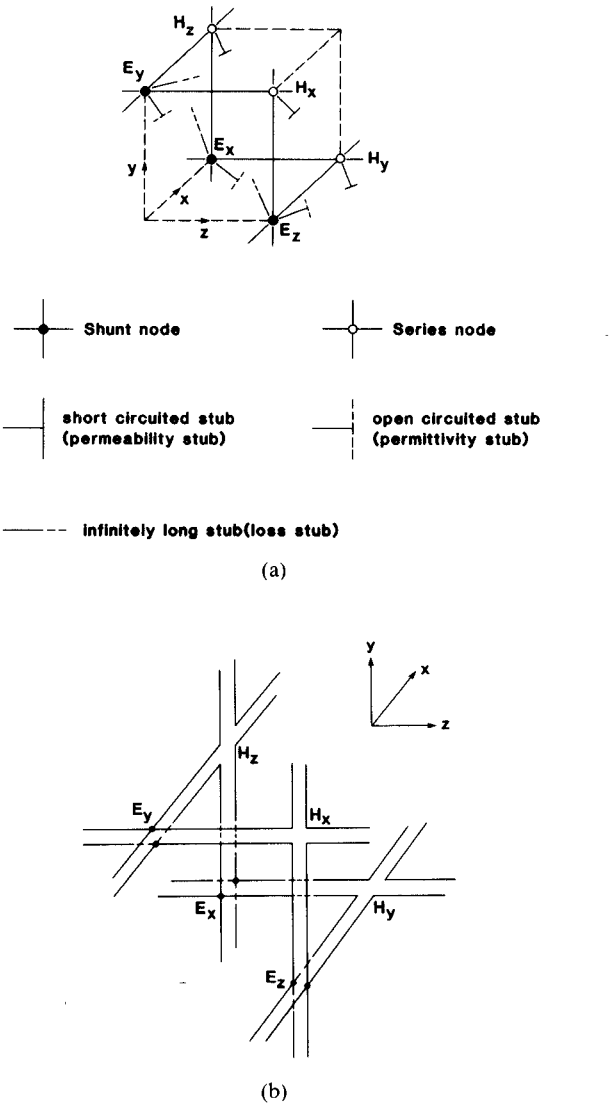

Fig. 15. (a) A generalized three-dimensional node. (b) Three-dimensional node.

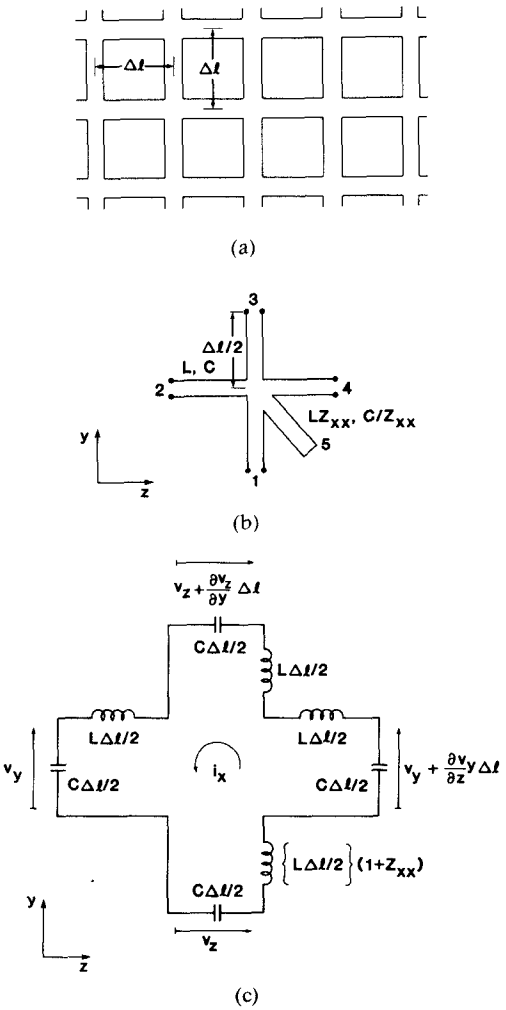

Fig. 16. (a) TEM lines connected in series. (b) A generalized series node. (c) Series node lumped network representation.

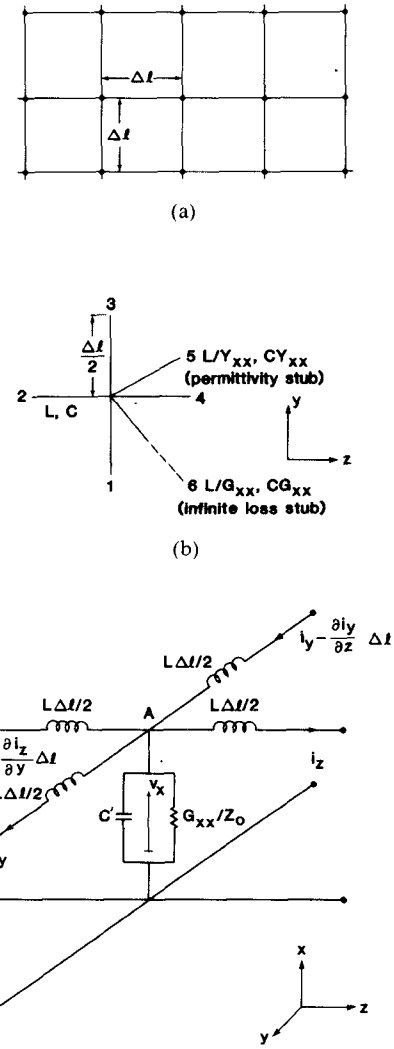

Fig. 17. (a) TEM lines connected in parallel. (b) A generalized shunt node. (c) Shunt node lumped network representation.

A similar analysis for series nodes in the xy- and xz-planes yields upon application of Kirchoff's voltage law

$$\frac{\partial v_y}{\partial x} - \frac{\partial v_x}{\partial y} = -2L\left(1+\frac{Z_{zz}}{4}\right)\frac{\partial i_z}{\partial t} \tag{136}$$

and

$$\frac{\partial v_x}{\partial z} - \frac{\partial v_z}{\partial x} = -2L\left(1+\frac{Z_{yy}}{4}\right)\frac{\partial i_y}{\partial t}. \tag{137}$$

Comparison with Maxwell's equations indicates the equivalences $v_y \equiv \mathscr{E}_y$, $v_x \equiv \mathscr{E}_x$, $i_z \equiv \mathscr{H}_z$, and $i_y \equiv \mathscr{H}_y$ hold if the following identifications are made:

$$\mu_{zz} = \frac{4+Z_{zz}}{4} \tag{138}$$

and

$$\mu_{yy} = \frac{4+Z_{yy}}{4}. \tag{139}$$

Continuing, the yz-plane shunt node shown in Fig. 17(b) is considered. In this case, the open-circuited stub (for permittivity) and the loss stubs (for conductivity) are in the $\hat{x}$-direction. The input admittance of the open-circuited stub is given by $Y_{\text{in}} = j\omega Y_{xx} C\Delta l/2 (\omega \Delta l/2c \ll 1)$, so that the equivalent capacitance is $C' = Y_{xx} C\Delta l/2$, while the total node capacitance is $2C(1+Y_{xx}/4)\,\Delta l$. Application of Kirchoff's, current law at node A yields

$$\frac{\partial i_z}{\partial y} - \frac{\partial i_y}{\partial z} = \left(\frac{G_{xx}}{Z_0 \Delta l} + 2C\left[1+\frac{Y_{xx}}{4}\right]\frac{\partial}{\partial t}\right)v_x. \tag{140}$$

A similar procedure in the other two planes produces the equations

$$\frac{\partial i_x}{\partial z} - \frac{\partial i_z}{\partial x} = \left(\frac{G_{yy}}{Z_0 \Delta l} + 2C\left[1+\frac{Y_{yy}}{4}\right]\frac{\partial}{\partial t}\right)v_y \tag{141}$$

and

$$\frac{\partial i_y}{\partial x} - \frac{\partial i_x}{\partial y} = \left(\frac{G_{zz}}{Z_0 \Delta l} + 2C\left[1+\frac{Y_{zz}}{4}\right]\frac{\partial}{\partial t}\right)v_z. \tag{142}$$

Comparing (140)–(142) with Maxwell's equations suggests the following parameter equivalences: $\mathscr{E}_x \equiv v_x$, $\mathscr{H}_z \equiv i_z$, $\mathscr{H}_y \equiv i_y$, $\sigma_{xx} \equiv G_{xx}/Z_0 \Delta l$, $\epsilon_0 = 2C$, and $\epsilon_{xx} = (4+Y_{xx})/4$. Similarly, $\mathscr{H}_x \equiv i_x$, $\mathscr{E}_y \equiv v_y$, $\sigma_{yy} \equiv G_{yy}/Z_0 \Delta l$, $\epsilon_{yy} \equiv (4+Y_{yy})/4$, and $\mathscr{E}_z \equiv v_z$, $\sigma_{zz} \equiv G_{zz}/Z_0 \Delta l$, and $\epsilon_{zz} \equiv (4+Y_{zz})$.

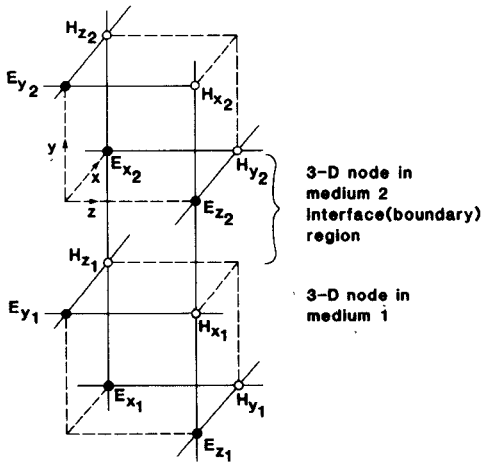

Fig. 18. Continuity of tangential fields across a dielectric boundary.

The previous discussion dealt with the derivation of the equivalent distributed circuit which models Maxwell's equations in the point form. Thus, the equivalent circuit, which is an analog to the differential form of Maxwell's equations, is obtained in terms of a generalized node with three shunt and three series nodes. A permittivity and a conductivity stub are connected to the shunt node, while a permeability stub is connected to the series node to complete the model. With this, a propagating medium can be represented accurately. By connecting appropriately characterized generalized nodes in a three-dimensional mesh, the individual homogeneous regions of the actual waveguiding structure can be modeled. To complete the model, boundary conditions need to be incorporated. A short circuit (electric wall) is obtained by shorting out the shunt nodes in the plane of interest, while an open circuit (magnetic wall) is achieved by open circuiting the appropriate series nodes in the plane of interest. Dielectric interfaces are dealt with in terms of the continuity of tangential field components. An example [44] is the xz-plane boundary between two dielectric materials. In this case, elementary transmission-line sections connect a generalized node in one medium to a generalized node in the second medium as Fig. 18 indicates. If the tangential field components for E_x, E_z, H_x, and H_z are considered on either side of the boundary, then the following equations are obtained:

$$E_{z_2} = E_{z_1} + \frac{\partial E_{z_1}}{\partial y}\Delta l \tag{143}$$

$$E_{x_2} = E_{x_1} + \frac{\partial E_{x_1}}{\partial y}\Delta l \tag{144}$$

$$H_{x_2} = H_{z_1} + \frac{\partial H_{x_1}}{\partial y}\Delta l \tag{145}$$

$$H_{z_2} = H_{z_1} + \frac{\partial H_{z_1}}{\partial y}\Delta l. \tag{146}$$

These relations are obtained from the correspondence of the electric field at a shunt node to voltage, and of the magnetic field at a series node to current.

The TLM method predicts, as stated previously, the impulse response of a given network. According to this technique, an impulse excitation takes place at some circuit location. It propagates throughout the transmission-line sections scattering at the shunt and series node locations. The manner according to which the impulse is scattered at a given node is prescribed by the scattering matrix pertinent to that node. The scattering matrix of a shunt node is

$$[S]_{\text{shunt}} = \frac{2}{Y}\begin{bmatrix} 1 & 1 & 1 & 1 & Y_{ll} \\ 1 & 1 & 1 & 1 & Y_{ll} \\ 1 & 1 & 1 & 1 & Y_{ll} \\ 1 & 1 & 1 & 1 & Y_{ll} \\ 1 & 1 & 1 & 1 & Y_{ll} \end{bmatrix} - [I] \tag{147}$$

where $Y = 4 + Y_{ll} + G_{ll}$, ll denotes $\hat{x}\hat{x}$, $\hat{y}\hat{y}$, or $\hat{z}\hat{z}$, and $[I]$ is the unitary matrix. For a series node

$$[S]_{\text{series}} = \frac{2}{Z}\begin{bmatrix} -1 & 1 & 1 & -1 & -1 \\ 1 & -1 & -1 & 1 & 1 \\ 1 & -1 & -1 & 1 & 1 \\ -1 & 1 & 1 & -1 & -1 \\ -Z_{ll} & Z_{ll} & Z_{ll} & -Z_{ll} & -Z_{ll} \end{bmatrix} + [I] \tag{148}$$

where $Z = 4 + Z_{ll}$.

The voltage–current analog of any electromagnetic field of interest can be excited by imposing the properly weighted voltage and current impulses at the node points of the equivalent network. These impulse fields can be followed as they travel and scatter through the network, and allow a determination of the field value at any point of the guiding structure by way of the analog and the corresponding network point. The response is obtained at the point of observation as the collection of the impulse amplitudes incident at that point. Fourier transformation of this result yields easily the Fourier domain response.

The TLM method just described has been applied to determine the dispersion characteristics of single and coupled microstrip lines, as well as of microstrip discontinuities on an anisotropic substrate as defined by a diagonalized permittivity tensor [44]. The geometry under consideration is illustrated in Fig. 1(c). Due to the even symmetry in x, a magnetic wall is placed at $x = 0$, and as such the input data involves boundary conditions which take the form $E_x = E_z = 0$ at $y = 0$, B, $E_y = E_z = 0$ at $x = a$, $H_y = H_z = 0$ at $x = 0$, and $E_x = E_z = 0$ at $y = H$, $0 \leqslant x \leqslant w/2$. Shorting planes are placed $2L_r$ units apart along the length of the microstrip transmission line to form a resonator. At the lowest resonant frequency of this cavity, the quantity $2L_r$ corresponds to half the guided wavelength of the fundamental propagating mode on the microstrip line, thereby yielding the dispersion characteristics of the line (i.e., at resonance $\beta = \pi/2L_r$).

Results for the particular case where $w/H = 3$, $\Delta l = H$, and $B/H = 6$ are shown in Fig. 19. For these computations, one thousand iterations were used (only a 0.01-percent change in resonant frequency is observed if more iterations are used [44]). The difference in the values as

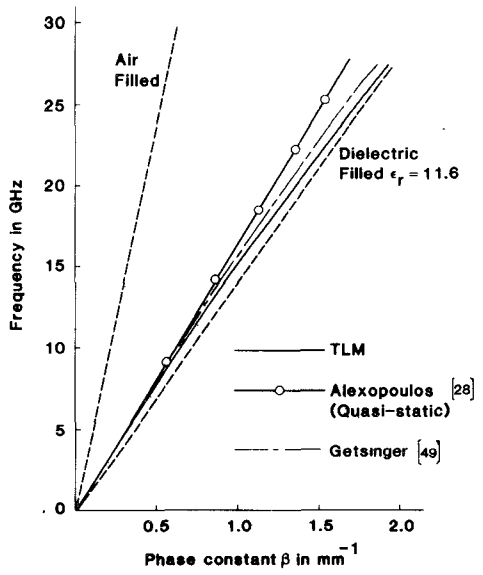

Fig. 19. Dispersion diagram for single microstrip on sapphire substrate $w/H = 3.0$, $H = \Delta 1$.

compared to an isotropic substrate case reported in the literature [50] are 7 percent for $H = \Delta l$, improved to 2 percent for $H = 2\,\Delta l$, and finally 0.5 percent if $H = 3\Delta l$ is chosen. A crucial point in convergence enhancement is, in this case, in *a priori* knowledge of the fundamental-mode field distribution. It has been found that a more accurate representation of the fundamental mode results if E_y is excited at all nodes lying directly below the strip conductor and E_x is excited along the edge of the strip.

The TLM method has also been used to predict the dispersion properties of microstrip discontinuities [44] such as those shown in Fig. 20. An example of dispersion for coupled microstrip on sapphire is shown in Fig. 21. There the dimensions are: $a = 17\Delta l$, $H = 3\Delta l$, $B = 6\Delta l$, $s = 3\Delta l$, $w = 3\Delta l$, and $\Delta l = 0.5$ mm.

The TLM technique as described is a very simple and versatile method which is easily adopted to obtain the dispersion characteristics of single or coupled microstrip lines, as well as of microstrip discontinuities on anisotropic substrates. An important disadvantage of the technique is the need for *a priori* knowledge or very good initial guess of the dominant-mode field distribution to enhance convergence. In addition, the accuracy is dependent on the number of iterations used to ensure convergence for the selected mesh size. Obviously, the finer the chosen mesh size, the more accurate the solution, at the expense of computer run time and memory storage requirements.

B. *Fourier-Domain Methods*

The frequency-dependent characteristics of integrated-circuit structures on anisotropic substrates can be analyzed, in addition to the transmission-line matrix method, by solving Maxwell's equations with Fourier-spectrum techniques. The electromagnetic-field components may be expressed either in terms of a continuous or a discrete Fourier spectrum depending on whether the waveguiding

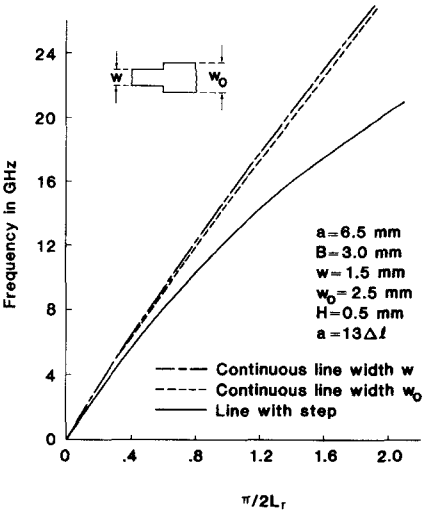

(a)

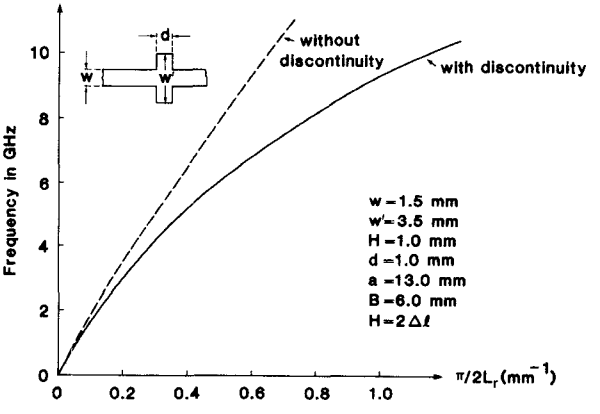

(b)

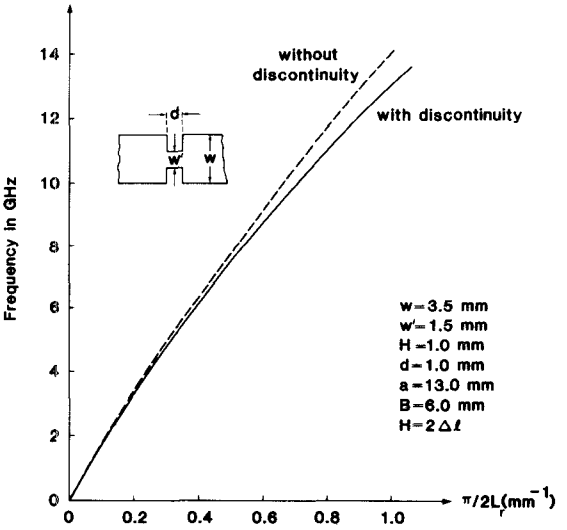

(c)

Fig. 20. Dispersion diagrams for the shown structures.

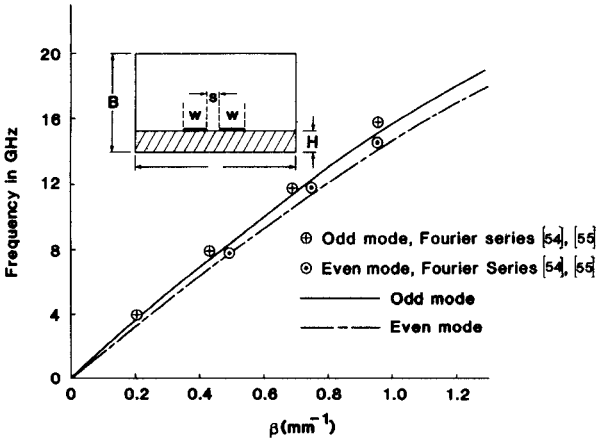

Fig. 21. Dispersion diagram for even and odd fundamental modes of edge-coupled microstrip ($a=17\Delta 1$, $H=3\Delta 1$, $B=9\Delta 1$, $s=3\Delta 1$, $w=3\Delta 1$, $\Delta 1=0.5$ mm, sapphire substrate).

circuit under consideration is an open or a closed structure. Due to the inhomogeneity in the $\hat{y}$-dimension of the structures under consideration, the complete field solution is obtained by the superposition of LSE and LSM modes. In this section, methods of solution for microstrip, microstrip with cover, microstrip in a rectangularly shaped shield, and the corresponding cases of coplanar waveguide and slotline are investigated. The substrate is characterized by a diagonalized tensor $\bar{\bar{\epsilon}}$, while the material magnetic and conductive properties are assumed isotropic ($\mu_r=1$, $\sigma=0$).

1) Continuous Fourier Spectrum — Microstrip and Coplanar Slots: The dispersive properties of microstrip with cover may be obtained by adopting the continuous Fourier spectrum in conjunction with the Wiener–Hopf method [51]. Structures such as microstrip with or without cover, inverted microstrip, coupled microstrip, coplanar lines, and coplanar slots may be analyzed by combining the continuous Fourier-spectrum field representation with the equivalent network method of solution of Maxwell's equations [52]–[54].

a) Modified Wiener–Hopf method; Microstrip with cover: For time-harmonic fields and propagation in the $+\hat{z}$-direction, Maxwell's equations are simplified by allowing $\partial/\partial t \rightarrow j\omega$ and $\partial/\partial t \rightarrow -j\beta$. Further simplification is obtained if the electromagnetic-field quantities E and H are written as the inverse Fourier transforms

$$\mathscr{A}(x,y)=\frac{1}{2\pi}\int_{-\infty}^{\infty}\tilde{\mathscr{A}}(\zeta,y)e^{j\zeta x}\,d\zeta \tag{149}$$

where $\mathscr{A}$ may represent E or H. With this substitution, the LSE and LSM modes are expressed in the spectral domain as follows.

LSE Modes (TE_y):

$$\tilde{E}_x^{TE_y}=\frac{\omega\mu_0\beta}{\zeta^2+\beta^2}\tilde{H}_y^{TE_y} \tag{150}$$

$$\tilde{E}_z^{TE_y}=\frac{\omega\mu_0\zeta}{\zeta^2+\beta^2}\tilde{H}_y^{TE_y} \tag{151}$$

$$\tilde{H}_x^{TE_y}=\frac{j\zeta}{\zeta^2+\beta^2}\frac{\partial\tilde{H}^{TE_y}}{\partial y} \tag{152}$$

and

$$\tilde{H}_z^{TE_y}=\frac{-j\beta}{\zeta^2+\beta^2}\frac{\partial\tilde{H}_y^{TE_y}}{\partial y} \tag{153}$$

where $\tilde{H}_y^{TE_y}$ satisfies the wave equation

$$\frac{\partial^2\tilde{H}_y^{TE_y}}{\partial y^2}-\left[\zeta^2+\beta^2-\epsilon_t k_0^2\right]\tilde{H}_y^{TE_y}=0. \tag{154}$$

Similarly, the following can be expressed.

LSM Modes (TM_y):

$$\tilde{E}_x^{TM_y}=\frac{j\zeta(\epsilon_{yy}/\epsilon_t)}{\zeta^2+\beta^2}\frac{\partial\tilde{E}_y^{TM_y}}{\partial y} \tag{155}$$

$$\tilde{E}_z^{TM_y}=-\frac{j\beta(\epsilon_{yy}/\epsilon_t)}{\zeta^2+\beta^2}\frac{\partial\tilde{E}_y^{TM_y}}{\partial y} \tag{156}$$

$$\tilde{H}_x^{TM_y}=-\frac{\omega\epsilon_0\epsilon_{yy}\beta}{\zeta^2+\beta^2}\tilde{E}_y^{TM_y} \tag{157}$$

and

$$\tilde{H}_z^{TM_y}=-\frac{\zeta\omega\epsilon_0\epsilon_{yy}}{\zeta^2+\beta^2}\tilde{E}_y^{TM_y} \tag{158}$$

where, for this case, $\tilde{E}_y^{TM_y}$ satisfies the wave equation

$$\frac{\partial^2\tilde{E}_y^{TM_y}}{\partial y^2}-\left(\frac{\epsilon_t}{\epsilon_{yy}}\right)\left[\zeta^2+\beta^2-\epsilon_{yy}k_o^2\right]\tilde{E}_y^{TM_y}=0 \tag{159}$$

and $\epsilon_t=\epsilon_{xx}=\epsilon_{zz}$. The LSE and LSM modes are superposed to yield the following system of equations:

$$\omega\mu_0\tilde{H}_y^{TE_y}=\beta\tilde{E}_x+\zeta\tilde{E}_z \tag{160}$$

$$j\left(\frac{\epsilon_{yy}}{\epsilon_t}\right)\frac{\partial\tilde{E}_y^{TM_y}}{\partial y}=\zeta\tilde{E}_x-\beta\tilde{E}_z \tag{161}$$

$$-\omega\epsilon_0\epsilon_{yy}\tilde{E}^{TM_y}=\beta\tilde{H}_x+\zeta\tilde{H}_z \tag{162}$$

and

$$j\frac{\partial\tilde{H}_y^{TE_y}}{\partial y}=\zeta\tilde{H}_x-\beta\tilde{H}_z \tag{163}$$

with $\tilde{E}_x$, $\tilde{E}_z$, $\tilde{H}_x$, $\tilde{H}_z$ representing the transform of the total field components. These relations are needed so as to determine the boundary conditions which $\tilde{E}_y^{TM_y}$ and $\tilde{H}_y^{TE_y}$ must satisfy. The wave equations to be solved in regions 1 and 2 of the geometry shown in Fig. 1(b) are given by

$$\frac{d^2\tilde{E}_{y_1}^{TM_y}}{dy^2}-\left(\frac{\epsilon_t}{\epsilon_{yy}}\right)R_y^2\tilde{E}_{y_1}^{TM_y}=0 \tag{164}$$

$$\frac{d^2\tilde{H}_{y_1}^{TE_y}}{dy^2}-R_t^2\tilde{H}_{y_1}^{TE_y}=0 \tag{165}$$

where $R_t^2=\zeta^2+\beta^2-\epsilon_t k_0^2$, $R_y^2=\zeta^2+\beta^2-\epsilon_{yy}k_0^2$ and

$$\frac{d^2\tilde{E}_{y_2}^{TM_y}}{dy^2}-R_0^2\tilde{E}_{y_2}^{TM_y}=0 \tag{166}$$

$$\frac{d^2\tilde{H}_{y_2}^{TM_y}}{dy^2}-R_0^2\tilde{H}_{y_2}^{TE_y}=0 \tag{167}$$

with $R_0^2 = \zeta^2 + \beta^2 - k_0^2$. The boundary conditions impose the following requirements.

At $y = 0, B$:

$$\tilde{H}_y^{\mathrm{TE}_y} = \frac{\partial \tilde{E}_y^{\mathrm{TM}_y}}{\partial y} = 0 \text{ for conductive wall.}$$

At $y = H$ and $|x| > w/2$:

$$\left(\frac{\epsilon_{yy}}{\epsilon_t}\right)\frac{\partial \tilde{E}_y^{\mathrm{TM}_y}}{\partial y},\ \tilde{H}_y^{\mathrm{TE}_y},\ \frac{\partial \tilde{H}_y^{\mathrm{TE}_y}}{\partial y}, \text{ and } \epsilon_{yy}\tilde{E}_y^{\mathrm{TM}_y}$$

must be continuous.

At $y = H$, $|x| \leqslant w/2$:

$$\tilde{H}_y^{\mathrm{TE}_y},\left(\frac{\epsilon_{yy}}{\epsilon_t}\right)\frac{\partial \tilde{E}_y^{\mathrm{TM}_y}}{\partial y}$$

are continuous and $\tilde{J}_x = \tilde{H}_z$, $\tilde{J}_z = -\tilde{H}_x$, where $\tilde{J}_x$ and $\tilde{J}_z$ are the transforms of the current density distribution on the microstrip. Solution to the aforementioned boundary-value problem yields the following relations [51]:

$$U_1(\zeta) = j\omega\epsilon_0\left[\frac{\coth(R_0 H\nu)}{R_0} + \frac{\sqrt{\epsilon_t\epsilon_{yy}}}{R_y}\coth(R_y H_{\mathrm{eq}})\right]F_1(\zeta) \tag{168}$$

and

$$j\omega\mu_0 U_2(\zeta) = \left[R_0\coth(R_0 H\nu) + R_t\coth(R_t H)\right]F_2(\zeta) \tag{169}$$

where the quantities $U_i(\zeta)$, $F_i(\zeta)$, $i = 1,2$, are defined by ($\nu = B/H - 1$)

$$U_1(\zeta) = \omega\epsilon_0\left(\tilde{E}_{y_2}^{\mathrm{TM}_y} - \epsilon_{yy}\tilde{E}_{y_1}^{\mathrm{TM}_y}\right)_{y=H} = -\zeta\tilde{J}_x + \beta\tilde{J}_z \tag{170}$$

$$U_2(\zeta) = -j\left(\frac{\partial \tilde{H}_{y_2}^{\mathrm{TE}_y}}{\partial y} - \frac{\partial \tilde{H}_{y_1}^{\mathrm{TE}_y}}{\partial y}\right)_{y=H} = \beta\tilde{J}_x + \zeta\tilde{J}_z \tag{171}$$

$$F_1(\zeta) = j\left[\frac{\partial \tilde{E}_{y_2}^{\mathrm{TM}_y}}{\partial y} - \left(\frac{\epsilon_{yy}}{\epsilon_t}\right)\frac{\partial \tilde{E}_{y_1}^{\mathrm{TM}_y}}{\partial y}\right]_{y=H} = +\zeta\tilde{E}_x - \beta\tilde{E}_z \tag{172}$$

and

$$F_2(\zeta) = -\omega\mu_0\left(\tilde{H}_{y_2}^{\mathrm{TE}_y} - \tilde{H}_{y_1}^{\mathrm{TE}_y}\right)_{y=H} = -\beta\tilde{E}_x - \zeta\tilde{E}_z. \tag{173}$$

A modified Wiener–Hopf method has been applied to solve this system of equations for the dispersion properties of a single microstrip conductor on sapphire [51]. The equation

$$F_1^+(\mp j\beta) \mp jF_2^+(\mp j\beta) = 0 \tag{174}$$

where

$$F_1(\zeta) = F_1^+(\zeta) + e^{-j\zeta w}F_1^+(-\zeta) \tag{175}$$

and

$$F_2(\zeta) = F_2^+(\zeta) - e^{-j\zeta w}F_1^+(-\zeta) \tag{176}$$

leads to the dispersion equation, which is obtained from

$$\begin{vmatrix} \dfrac{T_1}{\chi_1^+(-j\beta)} & \dfrac{jT_2}{\chi_2^+(-j\beta)} \\ \dfrac{T_3}{\chi_1^+(j\beta)} & \dfrac{jT_4}{\chi_2^+(j\beta)} \end{vmatrix} = 0 \tag{177}$$

where

$$T_1 = 1 + \sum_{n=0}^{\infty}\frac{s_n}{j\beta + \zeta_{n1}}A_n \tag{178}$$

$$T_2 = 1 + \sum_{n=1}^{\infty}\frac{t_n}{j\beta + \zeta_{n2}}B_n \tag{179}$$

$$T_3 = 1 - \sum_{n=0}^{\infty}\frac{s_n}{j\beta - \zeta_{n1}}A_n \tag{180}$$

and

$$T_4 = 1 - \sum_{n=1}^{\infty}\frac{t_n}{j\beta - \zeta_{n2}}B_n. \tag{181}$$

The F_t^+ are analytic on the upper half-plane $\mathrm{Im}\,\zeta > 0$, and (175) and (176) are valid for a symmetric current distribution on the microstrip. The solutions for F_t^+ are obtained as

$$F_1^+(\zeta) = \frac{P}{\chi_1^+}\left[1 - \sum_{n=0}^{\infty}\frac{s_n}{\zeta - \zeta_{n1}}A_n\right] \tag{182}$$

and

$$F_2^+(\zeta) = \frac{Q}{\chi_2^+}\left[1 - \sum_{n=1}^{\infty}\frac{t_n}{\zeta - \zeta_{n2}}B_n\right] \tag{183}$$

where P and Q are constants and χ_t^+ are defined as the plus functions of $\chi_t(\zeta)$ where

$$\chi_1(\zeta) = \frac{\coth(R_0 H\nu)}{R_0} + \frac{\sqrt{\epsilon_t\epsilon_{yy}}}{R_y}\coth(R_y H_{\mathrm{eq}}) \tag{184}$$

and

$$\chi_2(\zeta) = R_0\coth(R_0 H\nu) + R_t\coth(R_t H) \tag{185}$$

and ζ_n are the poles of χ_1 and χ_2 in the lower half-plane. In addition, A_n and B_n are the solutions to the system of equations

$$A_n = 1 + \sum_{m=0}^{\infty}\frac{s_m}{\zeta_{n1} + \zeta_{m1}}A_m, \qquad n = 0,1,2,\cdots \tag{186}$$

and

$$B_n = 1 + \sum_{m=1}^{\infty}\frac{t_m}{\zeta_{n2} + \zeta_{m2}}B_m, \qquad n = 1,2,\cdots \tag{187}$$

with

$$s_n = \frac{\mathrm{Res}\left[\chi_1^+(\zeta_{n1})\right]}{\chi_1^+(-\zeta_{n1})}e^{-j\zeta_n w} \tag{188}$$

and

$$t_n = -\frac{\mathrm{Res}\left[\chi_2^+(\zeta_{n2})\right]}{\chi_2^+(-\zeta_{n2})}e^{-j\zeta_n w}. \tag{189}$$

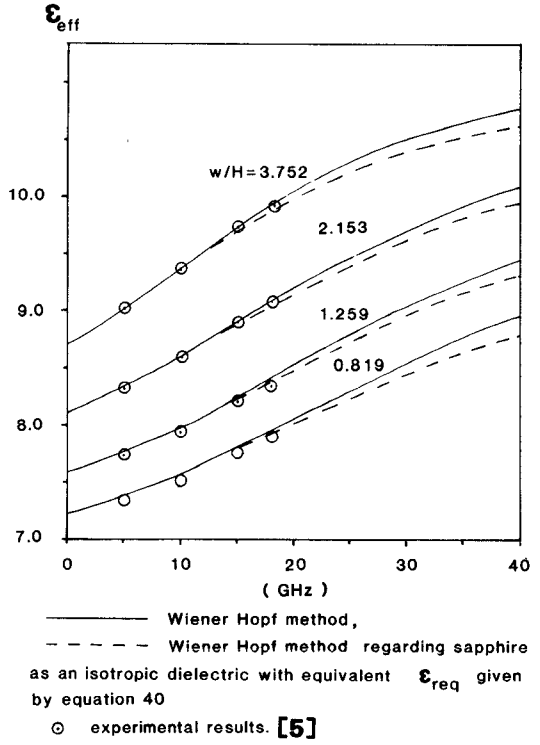

Fig. 22. Dispersion characteristics of microstrip with cover.

The characteristic impedance and the effective dielectric constant have been computed by this method. An expression for Z_0, based on the definition of wave impedance as the ratio of the quasi-static voltage at the center of the strip to the total longitudinal current, has been derived as

$$Z_0 = -\frac{j}{2\zeta_{01}} \frac{\beta F_1^+(-\zeta_{01})}{\omega\epsilon_0 F_1^+(0)\chi_1(0)} e^{-j\zeta_0 w/2} \tag{190}$$

where ζ_{01} is the lowest order pole of $\chi_1(\zeta)$ given by $\zeta_{01} = (k_0^2\epsilon_{yy} - \beta^2)^{1/2}$.

The effective dielectric constant is computed by using the definition $\epsilon_{eff} = (\beta/k_0)^2$ and it is shown in Fig. 22 as a function of frequency up to 40 GHz. Computations using the equivalent isotropic permittivities $\epsilon_{eq} = \sqrt{\epsilon_{xx}\epsilon_{yy}}$ and ϵ_{req} (as given by (40)) are also superimposed for comparison. When ϵ_{eq} is used, an error of 4–10 percent or greater occurs for $f > 5$ GHz, while the linewidth-corrected empirical expression for ϵ_{req} yields excellent agreement up to about 25 GHz, while at 40 GHz it introduces an error of about 2 percent [51].

b) Equivalent network method: An approach which is straightforward and more general in that it can be readily modified to yield solutions to a variety of integrated-circuit structures on anisotropic substrates with or without cover is the equivalent network technique [52]–[54]. The structure of Fig. 1(h) is considered for which the electric- and magnetic-field components transverse to the y-direction are expressed in the case of microstrip lines as [54]

$$\left.\begin{matrix} \boldsymbol{E}_t^{(i)} \\ \boldsymbol{H}_t^{(i)} \end{matrix}\right\} = \sum_{l=1}^{2} \int_{-\infty}^{\infty} \left\{ \begin{matrix} V_l^{(i)}(\zeta, y)\, \boldsymbol{f}_l(\zeta, x) \\ I_l^{(i)}(\zeta, y)\, \hat{y}x\boldsymbol{f}_l(\zeta, x) \end{matrix} \right\} e^{-j\beta z}\, d\zeta \tag{191}$$

where $i = 1,2,3$ refers to the ith region of the multiple-layered anisotropic structure. The index $l = 1$ corresponds to LSM and $l = 2$ to LSE modes. Furthermore

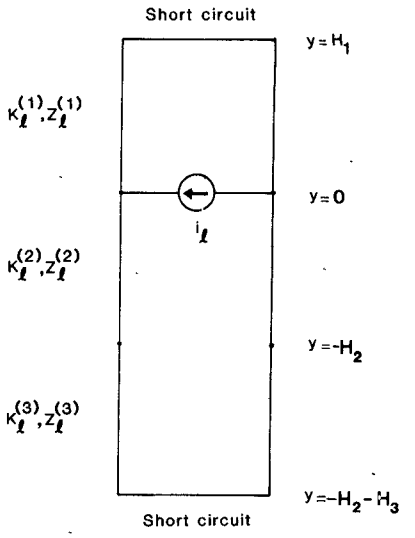

Fig. 23. Equivalent transmission-line circuits for transverse section of coupled strips.

$$\boldsymbol{f}_1(\zeta, x) = \frac{j}{\sqrt{2\pi}} \boldsymbol{K}_0 e^{-j\zeta x} \quad \boldsymbol{f}_2(\zeta, x) = -\hat{y} \times \boldsymbol{f}_1(\zeta, x) \tag{192}$$

and $\boldsymbol{K}_0 = \boldsymbol{K}/|\boldsymbol{K}|$ with $\boldsymbol{K} = \zeta\hat{x} + \beta\hat{z}$.

Substitution of $\boldsymbol{E}_t^{(i)}$ and $\boldsymbol{H}_t^{(i)}$ into Maxwell's equations yields the equivalent transmission-line relations

$$\frac{dV_l^{(i)}}{dy} = -j\kappa_l^{(i)} z_l^{(i)} I_l^{(i)} \tag{193}$$

and

$$\frac{dI_l^{(i)}}{dy} = -j\kappa_l^{(i)} y_l^{(i)} V_l^{(i)} \tag{194}$$

where

$$\kappa_1^{(i)} = \left[\epsilon_{i\perp} k_0^2 - \frac{\epsilon_{i\perp}}{\epsilon_{i_\parallel}} K^2\right]^{1/2} \quad \kappa_2^{(i)} = \left[\epsilon_{i\perp} k_0^2 - K^2\right]^{1/2}$$

$$z_1^{(i)} = \frac{\kappa_1^{(i)}}{\omega\epsilon_0\epsilon_{i\perp}} \quad z_2^{(i)} = \frac{\omega\mu_0}{\kappa_2^{(i)}} \text{ and } y_l^{(i)} = \frac{1}{z_l^{(i)}}.$$

In this development, $\kappa_1^{(i)}$ and $\kappa_2^{(i)}$ are the propagation constants in the $\hat{y}$-direction for TM_y and TE_y waves, while $z_{1,2}^{(i)}$ are the corresponding characteristic wave impedances for these waves (see Fig. 23 for equivalent transmission-line circuit). The (source) current density on the microstrip conductor at $y = 0$ is given by

$$\boldsymbol{j}_s(x, y, z) = \boldsymbol{j}_s(x)\delta(y)e^{-j\beta z} \tag{195}$$

where $\boldsymbol{j}_s(x)$ may be written as

$$\boldsymbol{j}_s(x) = \frac{1}{2\pi} \int_{-\infty}^{\infty} i(\zeta) e^{-j\zeta x}\, d\zeta. \tag{196}$$

It is also possible to define $i(\zeta)e^{-j\zeta x} = -2\pi[i_1(\zeta)\boldsymbol{f}_1(\zeta, x) + i_2(\zeta)\boldsymbol{f}_2(\zeta, x)]$ so that $\boldsymbol{j}_s(x)$ can be formulated as

$$\boldsymbol{j}_s(x) = -\int_{-\infty}^{\infty} [i_1(\zeta)\boldsymbol{f}_1(\zeta, x) + i_2(\zeta)\boldsymbol{f}_2(\zeta, x)]\, d\zeta. \tag{197}$$

Vector multiplication of (197) with $\boldsymbol{f}_l^*(\zeta, x)$ and integration over the spectrum yields the current density transform

$$i_l(\zeta) = -\int_{-\infty}^{\infty} \boldsymbol{f}_l^*(\zeta, x') \cdot \boldsymbol{j}_s(x')\, dx'. \tag{198}$$

Proceeding with the derivation of the dispersion equation for the propagation constant β, the boundary conditions at the layer interfaces and the grounded conductors may be expressed in terms of voltages and currents, i.e.,

$$V_l^{(1)}(\zeta, H_1) = 0 \tag{199}$$

$$V_l^{(2)}(\zeta, -H_2) = V_l^{(2)}(\zeta, -H_2) \tag{200}$$

$$V_l^{(1)}(\zeta, 0) = V_l^{(2)}(\zeta, 0) \tag{201}$$

$$V_l^{(3)}(\zeta, -H_2 - H_3) = 0 \tag{202}$$

$$I_l^{(1)}(y = 0^+) - I_l^{(2)}(y = 0^-) = i_l \tag{203}$$

and

$$I_l^{(2)}(y = -H_2) = I_l^{(3)}(y = -H_2). \tag{204}$$

Decoupling of (193) and (194) results in the solutions

$$V_l^{(i)}(\zeta, y) = Z_l^{(i)}(\zeta, y) i_l(\zeta) \tag{205}$$

and

$$I_l^{(i)}(\zeta, y) = T_l^{(i)}(\zeta, y) i_l(\zeta) \tag{206}$$

where

$$Z_l^{(1)}(\zeta, y) = -\frac{j \sin\left[\kappa_l^{(1)}(y - H_1)\right]}{D_0} \tag{207}$$

$$Z_l^{(2)}(\zeta, y) = \frac{j \sin\left(\kappa_l^{(1)} H_1\right)}{D_0}\left[D_1 \sin\left(\kappa_l^{(2)} y\right) + \cos\left(\kappa_l^{(2)}(y)\right)\right] \tag{208}$$

$$Z_l^{(3)}(\zeta, y) = -\frac{j \sin\left[\kappa_l^{(2)}(y + H_2 + H_3)\right]}{D_0} \frac{\sin\left(\kappa_l^{(1)} H_1\right)}{\sin\left(\kappa_l^{(3)} H_3\right)} \times \left[D_1 \sin\left(\kappa_l^{(2)} H_2\right) - \cos\left(\kappa_l^{(2)} H_2\right)\right] \tag{209}$$

$$T_l^{(1)}(\zeta, y) = \frac{y_l^{(1)} \cos\left[\kappa_l^{(1)}(y - H_1)\right]}{D_0} \tag{210}$$

$$T_l^{(2)}(\zeta, y) = \frac{y_l^{(2)} \sin\left(\kappa_l^{(1)} H_1\right)}{D_0}\left[\sin\left(\kappa_l^{(2)} y\right) - D_1 \cos\left(\kappa_l^{(2)} y\right)\right] \tag{211}$$

$$T_l^{(3)}(\zeta, y) = -\frac{y_l^{(3)} \sin\left(\kappa_l^{(1)} H_1\right)}{D_0} \frac{\cos\left[\kappa_l^{(3)}(y + H_2 + H_3)\right]}{\sin\left(\kappa_l^{(3)} H_3\right)} \cdot \left[\cos\left(\kappa_l^{(2)} H_2\right) - D_1 \sin\left(\kappa_l^{(2)} H_2\right)\right] \tag{212}$$

with

$$D_0 = y_l^{(1)} \cos\left(\kappa_l^{(1)} H_1\right) + y_l^{(2)} \sin\left(\kappa_l^{(1)} H_1\right) D_1$$

and

$$D_1 = \frac{\dfrac{\cos\left(\kappa_l^{(2)} H_2\right)}{\sin\left(\kappa_l^{(3)} H_3\right)} - \dfrac{y_l^{(2)} \sin\left(\kappa_l^{(2)} H_2\right)}{y_l^{(3)} \cos\left(\kappa_l^{(3)} H_3\right)}}{\dfrac{\sin\left(\kappa_l^{(2)} H_2\right)}{\sin\left(\kappa_l^{(3)} H_3\right)} + \dfrac{y_l^{(2)} \cos\left(\kappa_l^{(2)} H_2\right)}{y_l^{(3)} \cos\left(\kappa_l^{(3)} H_3\right)}}.$$

With the aid of these relations and (198), $\boldsymbol{E}_t^{(i)}$ can be derived in each region. The electric-field components in region 1 can be written as

$$E_x^{(1)} = -\frac{e^{-j\beta z}}{2\pi} \int_{-\infty}^{\infty} \frac{d\zeta}{\zeta^2 + \beta^2} \cdot \int_{-\infty}^{\infty} \left[\left[\zeta^2 Z_1^{(1)}(\zeta, y) + \beta^2 Z_2^{(1)}(\zeta, y)\right] j_x(x') + \zeta\beta\left[Z_1^{(1)}(\zeta, y) - Z_2^{(1)}(\zeta, y)\right] j_z(x')\right] \cdot e^{-j\zeta(x - x')}\, dx' \tag{213}$$

and

$$E_z^{(1)} = -\frac{e^{-j\beta z}}{2\pi} \int_{-\infty}^{\infty} \frac{d\zeta}{\zeta^2 + \beta^2} \cdot \int_{-\infty}^{\infty} \left[\zeta\beta\left[Z_1^{(1)}(\zeta, y) - Z_2^{(1)}(\zeta, y)\right] \times j_x(x') + \left[\beta^2 Z_1^{(1)}(\zeta, y) + \zeta^2 Z_2^{(1)}(\zeta, y)\right] j_z(x')\right] \cdot e^{-j\zeta(x - x')}\, dx'. \tag{214}$$

In order to derive the dispersion relations for the coupled microstrip lines shown in Fig. 1(h), a solution is obtained in terms of even- and odd-mode analysis.

i) Even modes (magnetic wall at $x = 0$): For this particular case, even-mode symmetry implies $j_{xe}(x') = -j_{xe}(-x')$ and $j_{ze}(x') = j_{ze}(-x')$, and therefore (213) and (214) can be rewritten as

$$E_{xe}^{(1)} = -\frac{2e^{-j\beta z}}{\pi} \int_0^{\infty} \frac{d\zeta}{\zeta^2 + \beta^2} \cdot \int_{s/2}^{s/2 + w} \left[\left[\zeta^2 Z_1^{(1)}(\zeta, y) + \beta^2 Z_1^{(2)}(\zeta, y)\right] j_{xe}(x') \cdot \sin(\zeta x) \sin(\zeta x') - j\left[\zeta\beta\left(Z_1^{(1)}(\zeta, y) - Z_2^{(1)}(\zeta, y)\right)\right] \cdot j_{ze}(x') \sin(\zeta x) \cos(\zeta x')\, dx' \tag{215}$$

and

$$E_{ze}^{(1)} = -\frac{2e^{-j\beta z}}{\pi} \int_0^{\infty} \frac{d\zeta}{\zeta^2 + \beta^2} \cdot \int_{s/2}^{s/2 + w} \left[j(\zeta\beta)\left(Z_1^{(1)}(\zeta, y) - Z_2^{(1)}(\zeta, y)\right)\right] \cdot j_{xe}(x') \cos(\zeta x) \sin(\zeta x') + \left[\beta^2 Z_1^{(1)}(\zeta, y) + \zeta^2 Z_2^{(1)}(\zeta, y)\right] \cdot j_{ze}(x') \cos(\zeta x) \cos(\zeta x')\, dx'. \tag{216}$$

On the strip, i.e., for $s/2 < x < s/2 + w$, $E_{xe}^{(1)} = E_{ze}^{(1)} = 0$, and the Galerkin method is invoked to obtain solutions of (215) and (216) for $j_{xe}(x)$ and $j_{ze}(x)$. These current densities are expanded into the forms [54]

$$j_{ze}(x') = \sum_{n=0}^{N} a_{nze} \frac{T_{2n}\left(\dfrac{2(x' - s)}{w}\right)^2}{\sqrt{1 - \left(\dfrac{2(x' - s)}{w}\right)}} \tag{217}$$

and

$$j_{xe}(x') = -j \sum_{n=0}^{N} a_{nxe} U_{2n}\left(\frac{2(x - s)}{w}\right) \tag{218}$$

where $T_n(x)$ and $U_n(x)$ represent the Chebyshev polynomials of the first and second kind, respectively. The particular choice of this representation for $j_{ze}(x')$ and $j_{xe}(x')$ is dictated by the edge conditions for the current density components at $x = s/2$ and $x = s/2 + w$. Consideration of the fact that $E_{xe}^{(1)} = E_{ze}^{(1)} = 0$ on the microstrip and substitution of (217) and (218) into (215) and (216) yields the following system of equations to be solved for the propagation constant β, namely:

$$\sum_{n=0}^{N} \alpha_{mne} a_{nze} + \sum_{n+1}^{N} \beta_{mne} a_{nxe} = 0, \qquad m = 0,1,2,3,\cdots,N \quad (219)$$

and

$$\sum_{n=0}^{N} \gamma_{mne} a_{nze} + \sum_{n=1}^{N} \delta_{mne} a_{nxe} = 0, \qquad m = 1,2,3,\cdots,N \quad (220)$$

where

$$\alpha_{mne} = (-1)^{m+n}\left(\frac{w}{2}\right)^2\left(\frac{2}{\pi}\right) \cdot \int_0^{\infty} \frac{d\zeta}{\zeta^2+\beta^2}\left[\beta^2 Z_1^{(1)}(\zeta,0) + \zeta^2 Z_2^{(1)}(\zeta,0)\right] \cdot J_{2n}\left(\frac{\zeta w}{2}\right) \cdot J_{2m}\left(\frac{\zeta w}{2}\right) \quad (221)$$

$$\beta_{mne} = (-1)^{m+n} nw(2/\pi) \cdot \int_0^{\infty} \frac{d\zeta}{\zeta^2+\beta^2}\left[\beta\left(Z_1^{(1)}(\zeta,0) - Z_2^{(1)}(\zeta,0)\right)\right] \cdot J_{2n}\left(\frac{\zeta w}{2}\right) J_{2m}\left(\frac{\zeta w}{2}\right) \quad (222)$$

and

$$\gamma_{mne} = \frac{m}{n}\beta_{mne} \quad (223)$$

$$\delta_{mne} = (-1)^{m+n} 4mn(2/\pi) \cdot \int_0^{\infty} \frac{d\zeta}{\zeta^2+\beta^2}\left[Z_1^{(1)}(\zeta,0) + \frac{\beta^2}{\zeta^2} Z_2^{(1)}(\zeta,0)\right] \cdot J_{2n}\left(\frac{\zeta w}{2}\right) J_{2m}\left(\frac{\zeta w}{2}\right) d\zeta. \quad (224)$$

Setting the determinant of the system of equations (219) and (220) equal to zero yields the dispersion equation for the even-mode propagation constant.

ii) Odd modes (electric wall at $x = 0$): For odd modes, $j_{xo}(x') = j_{xo}(-x')$, while $j_{zo}(x') = -j_{zo}(-x')$ and the electric-field components in region 1 are now given by

$$E_{xo}^{(1)} = -\frac{2e^{-j\beta z}}{\pi}\int_0^{\infty}\frac{d\zeta}{\zeta^2+\beta^2} \cdot \int_{s/2}^{s/2+w}\left[\left[\zeta^2 Z_1^{(1)}(\zeta,y) + \beta^2 Z_2^{(1)}(\zeta,y)\right] j_x(x')\cos(\zeta x)\cos(\zeta x') + j\zeta\beta\left[Z_1^{(1)}(\zeta,y) - Z_2^{(1)}(\zeta,y)\right] \cdot j_z(x')\cos(\zeta x)\sin(\zeta x')\right] dx' \quad (225)$$

and

$$E_{zo}^{(1)} = -\frac{2e^{-j\beta z}}{\pi}\int_0^{\infty}\frac{d\zeta}{\zeta^2+\beta^2} \cdot \int_{s/2}^{s/2+w}\left[\left[\beta^2 Z_1^{(1)}(\zeta,y) + \zeta^2 Z_2^{(1)}(\zeta,y)\right] j_z(x')\sin(\zeta x)\sin(\zeta x') - j\zeta\beta\left[Z_1^{(1)}(\zeta,y) - Z_2^{(1)}(\zeta,y)\right] \cdot j_x(x')\sin(\zeta x)\cos(\zeta x')\right] dx'. \quad (226)$$

In applying the Galerkin procedure for odd modes, the following expansions have been adopted for the current density components $j_{xo}(x)$ and $j_{zo}(x)$, namely [54]:

$$j_{zo}(x) = \sum_{n=1}^{N} a_{nzo} \frac{T_{2n-1}\left(\frac{2(x'-s)}{w}\right)}{\sqrt{1-\left(\frac{2(x-s)}{w}\right)^2}}$$

and

$$-jj_{xo}(x) = \sum_{n=1}^{N} a_{nxo} U_{2n-1}\left(\frac{2(x'-s)}{w}\right).$$

Adaptation of the above current distributions and the fact that $E_{xo}^{(1)} = E_{zo}^{(1)} = 0$ on the strip yields, in this case, the system of equations

$$\sum_{n=1}^{N} \alpha_{mno} a_{nzo} + \sum_{n=1}^{N} \beta_{mno} a_{nxo} = 0, \qquad m = 1,2,3,\cdots,N \quad (227)$$

and

$$\sum_{n=1}^{N} \gamma_{mno} a_{nzo} + \sum_{n=1}^{N} \delta_{mno} a_{nxo} = 0, \qquad m = 1,2,3,\cdots,N \quad (228)$$

whose solution yields the dispersive properties of the propagation constant for the odd mode. For this particular case

$$\alpha_{mno} = (-1)^{m+n}\left(\frac{w}{2}\right)^2\frac{2}{\pi}\int_0^{\infty}\frac{d\zeta}{\zeta^2+\beta^2} \cdot \left[\beta^2 Z_1^{(1)}(\zeta,0) + \zeta^2 Z_2^{(1)}(\zeta,0)\right] \cdot J_{2n-1}\left(\frac{\zeta w}{2}\right) J_{2m-1}\left(\frac{\zeta w}{2}\right) \quad (229)$$

$$\beta_{mno} = (-1)^{m+n}\left(\frac{w}{2}\right)(2n-1)\left(\frac{2}{\pi}\right)\int_0^{\infty}\frac{d\zeta}{\zeta^2+\beta^2} \cdot \left[\beta\left(Z_0^{(1)}(\zeta,0) - Z_2^{(1)}(\zeta,0)\right)\right] \cdot J_{2n-1}\left(\frac{\zeta w}{2}\right) J_{2m-1}\left(\frac{\zeta w}{2}\right) \quad (230)$$

$$\gamma_{mno} = \frac{(2m-1)}{(2n-1)}\beta_{mno}$$

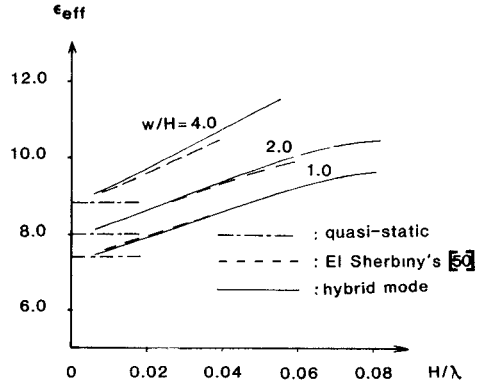

Fig. 24. Dispersion characteristics of single microstrip on sapphire.

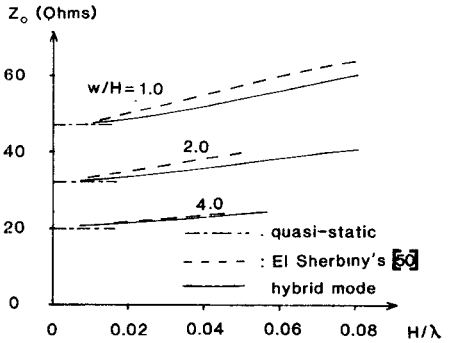

Fig. 25. Characteristic impedance of single microstrip on sapphire.

and

$$\delta_{mno} = (-1)^{m+n}(2n-1)(2m-1)\left(\frac{2}{\pi}\right)\int_0^\infty \frac{d\zeta}{\zeta^2+\beta^2} \cdot\left[Z_1^{(1)}(\zeta,0)+\frac{\beta^2}{\zeta^2}Z_2^{(1)}(\zeta,0)\right] \cdot J_{2n-1}\left(\frac{\zeta w}{2}\right)J_{2m-1}\left(\frac{\zeta w}{2}\right). \quad (231)$$

Numerical computations based on this analysis have been performed for various microstrip geometries. The results show that even for $N=2$, sufficient convergence accuracy is obtained [54]. Comparison of this technique with the Wiener–Hopf method indicates excellent agreement for the single microstrip with cover case in the computations for ϵ_{eff} when $w/H \leqslant 4.0$. The discrepancy between the two techniques becomes larger for increasing w/H, as Fig. 24 indicates. Furthermore, this disagreement, as Fig. 25 shows, is even more prominent when the dispersive behavior of Z_0 is compared between the two methods. This discrepancy is also due to the fact that the characteristic impedance in this case is defined in terms of the ratio P_{ave}/I^2, where P_{ave} is the average power flowing in the $\hat{z}$-direction along the microstrip as computed by the Poynting vector, and I is the total current on the microstrip. This definition of Z_0 accounts for dispersion more accurately than the definition used in [52], which is based on the ratio of the quasi-static voltage at the center of the strip to the total longitudinal strip current.

2) Discrete Fourier Spectrum — Structures with a Rectangular Shield: When a waveguiding structure is enclosed entirely within a rectangular shield, the discrete Fourier spectrum may be used to determine the dispersion properties of the distributed circuit [55], [56]. For coupled lines, the method requires the following Fourier transform definitions.

Even Modes (Magnetic Wall at $x=0$):

$$\tilde{E}_y^{TM_y} = \int_0^a E_y^{TM_y}\cos(k_n x)\,dx \quad (232)$$

$$\tilde{H}_y^{TE_y} = \int_0^a H_y^{TE_y}\sin(k_n x)\,dx \quad (233)$$

where $k_n = (2n-1)/2a\pi$.

Odd Modes (Electric Wall at $x=0$):

$$\tilde{E}_y^{TM_y} = \int_0^a E_y^{TM_y}\sin(k_n x)\,dx \quad (234)$$

$$\tilde{H}_y^{TE_y} = \int_0^a H_y^{TE_y}\cos(k_n x)\,dx \quad (235)$$

where $k_n = n\pi/a$.

These representations yield for the LSE and LSM modes the following equations.

LSE Modes:

$$\tilde{E}_x^{TE_y} = \frac{\omega\mu_0\beta}{\beta^2+k_n^2}\tilde{H}_y^{TE_y} \quad (236)$$

$$\tilde{E}_z^{TE_y} = \pm\frac{j\omega\mu_0 k_n}{\beta^2+k_n^2}\tilde{H}_y^{TE_y} \quad (237)$$

$$\tilde{H}_x^{TE_y} = \mp\frac{k_n}{\beta^2+k_n^2}\frac{\partial\tilde{H}_y^{TE_y}}{\partial y} \quad (238)$$

and

$$\tilde{H}_z^{TE_y} = -\frac{j\beta}{\beta^2+k_n^2}\frac{\partial\tilde{H}_y^{TE_y}}{\partial y} \quad (239)$$

where $H_y^{TE_y}$ satisfies the wave equation with $\zeta^2 = k_n^2$.

LSM Modes:

$$\tilde{E}_x^{TM_y} = \pm\frac{k_n\left(\frac{\epsilon_{yy}}{\epsilon_t}\right)}{\beta^2+k_n^2}\frac{\partial\tilde{E}_y^{TM_y}}{\partial y} \quad (240)$$

$$\tilde{E}_z^{TM_y} = -\frac{j\beta\left(\frac{\epsilon_{yy}}{\epsilon_t}\right)}{\beta^2+k_n^2}\frac{\partial\tilde{E}_y^{TM_y}}{\partial y} \quad (241)$$

$$\tilde{H}_x^{TM_y} = -\frac{\omega\epsilon_0\epsilon_{yy}\beta}{\beta^2+k_n^2}\tilde{E}_y^{TM_y} \quad (242)$$

$$\tilde{H}_z^{TM_y} = \pm\frac{j\omega\epsilon_0\epsilon_{yy}k_n}{\beta^2+k_n^2}\tilde{E}_y^{TM_y} \quad (243)$$

and $E_y^{TM_y}$ satisfies the wave equation with $\zeta^2 = k_n^2$. The lower (upper) signs refer to even (odd) modes, respectively. The current distribution Fourier components $\tilde{J}_x$ and $\tilde{J}_z$ can be obtained by inverting the system of equations [56]

$$\begin{bmatrix} j\tilde{E}_z \\ \tilde{E}_x \end{bmatrix} = \begin{bmatrix} \tilde{G}_{11} & \tilde{G}_{12} \\ \tilde{G}_{21} & \tilde{G}_{22} \end{bmatrix}\begin{bmatrix} j\tilde{J}_x \\ -\tilde{J}_z \end{bmatrix} \quad (244)$$

which is valid on the plane of the strips. The matrix components G_{lm} are elements of the Green's dyadic function for the multiple-layered geometry shown in Fig. 1(l). The boundary-value problem solution yields for G_{lm} the following result:

$$\tilde{G}_{11}=\tilde{G}_{22}=\frac{\pm k_0 k_n \beta}{\gamma_n^2 \omega \epsilon_0}\left[F_1(k_n,\beta)+F_2(k_n,\beta)\right] \tag{245}$$

$$\tilde{G}_{12}=\frac{k_0}{\gamma_n^2 \omega \epsilon_0}\left[k_n^2 F_1(k_n,\beta)-\beta^2 F_2(k_n,\beta)\right] \tag{246}$$

$$\tilde{G}_{21}=\frac{k_0}{\gamma_n^2 \omega \epsilon_0}\left[\beta^2 F_1(k_n,\beta)-k_n^2 F_2(k_n,\beta)\right] \tag{247}$$

where

$$F_1(k_n,\beta)=\left[1/f_{t1}+\left(\alpha_t^{(2)^2} f_{t2} f_{t3}+1\right)/\left(f_{t2}+f_{t3}\right)\right]^{-1} \tag{248}$$

$$F_2(k_n,\beta)=\left[1/g_{y1}+\left(g_{y2}g_{y3}+\alpha_y^{(2)^2}\right)/\left\{\alpha_y^{(2)^2}\left(g_{y2}+g_{y3}\right)\right\}\right]^{-1} \tag{249}$$

$$\gamma_n^2=\beta^2+k_n^2 \tag{250}$$

$$\alpha_y^{(i)}=\sqrt{\left\{\left(\gamma_n/k_0\right)^2-\epsilon_y^{(i)}\right\}/\left(\epsilon_y^{(i)}\epsilon_t^{(i)}\right)} \tag{251}$$

$$\alpha_t^{(i)}=\sqrt{\left(\gamma_n/k_0\right)^2-\epsilon_t^{(i)}} \tag{252}$$

$$f_{ti}=\tanh\left(k_0\alpha_t^{(i)}h_i\right)/\alpha_t^{(i)} \tag{253}$$

and

$$g_{yi}=\alpha_y^{(i)}\tanh\left(\epsilon_t^{(i)}k_0\alpha_y^{(i)}h_i\right). \tag{254}$$

The subscript/superscript i refers to the ith anisotropic layer in the structure.

For the slotline or coplanar waveguide problem, duality may be invoked to show that the conductor currents are related to the slot-field components through the relation [56]

$$\begin{bmatrix} j\tilde{J}_x \\ -\tilde{J}_z \end{bmatrix}=\begin{bmatrix} \tilde{Q}_{11} & \tilde{Q}_{12} \\ \tilde{Q}_{21} & \tilde{Q}_{22} \end{bmatrix}\begin{bmatrix} j\tilde{E}_z \\ \tilde{E}_x \end{bmatrix} \tag{255}$$

where

$$\tilde{Q}_{11}=\tilde{G}_{22}/\Delta \quad \tilde{Q}_{12}=-\tilde{G}_{12}/\Delta \quad \tilde{Q}_{21}=-\tilde{G}_{21}/\Delta \tag{256}$$

and

$$\Delta=\tilde{G}_{11}\tilde{G}_{22}-\tilde{G}_{12}\tilde{G}_{21}. \tag{257}$$

The microstrip current density or slot-field distribution may be expanded in terms of a set of known basis functions $\{f_k(x)\}$ and $\{g_k(x)\}$ in the form

$$\left.\begin{matrix} -J_z(x) \\ E_x(x) \end{matrix}\right\}=\sum_{k=1}^{N} c_k f_k(x) \tag{258}$$

and

$$\left.\begin{matrix} jJ_x(x) \\ jE_z(x) \end{matrix}\right\}=\sum_{k=1}^{M} d_k g_k(x) \tag{259}$$

where $f_k(x)$ and $g_k(x)$ are defined only on the microstrip line or on the slot. The basis functions are chosen so that the edge effect is properly included, i.e., $f_k(x)=[(x-\frac{1}{2}(s+w))/w/2]^{k-1}$ and $g_k(x)=\sin[k\pi(x-s/2)/w]$, [56]. The microstrip current density or slot-field distribution as represented by (258) and (259) are Fourier transformed and the result is substituted in (244) or (255). The Galerkin procedure is applied to yield a system of $(N+M)\times(N+M)$ eigenequations for the unknown constants c_k and d_k. On the microstrip or the slot, this is a homogeneous system of equations whose determinant is set equal to zero to yield the dispersive behavior of the propagation constant β. The elements of the determinantal equation are given by

$$\begin{pmatrix} X_{rp}^{(1,1)} \\ X_{rq}^{(1,2)} \\ X_{sp}^{(2,1)} \\ X_{sq}^{(2,2)} \end{pmatrix}=\sum_{l=1}^{\infty}\begin{pmatrix} \tilde{J}_{zr}(k_l)\tilde{G}_{11}(\beta,k_l)\tilde{J}_{xp}(k_l) \\ \tilde{J}_{zr}(k_l)\tilde{G}_{12}(\beta,k_l)\tilde{J}_{zq}(k_l) \\ \tilde{J}_{xs}(k_l)\tilde{G}_{21}(\beta,k_l)\tilde{J}_{xp}(k_l) \\ \tilde{J}_{xs}(k_l)\tilde{G}_{22}(\beta,k_l)\tilde{J}_{yq}(k_l) \end{pmatrix} \tag{260}$$

where $p=s=1$ to M and $r=q=1$ to N.

This technique has been tested against already discussed quasi-static as well as dynamic solutions. In the quasi-static case, the results of the microstrip couplers with a superstrate layer shown in Table VII have been checked. For each case, a difference of less than 0.03 percent was found for $N=2$, $M=10$, $a=20$, $k_0=10^{-4}$, and $l=1000$. The dispersion curves for $\epsilon_{\text{eff}}^{\{e,o\}}$ as determined by the TLM method have also been verified. In using the discrete Fourier technique, a convergence accuracy better than 0.5 percent has been enforced. This convergence requirement is satisfied when $N=M=4$ and $l=300$ for the results shown in Fig. 26, and it has been determined that for the mesh size chosen the TLM computations are consistently lower by 3 percent for $\epsilon_{\text{eff}}^{(o)}$ and 1.5 percent for $\epsilon_{\text{eff}}^{(e)}$. A particular case of interest is shown in Fig. 27 where as observed equalization of even- and odd-mode phase velocities is obtained at those normalized frequencies where $\epsilon_{\text{eff}}^{(e)}=\epsilon_{\text{eff}}^{(o)}$. In order to emphasize the versatility of this technique, the dispersive properties of coupled inverted microstrip lines are demonstrated in Fig. 28, while Fig. 29 shows the variation of ϵ_{eff} for a shielded slotline.

The dispersion curves of Fig. 28 highlight the frequency dependence of the error incurred when anisotropy is not included in the computation. The error becomes larger with increasing frequency and it is of the order of 17 percent when, e.g., normalized $k_0=0.70$. The results calculated by this method have been found to be in excellent agreement with those obtained by the equivalent network approach for microstrip with cover and for coupled slots without cover. In addition to the excellent accuracy, this approach provides a generalized algorithm which can resolve all the waveguiding structures shown in Fig. 1 [56]. For this reason, it is perhaps the most useful of the tools presented in this paper for the analysis of the dispersive properties of a variety of integrated-circuit waveguiding structures.

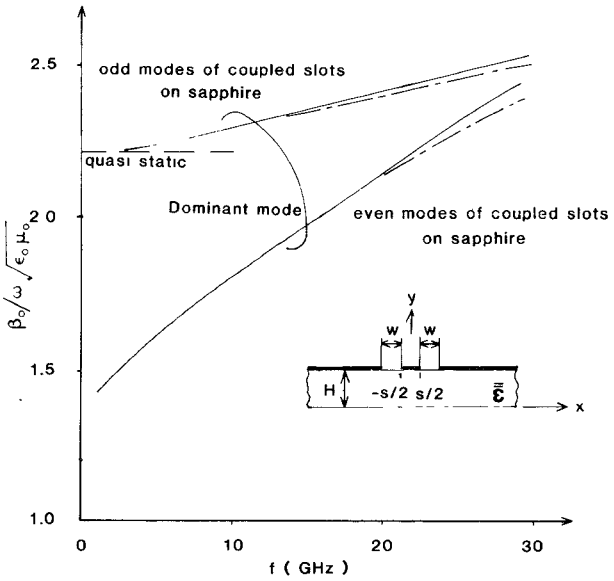

Fig. 26. Normalized propagation constant.

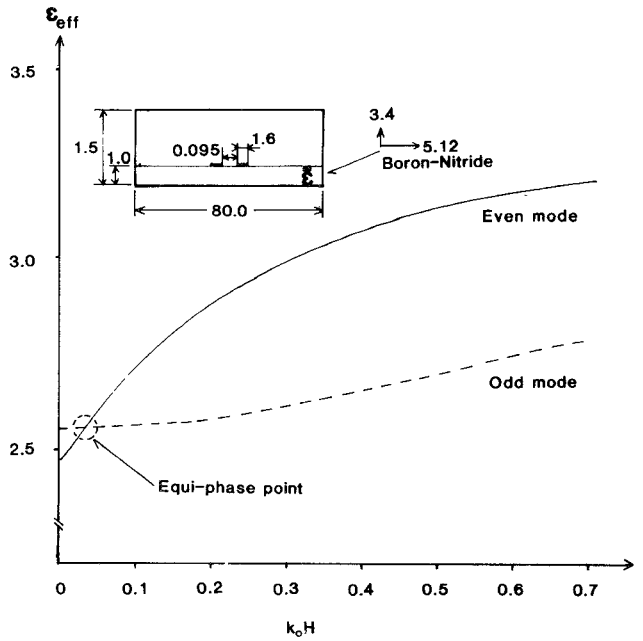

Fig. 27. Dispersive behavior of ϵ for coupled microstrip in a rectangular shield.

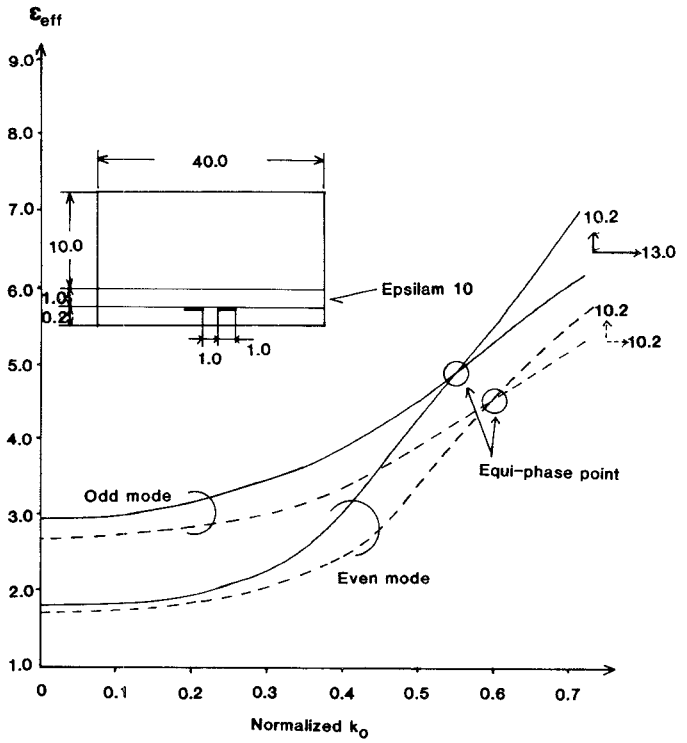

Fig. 28. Dispersion behavior of inverted coupled microstrip lines.

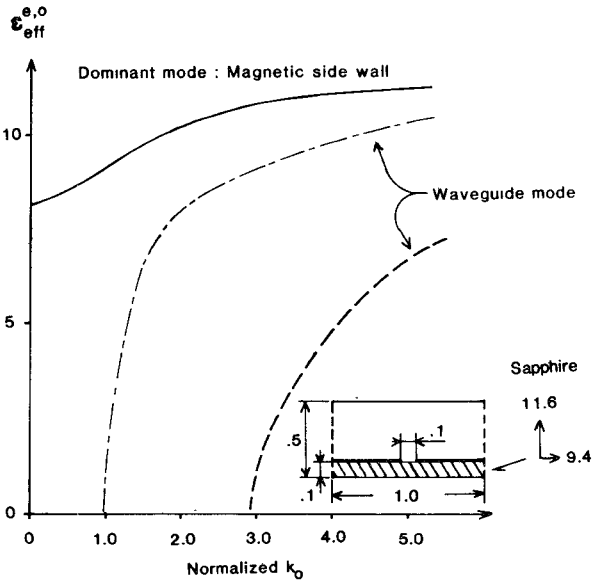

Fig. 29. Dispersion characteristics of single slot and waveguide modes.

C. The Method of Lines

This method solves directly the wave equation and associated boundary conditions for waveguiding structures in a rectangular shield. It is essentially a simplified version of the finite differences method, it is more accurate, and requires less computation time. The system of partial differential equations which describes the nature of the propagating modes is discretized in all directions, except the direction which is transverse to the electrical inhomogeneities of the structure under consideration. The procedure requires, e.g., that the $\hat{x}$-dimension of the circuit of Fig. 1(c) be divided into N subsections by defining $x_n = x_o + n\Delta x$ with $n = 1, 2, \cdots, N$ (see Fig. 30). This discretization forces the replacement of derivatives in the $\hat{x}$-direction by

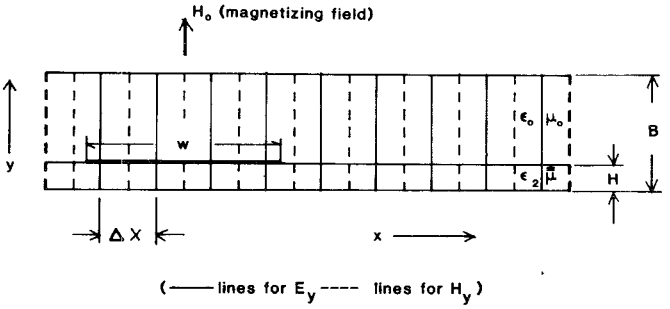

Fig. 30. Cross section of planar microwave structure on magnetized ferrite substrate.

finite differences, and it yields a system of N-coupled ordinary differential equations. Upon the introduction of the proper transformed potentials, this system is reduced to N-uncoupled ordinary second-order differential equations which can be solved easily. The steps leading to this latter system of differential equations may be chosen carefully so as to account correctly for the boundary conditions at the side walls of the enclosure, as well as for the edge condition at the waveguiding circuit edges [93]–[95].

This technique has been adopted to obtain the dispersive properties of a microstrip transmission line on a gyrotropic substrate [10]. For the case of a dc magnetizing field $\boldsymbol{H} = \hat{y}H_0$, the permeability tensor given by (5) is used with $\mu_{xx} = \mu_0\mu_1$, $\mu_{xz} = j\mu_0\mu_2$, $\mu_{yy} = \mu_0$, $\mu_{zx} = \mu_{xz}^*$, and $\mu_{zz} = \mu_0\mu_1 = \mu_{xx}$ where

$$\mu_1 = 1 + \frac{\gamma^2 M_s H_0}{(\gamma H_0)^2 - \omega^2} \tag{261}$$

and

$$\mu_2 = \frac{\omega\gamma M_s}{(\gamma H_0)^2 - \omega^2}. \tag{262}$$

In these equations, γ is the gyromagnetic ratio and M_s represents the saturation magnetization [8]. Maxwell's equations are solved in this gyrotropic medium in terms of the electric- and magnetic-field components in the direction of H_0, i.e., in terms of E_y and H_y [10]. A coupled system of second-order partial differential equations results for this case in the form

$$\frac{\partial^2 E_y}{\partial x^2} + \frac{\partial^2 E_y}{\partial y^2} - \beta^2 E_y + \mu_e k_e^2 E_y = k_e \eta \left(\frac{\mu_2}{\mu_1}\right) \frac{\partial H_y}{\partial y} \tag{263}$$

and

$$\frac{\partial^2 H_y}{\partial x^2} + \frac{1}{\mu_0}\frac{\partial^2 H_y}{\partial y^2} - \beta^2 H_y + k_e^2 H_y = -\frac{k_e}{\eta}\left(\frac{\mu_2}{\mu_1}\right)\frac{\partial E_y}{\partial y} \tag{264}$$

where

$$\eta = (\mu_0/\epsilon_2)^{1/2} \quad \mu_e = \mu_1 - \frac{\mu_2^2}{\mu_1} \quad \text{and} \quad k_e^2 = \omega^2 \epsilon_2 \mu_0.$$

A discretization procedure is adopted in the $\hat{x}$-direction [10] as suggested in [93]–[95] and [10] which reduces this pair of second-order coupled partial differential equations to a system of second-order ordinary differential equations in the form

$$\left(\frac{d^2}{dy^2} + \mu_e k_e^2 - \beta^2\right) - \frac{1}{(\Delta x)^2}[\lambda^2]\Bigg)\underline{E}_y = \eta k_e \frac{\mu_2}{\mu_1}\frac{\partial}{\partial y}\underline{H}_y \tag{265}$$

and

$$\left(\frac{1}{\mu_1}\frac{d^2}{dy^2} + k_e^2 - \beta^2\right) - \frac{1}{(\Delta x)^2}[\lambda^2]\Bigg)\underline{H}_y = -\frac{1}{\eta}k_e\left(\frac{\mu_2}{\mu_1}\right)\frac{\partial}{\partial y}\underline{E}_y \tag{266}$$

where $\underline{E}_y$ and $\underline{H}_y$ are column vectors with elements E_{yn}, H_{yn} $(n = 1, 2, 3, \cdots, M)$. In order to arrive at this system of coupled ordinary second-order differential equations, the following boundary conditions have been invoked.

On Electric Wall:

$$E_y = E_z = 0 \quad \text{and} \quad \frac{\partial H_y}{\partial x} = -j\frac{\mu_2}{\mu_1}\frac{\partial H_z}{\partial y}. \tag{267}$$

On Magnetic Wall:

$$H_y = H_z = 0 \quad \text{and} \quad \frac{\partial E_y}{\partial x} = -\eta\mu_2 k_e H_x. \tag{268}$$

In (265) and (266), $[\lambda]$ is a diagonal matrix and its elements represent the eigenvalues of the discretization matrix [10]. Equations (265) and (266) may be decoupled in the spectral domain to yield a system of fourth-order ordinary differential equations in the form

$$\left[\left(\frac{1}{\mu_1}\frac{d^2}{dy^2} + [\xi^h]\right)\left(\frac{d^2}{dy^2} + [\xi^e]\right) + k_e^2\frac{\mu_2^2}{\mu_1^2}\frac{d^2}{dy^2}\right]\underline{G}_y = 0 \tag{269}$$

where $\underline{G}_y$ represents either $\underline{E}_y$ or $\underline{H}_y$. In addition, $\xi_n^h =$

$$k_e^2 - \beta^2 - \frac{1}{(\Delta x)^2}\lambda_n^2 \quad \text{and} \quad \xi_n^e = \mu_e k_e^2 - \beta^2 - \frac{1}{(\Delta x)^2}\lambda_n^2.$$

This fourth-order differential equation may be solved easily in terms of hyperbolic sines and cosines to yield the solutions

$$E_{yn} = A_{1n}\cosh k_{y1n} y + A_{2n}\cosh k_{y2n} y \tag{270}$$

and

$$H_{yn} = B_{1n}\sinh k_{y1n} y + B_{2n}\sinh k_{y2n} y \tag{271}$$

with

$$k_{y1n,2n}^2 = -\mu_1\left(x_n \pm \sqrt{x_n^2 - 4\,\frac{\xi_n^e \xi_n^h}{\mu_1}}\right) \tag{272}$$

and

$$x_n = \xi_n^h + \frac{1}{\mu_1}\xi_n^e + k_e^2\frac{\mu_2^2}{\mu_1^2}. \tag{273}$$

The coefficients B_{1n} and B_{2n} are obtained in terms of A_{1n} and A_{2n} by substituting (270) and (271). A similar approach is followed in the air region, and subsequently the boundary conditions are applied at the interface to yield after some manipulations the dispersion equation in β/k_0. This procedure as adopted in [10] yields the dispersion diagrams shown in Fig. 31 for $H_0/M_s = 2.0$ and 8.1 Comparison with the results obtained by the mode-matching technique [9] indicates excellent agreement for $H_0/M_s =$ 8.1, but a serious discrepancy exists between the two methods for increasing frequency when $H_0/M_s = 2.0$. This disagreement has not been clarified as yet, but previous results on isotropic substrates have in general verified the accuracy of the method of lines. The discussion in this section simply indicates that this is a useful technique which can be extended to analyze the properties of integrated-circuit structures on anisotropic substrates.

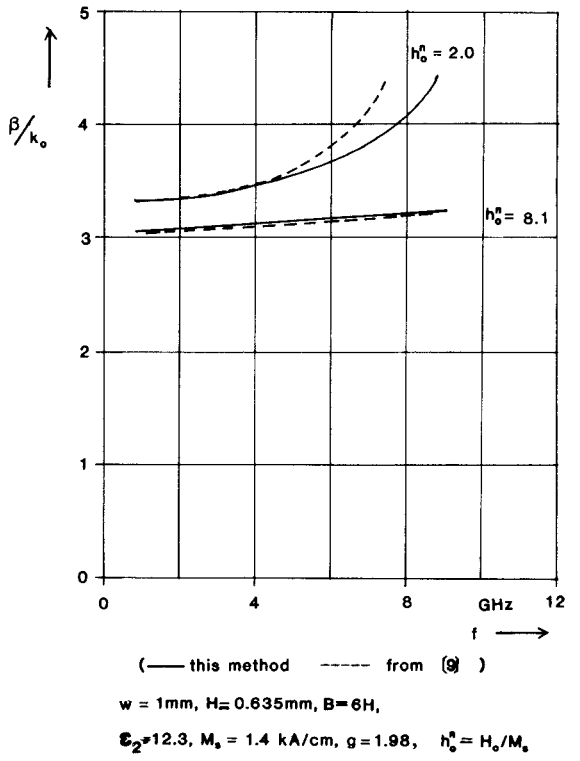

Fig. 31. Dispersion diagram for a microstrip on magnetized ferrite.

IV. Conclusions

A collection of new results has been presented in this paper aiming at the clarification of anisotropic substrate effects on the propagation properties of various integrated-circuit structures. In addition, the bulk of this paper has been devoted to the presentation of analytical and numerical methods which are useful in the accurate modeling of the effective dielectric constant and characteristic impedance of various structures such as microstrip, slotline, and coplanar waveguide on anisotropic substrates.

The various quasi-static and dynamic analytical methods summarized in this paper have shown that when anisotropy is not accounted for in the computation of the waveguiding structure properties, an error is incurred which increases with decreasing linewidth and/or increasing frequency. The concept of anisotropy ratio (AR) has been introduced, which may be used as an indication of dimensional tolerance sensitivity for coupled lines with cover, where the cover is used for achieving equalization of even- and odd-mode phase velocities. It has been found that, when AR >1, the equalization of phase velocities is less sensitive to small variations in the cover height to substrate thickness ratio compared to when AR $\leqslant 1$. Also, it has been seen that by introducing an equivalent relative dielectric constant and an equivalent substrate thickness, the anisotropic layer may be replaced by an equivalent isotropic substrate for microstrip without cover. In this case, computations are simplified since existing design methods for microstrip without cover may be used provided ϵ_r and H are replaced by ϵ_{eq} and H_{eq}, respectively.

The quasi-static methods summarized in this paper prove to be of practical use when the largest (and transverse to the direction of propagation) characteristic dimension of the circuit structure under consideration is small by comparison to the source wavelength. Among the various techniques presented, the method of moments in conjunction with the pertinent Green's function provides a straightforward solution to the integral equation for the charge density of single or coupled lines. This solution may be obtained to within desired convergence accuracy even for open structures since the boundary condition at infinity is included in the Green's function representation. On the other hand, the finite differences technique suffers from convergence sensitivity problems, especially for open structures, while the variational method provides results only to within an upper or lower bound from the true answer. The method of moments is considered to be the superior of all the other quasi-static techniques discussed due to its versatility and excellent accuracy.

The dispersive properties of various integrated-circuit structures have also been addressed in this paper. It has been found that the Fourier series method is the most generalized dispersion modeling procedure since it yields solutions to essentially all the structures of practical interest. It provides, in addition, results to within desired convergence accuracy.

Similarly, the equivalent network method also offers a generalized approach since it can deal with most of the integrated-circuit geometries of practical interest with excellent accuracy. The modified Wiener–Hopf procedure, on the other hand, is a mathematically elegant technique, but it has been applied only to microstrip with cover on an anisotropic substrate and it has not been adopted to tackle the question of coupled microstrip lines and that of more general integrated-circuit structures.

The aforementioned dispersive models suffer from a major disadvantage in that they fail to characterize the dispersive properties of circuit discontinuities and structure transitions. The transmission-line matrix and the method of lines procedures, on the other hand, are adoptable to modeling effectively the dispersive properties of a waveguiding circuit in a rectangular waveguide as well as certain circuit discontinuities. As stated previously, the TLM technique has been applied to the geometry of single and coupled microstrip on sapphire in a rectangular waveguide for wide microstrip lines. The graphs shown in Fig. 21 for $\epsilon_{\text{eff}}^{(e,o)}$ have been found to be in error by 1.5 and 3 percent, respectively, when compared to the corresponding cases computed by the Fourier series method when the latter is applied with a convergence accuracy of 0.5 percent. This error observation, coupled with the fact that the computations in [44] refer only to wide lines ($w/H \geqslant 1$), suggests that there is no sufficient evidence for the degree of accuracy provided by this method, especially for lines with $w/H < 1$ on anisotropic substrates. In summary, the inherent disadvantages of this method are: a) the need of *a priori* knowledge or a very good initial guess of the domi-

nant field distribution; b) the dependence of the method on the chosen mesh size and large number of iterations necessary to achieve desired convergence accuracy, factors which may lead to excessive computer run time and memory storage requirements; c) the method is effective for modeling dispersion in closed structures only; d) the method does not yield readily an equivalent circuit for the discontinuities of interest; e) there is no theoretical or experimental verification for the dispersive models derived by this method for the step and gap discontinuities presented in this paper. The method of lines is also an effective method to study the dispersive properties of distributed circuits in a rectangular waveguide with very good accuracy. Its major advantage is the simplicity of the resulting computer algorithm which allows efficient circuit parameter computation on a personal computer. The method has also been used to model discontinuities such as a periodic meander microstrip line and a periodically slotted microstrip. In addition, it has been used effectively to model a slotline short circuit. The versatility of this method in resolving the dispersive properties of step, gap, and other nonperiodic types of useful discontinuities has yet to be demonstrated.

Neither the TLM technique nor the method of lines are adequately general to provide solutions for the dispersion properties for the majority of the structures in Fig. 1. In fact, these techniques are ineffective as far as open structures are concerned and, in particular, in the modeling of discontinuities associated with open structures.

A novel approach was developed recently which resolves the dispersion properties of microstrip transmission lines, and it provides very accurate frequency-dependent equivalent circuits for microstrip discontinuities such as microstrip gap, open-circuited microstrip, etc., on isotropic substrates [15]–[99]. The method accounts for line and discontinuity radiation loss, conductor thickness, as well as all substrate effects, including the excitation of substrate surface waves. The model involves derivation of the standing-wave pattern for the current density along the circuit from which the line dispersion properties and discontinuity frequency-dependent equivalent circuits are derived [96]. The current density standing-wave pattern is obtained by solving Pocklington's integral equation by the method of moments. The radiation aspects of the problem, as well as the substrate effects, are taken into account by the Green's function which is obtained by solving the boundary-value problem of radiation by an infinitesimally short electric dipole printed on a substrate [96]. This approach can be extended to all the microstrip geometries of Fig. 1, where the Green's function must be derived for anisotropic substrates. A dual direction may be followed for the geometries which involve slotlines.

Acknowledgment

The author is indebted to his students J. Castaneda, D. Jackson, and A. Nakatani for their critical review and helpful comments. Thanks are also due to S. Spurrier, P. Parris, and M. Schoneberg for typing the manuscript and to K. Abolhassani and A. Nakatani for drawing the figures. This paper was written at Phraxos.

References

[1] K. C. Gupta, R. Garg, and I. J. Bahl, *Microstrip Lines and Slotlines*. Dedham, MA: Artech House, 1979.

[2] T. C. Edwards, *Foundations for Microstrip Circuit Design*. New York: Wiley, 1981.

[3] M. Olyphant, Jr., "Measuring anisotropy in microwave substrates," in *IEEE MTT-S 1979 Int. Microwave Symp. Dig.*, Apr. 30–May 2, 1979, pp. 91–94.

[4] R. P. Owens, J. E. Aitken, and T. C. Edwards, "Quasi-static characteristics of microstrip on an anisotropic sapphire substrate," *IEEE Trans. Microwave Theory Tech.*, vol. MTT-24, pp. 499–505, Aug. 1976.

[5] T. C. Edwards and R. P. Owens, "2–18-GHz dispersion measurements on 10–100-Ω microstrip lines on sapphire," *IEEE Trans. Microwave Theory Tech*, vol. MTT-24, pp. 506–513, Aug. 1976.

[6] C. M. Krowne, "Microstrip transmission lines on pyrolytic boron nitride," *Electron. Lett.*, vol. 12, no. 24, pp. 642–643, Nov. 25, 1976.

[7] C. M. Krowne, "Pyrolytic boron nitride as a microstrip substrate material," in *Electrical Electronics Insulation Conf. Proc.*, Sept. 1977, pp. 35–38.

[8] B. Lax and K. J. Button, *Microwave Ferrites and Ferrimagnetics*. New York: McGraw-Hill, 1962

[9] N. Krause, "Ein Verfahren zur Berechnung der Dispersion einer Mikrostreifenleitung auf gyrotropem Substrat," *Arch. Elek. Übertragung.*, vol. 31, pp. 205–211, 1977.

[10] R. Pregla and S. B. Worm, "The method of lines for the analysis of planar waveguides with magnetized ferrite substrate," in *IEEE MTT-S 1984 Int. Microwave Symp. Dig.*, May 28–June 1, 1984, pp. 348–350.

[11] A. Beyer and I. Wolff, "Power density distribution analysis of ferrite loaded finlines for the development of integrated nonreciprocal millimeter wave elements," in *IEEE MTT-S Int. Symp. Dig.*, May 28–June 1, 1984, pp. 342–344.

[12] R. E. Collin, *Field Theory of Guided Waves*. New York: McGraw-Hill, 1960.

[13] J. A. Kong, *Theory of Electromagnetic Waves*. New York: Wiley, 1975.

[14] H. C. Chen, *Theory of Electromagnetic Waves*. New York: McGraw-Hill, 1983.

[15] A. A. Th. M. van Trier, "Guided electromagnetic waves in anisotropic media," *Appl. Sci. Res.*, vol. B3, pp. 305–308, 1953.

[16] M. L. Kales, "Modes in waveguides that contain ferrites," *J. Appl. Phys.*, vol. 24, pp. 604–608, May 1953.

[17] R. F. Soohoo, *Theory and Application of Ferrites*. Englewood Cliffs, NJ: Prentice Hall, 1960.

[18] J. B. Davies, "An analysis of the *m*-port symmetrical *H*-plane waveguide junction with central ferrite post," *IRE Trans. Microwave Theory Tech.*, vol. MTT-10, pp. 596–604, Nov. 1962.

[19] J. B. Davies and P. Cohen, "Theoretical design of symmetrical junction stripline circulator," *IEEE Trans. Microwave Theory Tech.*, vol. MTT-11, pp. 506–512, Nov. 1963.

[20] H. Bosma, "On stripline *Y*-circulation at UHF," *IEEE Trans. Microwave Theory Tech.*, MTT-12, pp. 61–72, Jan. 1964.

[21] W. J. Ince and E. Stern, "Nonreciprocal remanence phase shifters in rectangular waveguide," *IEEE Trans. Microwave Theory Tech.*, vol. MTT-15, pp. 87–95, Feb. 1967.

[22] J. B. Castillo, Jr., and L. E. Davis, "Computer-aided three-port waveguide junction circulator," *IEEE Trans. Microwave Theory Tech.*, vol. MTT-18, pp. 25–34, Jan. 1970.

[23] J. Helszajn, *Principles of Microwave Ferrite Engineering*. New York: Wiley, 1970.

[24] J. Helszajn, *Nonreciprocal Microwave Junctions and Circulators*. New York: Wiley, 1975.

[25] R. F. Soohoo, *Microwave Magnetics*. New York: Harper and Row, 1985.

[26] K. J. Button, "Microwave ferrite devices: The first ten years," *IEEE Trans. Microwave Theory Tech.*, vol. MTT-32, pp. 1088–1096, Sept. 1984.

[27] N. G. Alexopoulos, S. R. Kerner, and C. M. Krowne, "Dispersionless coupled microstrip over fused silica-like anisotropic substrates," *Electron. Lett.*, vol. 12, no. 22, pp. 579–580, Oct. 28, 1976.
[28] N. G. Alexopoulos and C. M. Krowne, "Characteristics of single and coupled microstrips on anisotropic substrates," *IEEE Trans. Microwave Theory Tech.*, vol. MTT-26, pp. 387–393, June 1978.
[29] A. G. D'Assunção, A. J. Giarola, and D. A. Rogers, "Characteristics of broadside coupled microstrip lines with iso/anisotropic substrates," *Electron. Lett.*, vol. 17, no. 7, pp. 264–265, Apr. 2, 1981.
[30] M. Kobayashi, "Analysis of the microstrip and the electrooptic light modulator," *IEEE Trans. Microwave Theory Tech.*, vol. MTT-26, pp. 119–126, Feb. 1978.
[31] ——, "Green's function technique for solving anisotropic electrostatic field problems," *IEEE Trans. Microwave Theory Tech.*, vol. MTT-26, pp. 510–512, July 1978.
[32] H. Shibata, S. Minakawa, and R Terakado, "Analysis of the shielded-strip transmission line with an anisotropic medium," *IEEE Trans. Microwave Theory Tech.*, vol. MTT-30, pp. 1264–1267, Aug. 1982.
[33] E. Yamashita, K. Atsuki, and T. Mori, "Application of MIC formulas to a class of integrated-optics modulator analyses: A simple transformation," *IEEE Trans. Microwave Theory Tech.*, vol. MTT-25, pp. 146–150, Feb. 1977.
[34] N. G. Alexopoulos and N. K. Uzunoglu, "An efficient computation of thick microstrip properties on anisotropic substrates," *J. Franklin Inst.*, vol. 306, no. 1, pp. 9–22, July 1978.
[35] N. G. Alexopoulos and N. K. Uzunoglu, "A simple analysis of thick microstrip anisotropic substrates," *IEEE Trans. Microwave Theory Tech.*, vol. MTT-26, pp. 455–456, June 1978.
[36] M. Horno, "Quasistatic characteristics of microstrip on arbitrary anisotropic substrates," *Proc. IEEE*, vol. 67, pp. 1033–1034, Aug. 1980.
[37] M. Horno, "Upper and lower bounds on capacitances of coupled microstrip lines with anisotropic substrates," *Proc. Inst. Elec. Eng.*, vol. 129, pt. H, no. 3, pp. 89–93, June 1982.
[38] M. Horno and R. Marqués, "Coupled microstrips on double anisotropic layers," *IEEE Trans. Microwave Theory Tech.*, vol. MTT-32, pp. 467–470, Apr. 1984.
[39] S. K. Koul and B. Bhat, "Inverted microstrip and suspended microstrip with anisotropic substrates," *Proc. IEEE*, vol. 70, pp. 1230–1231, Oct. 1982.
[40] S. K. Koul and B. Bhat, "Shielded edge-coupled microstrip mixture with anisotropic substrates," *Arch. Elek. Übertragung*, vol. 37, pp. 269–274, July/Aug. 1983.
[41] S. K. Koul and B. Bhat, "Transverse transmission line method for the analysis of broadside-coupled microstrip lines with anisotropic substrates," *Arch. Elek. Übertragung.*, vol. 37, pp. 59–64, Jan./Feb. 1983.
[42] S. K. Koul and B. Bhat, "Generalized analysis of microstrip-like transmission lines and coplanar strips with anisotropic substrates for MIC, electrooptic modulator, and SAW applications," *IEEE Trans. Microwave Theory Tech.*, vol. MTT-31, pp. 1051–1058, Dec. 1983.
[43] T. Kitazawa and Y. Hayashi, "Quasi-static characteristics of coplanar waveguide on a sapphire substrate with its optical axis inclined," *IEEE Trans. Microwave Theory Tech.*, vol. MTT-30, pp. 920–922, June 1982.
[44] G. E. Mariki, "Analysis of microstrip lines on inhomogeneous anisotropic substrates," Ph.D. dissertation, Univ. of California, Los Angeles, June 1978.
[45] G. E. Mariki and C Yeh, "Dynamic three-dimensional TLM analysis of microstrip lines on anisotropic substrates," *IEEE Trans. Microwave Theory Tech.*, vol. MTT-33, pp. 789–799, Sept. 1985.
[46] P. B. Johns and R. L. Beurle, "Numerical solution of two dimensional scattering problems using a transmission line matrix," *Proc. Inst. Elec. Eng.*, vol. 118, pp. 1203–1208, Sept. 1971
[47] P. B. Johns, "Application of the transmission line matrix method to homogeneous waveguides of arbitrary cross section," *Proc. Inst. Elec. Eng.*, vol. 119, pp. 1086–1091, Aug. 1972.
[48] S. Akhtarzad and P. B. Johns, "The solution of Maxwell's equations in three space dimensions and time by the TLM method," *Proc. Inst. Elec. Eng.*, vol. 122, 1975.
[49] S. Akhtarzad and P. B. Johns, "Generalised elements for the TLM method of numerical analysis," *Proc. Inst. Elec. Eng.*, vol. 122, 1975.
[50] W. Getsinger, "Microstrip dispersion model," *IEEE Trans. Microwave Theory Tech.*, vol. MTT-21, pp. 34–39, Jan. 1973.
[51] A-M. A. El-Sherbiny, "Hybrid mode analysis of microstrip lines on anisotropic substrates," *IEEE Trans. Microwave Theory Tech.*, vol. MTT-29, pp. 1261–1265, Dec. 1981.
[52] Y. Hayashi and T. Kitazawa, "Analysis of microstrip transmission line on a sapphire substrate," *J. Inst. Electron. Commun. Eng. Jap.*, vol. 62-B, pp. 596–602, June 1979.
[53] T. Kitazawa and Y. Hayashi, "Coupled slots on an anisotropic sapphire substrate," *IEEE Trans. Microwave Theory Tech.*, vol. MTT-29, pp. 1035–1040, Oct. 1981.
[54] T. Kitazawa and Y. Hayashi, "Propagation characteristics of striplines with multilayered anisotropic media," *IEEE Trans. Microwave Theory Tech.*, vol. MTT-31, pp. 429–433, June 1983.
[55] K. Shibata and K. Hatori, "Dispersion characteristics of coupled microstrip with overlay on anisotropic dielectric substrate," *Electron. Lett.*, Jan. 1984.
[56] A. Nakatani and N. G. Alexopoulos, "A generalized algorithm for structures on anisotropic substrates," presented at IEEE MTT-S Int. Microwave Symp., St. Louis, June 1985.
[57] N. J. Damaskos, R. B. Mack, A. L. Maffett, W. Parmon, and P. L. E. Uslenghi, "The inverse problem for biaxial materials," *IEEE Trans. Microwave Theory Tech.*, vol. MTT-32, pp. 400–405, Apr. 1984.
[58] J. Fontanella, C. Andeen, and D. Schuele, "Low-frequency dielectric constants of α-quartz, sapphire, MgFz and MgO," *J. Appl. Phys.*, vol. 45, no. 7, pp. 2852–2854, July 1974.
[59] W. B. Westphal and A. Sils, "Dielectric constant and ion data," Tech. Rep. AFML-TR-72-39, Apr. 1972.
[60] P. H. Ladbrooke, M. H. N. Potok, and E. H. England, "Coupling errors in cavity-resonance measurements on MIC dielectrics," *IEEE Trans Microwave Theory Tech.*, vol. MTT-21, pp. 560–562, Aug. 1973.
[61] E. V. Loewenstein, D. R. Smith, and R. L. Morgan, "Optical constants for infra-red materials, 2: Crystalline solids," *Appl. Optics*, vol. 12, pp. 398–406, Feb. 1973.
[62] E. E. Russell and E. E. Bell, "Optical constants of sapphire in the far infrared," *J. Opt. Soc. Am.*, vol. 57, pp. 543–544, Apr. 1967.
[63] S. Roberts and D. D. Coon, "Far-infrared properties of quartz and sapphire," *J. Opt. Soc. Am.*, vol. 52, pp. 1023–1029, Sept. 1962.
[64] M. Olyphant, Jr., "Microwave permittivity measurements using disk cavity specimens," *IEEE Trans. Instrum. Meas.*, vol. 20, no. 4, pp. 342–344, Nov 1971.
[65] RT/Duroid®, Rogers Corporation, TR 2692, July 1981.
[66] W. R. Smythe, *Static on Dynamic Electricity*. New York: McGraw-Hill, 1950.
[67] L. D Landau and E. M. Lifshitz, *Electrodynamics of Continuous Media*. Addison-Wesley, 1960.
[68] B. T. Szentkuti, "Simple analysis of anisotropic microstrip lines by a transform methods," *Electron. Lett.*, vol. 25, no. 12, pp. 672–673, Dec. 9, 1976.
[69] M. Kobayashi and R. Terakado,"New view on an anisotropic medium and its application to transformation from anisotropic to isotropic problems," *IEEE Trans. Microwave Theory Tech.*, vol. MTT-27, pp. 769–775, Sept. 1979.
[70] ——, "Accurately approximate formula of effective filling fraction for microstrip line with isotropic substrate and its application to the case with anisotropic substrate," *IEEE Trans. Microwave Theory Tech.*, vol. MTT-27, pp. 776–778, Sept. 1979.
[71] ——, "Method for equalizing phase velocities of coupled microstrip lines by using anisotropic substrate," *IEEE Trans. Microwave Theory Tech.*, vol. MTT-28, pp. 719–722, July 1980.
[72] E. Yamashita, K. Atsuki, and T. Akamatsu, "Application of microstrip analysis to the design of a broad-band electrooptical modulator," *IEEE Trans. Microwave Theory Tech.*, vol. 22, pp. 462–464, Apr. 1974.
[73] E. Yamashita and K. Atsuki, "Distributed capacitance of a thin-film electrooptic light modulator," *IEEE Trans. Microwave Theory Tech.*, vol. 23, pp. 177–178, Jan. 1975.
[74] T. G. Bryant and J. A. Weiss, "Parameters of microstrip transmission lines and of coupled pairs of microstrip lines," *IEEE Trans. Microwave Theory Tech.*, vol. MTT-16, pp. 1021–1027, Dec. 1968.
[75] A. Farrar and A. T. Admas, "Characteristic impedance of microstrip by the method of moments," *IEEE Trans. Microwave Theory Tech.*, vol. 18, pp. 65–66, Jan. 1980.
[76] R. F. Harrington, *Field Computation by Moment Methods*. New York: Macmillan Co , 1968.
[77] N. G. Alexopoulos and S. A. Maas, "Characteristics of microstrip directional couplers on anisotropic substrates," *IEEE Trans. Microwave Theory Tech.*, vol. MTT-30, pp. 1267–1270, Aug. 1982.

[78] N. G. Alexopoulos and S. A. Maas, "Performance of microstrip couplers on an anisotropic substrate with an isotropic superstate," *IEEE Trans. Microwave Theory Tech.*, vol. MTT-31, pp. 671–673, Aug. 1983.
[79] B. Sheleg and B. E. Spielman, "Broad-band directional couplers with dielectric overlays," *IEEE Trans. Microwave Theory Tech.*, vol. MTT-22, pp. 1216–1220, Dec. 1974.
[80] D. Paolino, "MIC overlay coupler design using spectral domain techniques," *IEEE Trans. Microwave Theory Tech.*, vol. MTT-26, pp. 646–649, Sept. 1978.
[81] G. Haupt and H. Delfs, "High directivity microstrip couplers," *Electron. Lett.*, vol. 10, no. 9, pp. 142–143, May 2, 1974.
[82] R. N. Karekar and M. K. Pande, "MIC coupler with improved directivity using thin film BiO_3 overlay," *IEEE Trans. Microwave Theory Tech.*, vol. MTT-25, pp. 74–75, Jan. 1977.
[83] S. Rhenmark, "High directivity CTL couplers and a new technique for measurement of CTL coupler parameters," *IEEE Trans. Microwave Theory Tech.*, vol. MTT-25, p. 1116, Dec. 1977.
[84] J. E. Dalley, "A stripline directional coupler utilizing a non-homogeneous dielectric medium," *IEEE Trans. Microwave Theory Tech.*, vol. MTT-17, pp. 706–712, Sept. 1969.
[85] K. Atsuki and E. Yamashita, "Three methods for equalizing the even- and odd-mode phase velocity of coupled strip lines with an inhomogeneous medium," *Trans. IECE (Japan)*, vol. 55-B, pp. 424–426, July 1972 (in Japanese).
[86] W. T. Weeks, "Calculation of coefficients of capacitance of multiconductor transmission lines in the presence of a dielectric interface," *IEEE Trans. Microwave Theory Tech.*, vol. MTT-19, pp. 35–43, Jan. 1970.
[87] E. Yamashita, K. Atsuki, and T. Akamatsu, "Application of microstrip analysis to the design of a broad-band electrooptical modulator," *IEEE Trans. Microwave Theory Tech.*, vol. MTT-22, pp. 462–464, Apr. 1974.
[88] E. Yamashita and K. Atsuki, "Distributed capacitance of a thin-film electrooptic light modulator," *IEEE Trans. Microwave Theory Tech.*, vol. MTT-23, pp. 177–178, Jan. 1975.
[89] T. Kitazawa and Y. Hayashi, "Quasi-static characteristics of coplanar waveguide on a sapphire substrate with its optical axis inclined," *IEEE Trans. Microwave Theory Tech.*, vol. MTT-30, pp. 920–922, June 1982.
[90] M. Kobayashi, "Frequency dependent characteristics of microstrips on anisotropic substrates," *IEEE Trans. Microwave Theory Tech.*, vol. MTT-30, pp. 2054–2057, Nov. 1982.
[91] M. V. Schneider, "Microstrip lines for microwave integrated circuits," *Bell Syst. Tech. J.*, vol. 48, pp. 1421–1444, May/June 1969.
[92] E. Yamashita, K. Atsuki, and T. Ueda, "An approximate dispersion formula of microstrip lines for computer-aided design of microwave integrated circuits," *IEEE Trans. Microwave Theory Tech.*, vol. MTT-27, pp. 1036–1038, Dec. 1979.
[93] U. Schulz and R. Pregla, "A new technique for the analysis of the dispersion characteristics of planar waveguides," *Arch. Elek. Übertragung.*, vol. 34, pp. 169–173, 1980.
[94] U. Schulz and R. Pregla, "A new technique for the analysis of the dispersion characteristics of planar waveguides and its application to microstrips with tuning septums," *Radio Sci.*, vol. 16, pp. 1173–1178, Nov.–Dec. 1981.
[95] S. B. Worm and R. Pregla, "Hybrid mode analysis of arbitrarily shaped planar microwave structures by the method of lines," *IEEE Trans. Microwave Theory Tech.*, vol. MTT-32, pp. 191–196, Feb. 1984.
[96] P. B. Katehi and N. G. Alexopoulos, "On the modeling of electromagnetically coupled microstrip antennas—The printed strip dipole," *IEEE Trans. Antennas Propagat.*, vol. 32, pp. 1179–1186, Nov. 1984.
[97] P. B. Katehi and N. G. Alexopoulos, "Microstrip discontinuity modelling for millimetric integrated circuits," in *1985 IEEE MTT-S Int. Microwave Symp. Proc.*, pp. 571–573.
[98] R. W. Jackson and D. M. Pozar, "Surface wave losses at discontinuities in millimeter wave integrated transmission lines," in *1985 IEEE MTT-S Int. Microwave Symp. Proc.*, pp. 563–565.
[99] P. B. Katehi and N. G. Alexopoulos, "Frequency dependent characteristics of microstrip discontinuities in millimeter wave integrated circuits," *IEEE Trans. Microwave Theory Tech.*, this issue, pp. 1029–1035.

✠

Nicólaos G. Alexópoulos (S'68–M'69–SM'82) was born in Athens, Greece, in 1942. He graduated from the 8th Gymnasium of Athens, Greece, and subsequently obtained the B.S.E.E., M.S.E.E., and Ph.D. degrees from the University of Michigan, Ann Arbor, MI, in 1964, 1967, and 1968, respectively.

He is currently a Professor in the Department of Electrical Engineering, University of California, Los Angeles, and a Consultant with Northrop Corporation's Advanced Systems Division. His current research interests are in electromagnetic theory as it applies in the modeling of integrated-circuit components and printed circuit antennas for microwave and millimeter-wave applications, substrate materials and their effect on integrated-circuit structures and printed antennas, integrated-circuit antenna arrays, and antenna concealment studies. He is the Associate Editor of the IEEE TRANSACTIONS ON ANTENNAS AND PROPAGATION, *Electromagnetics Journal*, and *Alta Frequenza*.